

Master thesis

Master in Chemical Engineering Technology

Chemical Engineering Technology

Hexane to hexanol oxidation with metal-organic frameworks in the light of direct alkane to alcohol conversion

Quinten Diddens

Supervisor: Prof. Dr. Pedro Luis Arias
Co-supervisor: Dr. Iker Agirrezabal-Telleria

Academic year 2023-2024

Preface

I would like to extend my deepest gratitude to several individuals and groups who have been instrumental in the successful completion of my master's thesis.

First and foremost, I would like to thank my thesis supervisor and co-supervisor, Prof. Dr. Pedro Luis Arias and Dr. Iker Agirrezabal-Telleria, for their unwavering support, invaluable guidance, and insightful feedback throughout this journey. Their expertise and encouragement have been crucial in shaping this work.

I am also profoundly grateful to my professors and academic mentors, both at my home university (KU Leuven) as well as at my guest university (Universidad del País Vasco), whose teaching and advice have significantly contributed to my educational and personal growth. Their dedication and passion for their subjects have inspired me throughout my studies.

To my family, your endless support and belief in me have been the foundation of my perseverance. Your love and sacrifices have made this achievement possible, and for that, I am forever thankful.

I extend my heartfelt thanks to my friends and peers for their constant encouragement, camaraderie, and for making this academic journey more enjoyable and less arduous.

I would also like to acknowledge my research collaborators and lab members, Dr. Adrián Angulo Ibáñez and many others of the SuPrEn research group from my guest university, whose assistance and cooperation were indispensable during the research process. Special thanks go to the technical and administrative staff, whose behind-the-scenes efforts ensured a smooth and efficient research environment.

Finally, I am grateful to the funding agencies and scholarship providers, Erasmus+, KU Leuven and Universidad del País Vasco, whose financial support has enabled me to pursue and complete this research.

To everyone who has contributed to this journey in any way, your support and encouragement have been invaluable, and I am deeply appreciative of your contributions.

Abstract

This thesis investigates the oxidation of hexane to hexanol using metal-organic frameworks (MOFs) as catalysts, with hydrogen peroxide as the oxidizing agent. The study focuses on MIL-100, HKUST-1, and MOF-808 @His-Cu, examining their structural, thermal, and catalytic properties. Nitrogen adsorption-desorption isotherms and XRD analyses reveal distinct pore structures and crystallinity levels, which significantly influence their performance. MIL-100 and HKUST-1 exhibit mesoporous characteristics, while MOF-808 @His-Cu shows slit-shaped mesopores. XRD results indicate that MIL-100 is synthesized with high purity and relatively high crystallinity, HKUST-1 has a minor impurity, and MOF-808 @His-Cu shows signs of impurities or incomplete synthesis.

The SEM images reveal distinct morphologies: MIL-100 displays porous polyhedral grains, HKUST-1 exhibits smooth octahedral crystals, and MOF-808 @His-Cu shows precise octahedral crystals, confirming their crystalline nature. Thermogravimetric analysis (TGA) demonstrates that MIL-100 has the highest thermal stability, followed by HKUST-1 and MOF-808 @His-Cu. Under inert conditions, MIL-100 decomposes at higher temperatures than the other MOFs, reflecting its greater stability.

Experimental results indicate that increasing temperature and reaction time enhance hexane conversion, though selectivity decreases with temperature but improves with longer reaction times. Varying pressure does not significantly affect conversion or selectivity, and the presence of MOFs significantly boosts both conversion and selectivity compared to reactions without MOFs.

Among the studied MOFs, MIL-100 offers lower conversion but higher selectivity compared to HKUST-1, while MOF-808 @His-Cu exhibits both lower conversion and selectivity. These findings underscore the importance of MOF properties in optimizing hexane oxidation processes and provide valuable insights for their application in industrial catalysis.

Keywords: Metal-organic frameworks (MOFs), MOF characterisation, hexane to hexanol oxidation, batch reactor, catalytic performance

TABLE OF CONTENTS

Preface	i
Abstract	ii
List of Figures	v
List of Tables	vi
List of Symbols	vii
1 Introduction	1
1.1 Overview	1
1.1.1 DEMO project idea	1
1.1.2 Currently investigated methodologies.....	1
1.2 Methane	2
1.2.1 Human health	2
1.2.2 Greenhouse gas	2
1.2.3 Sources	3
1.2.4 Current and outlook.....	3
1.3 Methanol	3
1.3.1 Applications	4
1.3.2 Hydrogen production	4
1.3.3 Methanol fuel cells.....	4
1.3.4 Other applications	5
1.4 Methane-to-methanol.....	5
1.4.1 Direct Oxidative Methane Conversion.....	6
1.4.2 Thermochemical Methane Conversion	7
1.4.3 Plasma-Assisted Methane Conversion.....	8
1.4.4 Biological Methane Conversion.....	8
1.4.5 Hybrid and Integrated Processes	9
1.5 Intended methodology	9
1.5.1 Parallel researched technique.....	9
1.5.2 Process under development.....	10
1.6 Research methodology.....	14
1.6.1 Components.....	14
1.6.2 P&ID	18
2 Materials and methods	19
2.1 Materials	19
2.2 Experimental setup	19
2.3 MOF synthesis	19
2.3.1 MIL-100.....	19
2.3.2 HKUST-1	20
2.3.3 MOF-808 @His-Cu.....	20
2.4 MOF characterisation techniques	21
2.4.1 Nitrogen adsorption analysis.....	21
2.4.2 X-ray diffraction (XRD)	24
2.4.3 Field emission scanning electron microscopy (FE-SEM).....	25

2.4.4	Thermogravimetric analysis (TGA)	27
2.5	Sample analysis and calibration measurements	28
2.5.1	Gas chromatography	28
2.5.2	Used chromatographs	30
2.6	Conversion and selectivity	32
2.6.1	Calculations	32
3	Results and Discussion	34
3.1	Characterisation	34
3.1.1	Nitrogen adsorption analysis	34
3.1.2	XRD	38
3.1.3	FE-SEM	41
3.1.4	TGA	43
3.2	Parameters	48
3.2.1	Presence of MOFs	48
3.2.2	MOF type	49
3.2.3	Relative MOF mass	49
3.2.4	Temperature	50
3.2.5	Pressure	51
3.2.6	<i>n</i> -Hexane:H ₂ O ₂ ratio	52
3.2.7	Reaction time	53
4	Conclusion	55
	Bibliography	56

List of Figures

Figure 1: DEMO project idea.....	1
Figure 2: Thesis idea.....	2
Figure 3: Oxidation active Fe site.....	9
Figure 4: Oxidation active site MIL-100.....	9
Figure 5: Operation conditions or the different stages in the parallel researched technique.....	10
Figure 6: P&ID research methodology.....	18
Figure 7: Experimental setup.....	19
Figure 8: MIL-100.....	20
Figure 9: HKUST-1.....	20
Figure 10: MOF-808 @His-Cu.....	20
Figure 11: IUPAC classification of adsorption isotherms.....	22
Figure 12: IUPAC Classification of Hysteresis Loops.....	22
Figure 13: Bragg's law for X-ray diffraction.....	25
Figure 14: Scanning electron microscope.....	26
Figure 15: Interaction of specimen with electron beam.....	26
Figure 16: Bottom loading or hang-down.....	28
Figure 17: Top loading.....	28
Figure 18: Side loading.....	28
Figure 19: GC.....	29
Figure 20: GC-MS.....	29
Figure 21: Nitrogen adsorption-desorption isotherm MIL-100.....	34
Figure 22: Nitrogen adsorption-desorption isotherm HKUST-1.....	35
Figure 23: Nitrogen adsorption-desorption isotherm MOF-808 @His-Cu.....	35
Figure 24: Surface areas per MOF.....	36
Figure 25: Pore volume per MOF.....	38
Figure 26: Pore size distribution per MOF.....	38
Figure 27: XRD MIL-100 used (top) and simulated (bottom).....	39
Figure 28: XRD HKUST-1 used (top) and simulated (bottom).....	40
Figure 29: XRD MOF-808 @His-Cu used (top) and simulated (bottom).....	40
Figure 30: SEM image MIL-100 (2 μm).....	42
Figure 31: SEM image MIL-100 (20 μm).....	42
Figure 32: SEM image HKUST-1 (2 μm).....	42
Figure 33: SEM image HKUST-1 (20 μm).....	42
Figure 34: SEM image MOF-808 @His-Cu (2 μm).....	42
Figure 35: SEM image MOF-808 @His-Cu (20 μm).....	42
Figure 36: TGA of MIL-100 at constant N_2 gas flow with 5,0 K/min ramp.....	43
Figure 37: TGA of HKUST-1 at constant N_2 gas flow with 5,0 K/min ramp.....	44
Figure 38: TGA of MOF-808 @His-Cu at constant N_2 gas flow with 5,0 K/min ramp.....	44
Figure 39: TGA of MIL-100 at constant O_2 gas flow with 5,0 K/min ramp.....	45
Figure 40: TGA of HKUST-1 at constant O_2 gas flow with 5,0 K/min ramp.....	46
Figure 41: TGA of MOF-808 @His-Cu at constant O_2 gas flow with 5,0 K/min ramp.....	46
Figure 42: TGA all MOFs under isothermal (200°C) and N_2 gas flow conditions.....	47
Figure 43: Effect of MOFs on conversion.....	49
Figure 44: Effect of MOFs on selectivity.....	49
Figure 45: Effect of temperature for reaction conditions a.....	51
Figure 46: Effect of temperature for reaction conditions b.....	51
Figure 47: Effect of n -hexane: H_2O_2 ratio for reaction conditions a.....	53
Figure 48: Effect of n -hexane: H_2O_2 ratio for reaction conditions b.....	53
Figure 49: Effect of reaction time for reaction conditions a.....	54
Figure 50: Effect of reaction time for reaction conditions b.....	54

List of Tables

Table 1: Surface areas	36
Table 2: Pore volumes and size distribution.....	37
Table 3: Effect of MOFs	48
Table 4: Effect MOF type	49
Table 5: Effect of relative MOF mass	50
Table 6: Effect of temperature.....	51
Table 7: Effect of pressure	52
Table 8: Effect of <i>n</i> -hexane:H ₂ O ₂ ratio	53
Table 9: Effect of reaction time.....	54

List of Symbols

d	Inner spacing	[m]
m	Mass of adsorbent	[g]
n	Diffraction order	[/]
r	Pore radius	[m]
t	Thickness of the adsorbed layer	[m]
$v\%$	Volume percentage	[/]
C	BET constant	[/]
N_A	Avogadro's number	[molecules/mol]
P_0	Saturation pressure of nitrogen	[Pa]
P	Equilibrium pressure of nitrogen	[Pa]
R	Gas constant	[J/K.mol]
S_{BET}	Surface area per gram of adsorbent	[m ² /g]
T	Temperature	[K]
V_{ads}	Amount of nitrogen adsorbed	[m ³]
V_m	Volume of nitrogen adsorbed at monolayer coverage	[m ³]
V_M	Molar volume of liquid nitrogen	[m ³]
V	Volume of nitrogen adsorbed at pressure P	[m ³]
γ	Surface tension of liquid nitrogen	[N/m]
θ	Angles of diffraction	[rad]
λ	Wavelength	[m]
σ	Cross-sectional area of a nitrogen molecule	[m ²]

List of Abbreviations

MOF	Metal-Organic Framework
MMO	Methane MonoOxygenase
PFR	Plug Flow Reactor
PM _{2.5}	Particulate matter with a diameter of 2,5 micrometre or smaller
GWP	Global Warming Potential
SRES	Special Report on Emissions Scenarios
RCP	Representative Concentration Pathways
AI	Artificial Intelligence
DME	DiMethyl Ether
CAGR	Compound Annual Growth Rate
PEM	Proton Exchange Membrane
PEMFC	Proton Exchange Membrane Fuel Cell
DMFC	Direct Methanol Fuel Cell
MTO	Methanol-To-Olefins
MTG	Methanol-To-Gasoline
MTM	Methane-To-Methanol
SMA	SilicoMolybdc Acid
CFD	Computational Fluid Dynamics
ZSM	Zeolite Socony Mobil
WGS	Water-Gas Shift
DBD	Dielectric Barrier Discharge
IPC	In-Plasma Catalysis
PPC	Post-Plasma Catalysis
BTC	Benzene-1,3,5-TriCarboxylate
sMMO	soluble Methane MonoOxygenase
pMMO	particulate Methane MonoOxygenase
GC	Gas Chromatograph
Milli-Q® water	Ultrapure water (Type 1)
H ₂ BTC	Trimesic acid
ACN	ACetoNitrile
BET	Brunauer-Emmett-Teller
STP	Standard Temperature and Pressure
XRD	X-Ray Diffraction
TGA	ThermoGravimetric Analysis
EGA	Evolved Gas Analysis
ICTAC	International Confederation for Thermal Analysis and Calorimetry
TA	Thermal Analysis
FE-SEM	Field Emission Scanning Electron Microscopy
SEM	Scanning Electron Microscopy
FEG	Field Emission Gun
TEM	Transmission Electron Microscopy
SEs	Secondary Electrons
BSEs	BackScattered Electrons
CL	CathodoLuminescence
GC-MS	Gas Chromatograph-Mass Spectrometer
FID	Flame Ionization Detector
TCD	Thermal Conductivity Detector
MS	Mass Spectroscopy
C6 molecules	Organic molecules that contain 6 Carbon atoms (analogue for C2 and C3)

1 Introduction

1.1 Overview

1.1.1 DEMO project idea

The 'DEMO project' partnership employs a novel approach, utilizing metal-organic frameworks (MOFs) and enzymes to convert methane to methanol. MOFs impregnated with methane monooxygenase (MMO) enzymes or biomimicking these enzymes facilitate this conversion within their pores, under continuous gas flow conditions resembling a plug flow reactor (PFR) concept. With N_2O as the oxidizing agent and operating at relatively low pressure and temperature, this technique promises greater economic efficiency and reduced equipment requirements compared to traditional methods. The chemical reaction targeted by the DEMO project research team is given in **Figure 1** [1]. Further detail will be given in **1.5.2**.

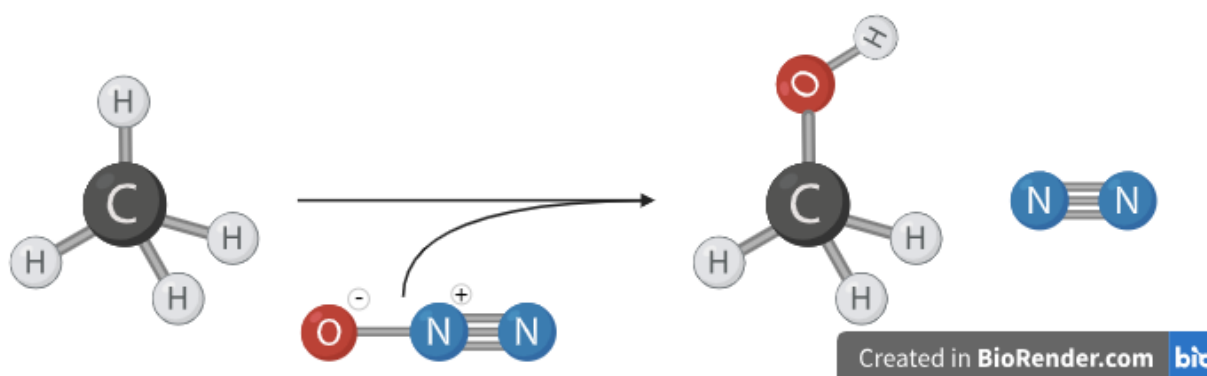


Figure 1: DEMO project idea

In addition to investigating the specific objectives outlined within the DEMO project, it is essential to contextualize this research within the broader scope of a comprehensive exploration into hydrocarbon conversion processes. The DEMO project represents a pivotal component of a larger research initiative aimed at elucidating the mechanisms involved in the transformation of hydrocarbons into alcohols and olefins. While the oxidation of methane to methanol stands as one of the most challenging endeavours within this field, the investigation into hexane oxidation holds significant relevance. Not only does this pathway offer the potential to produce higher-order alcohols compared to methanol, but it also serves as a valuable avenue for gaining fundamental insights into the intricate mechanisms underlying hydrocarbon oxidation processes, particularly when employing metal-organic frameworks (MOFs) as heterogeneous catalysts. Thus, the exploration of hexane oxidation in this master thesis as part of the DEMO project not only addresses immediate research objectives but also contributes to advancing the broader understanding of hydrocarbon oxidation mechanisms, paving the way for innovative catalytic solutions in sustainable chemical synthesis.

1.1.2 Currently investigated methodologies

1.1.2.1 Research methodology of this master thesis

In this master thesis, the conversion of hexane to hexanol utilizing hydrogen peroxide (H_2O_2) as the oxidizing agent within a continuously stirred batch reactor will be investigated. The research will employ metal-organic frameworks (MOFs) as catalysts to facilitate the reaction. MOFs are porous materials with a highly ordered structure, typically constructed from metal ions or clusters connected by organic linkers. Parameters such as temperature, pressure, MOF type, reaction time, and the ratio of oxidant to hexane will systematically be varied to assess their respective impacts on conversion efficiency and selectivity in the hexane to hexanol transformation. This rigorous examination aims to elucidate the optimal conditions for maximizing hexanol yield while minimizing the formation of undesired byproducts, providing valuable insights into the fundamental principles underlying this

catalytic process. The targeted chemical reaction for this thesis can be found in **Figure 2** [2].

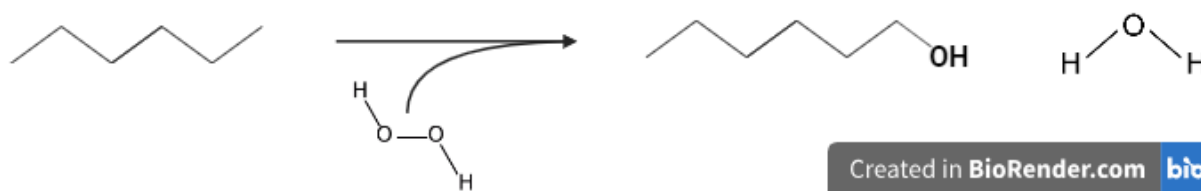


Figure 2: Thesis idea

1.1.2.2 Parallel researched technique

The parallel researched technique aims to convert propane to propanol in a continuous flow reactor, representing a direct oxidation approach in hydrocarbon transformation. This method harnesses the catalytic properties of metal-organic frameworks (MOFs) to facilitate the conversion process, utilizing N₂O gas as the oxidizing agent. Additionally, the continuous flow reactor provides precise control over reaction parameters such as temperature, pressure, and residence time, enabling optimization of reaction conditions for maximum efficiency and product yield. This direct oxidation technique holds promise for sustainable chemical synthesis, offering a viable pathway for the conversion of propane to propanol with reduced environmental impact and improved process economics.

1.2 Methane

1.2.1 Human health

Research shows that industrial air pollution such as methane pollution leads to excess mortalities, revealing significant associations with cardiopulmonary disease and lung cancer. When identifying the drivers of these changes, results indicate that increases in emissions of short-lived air pollutants predominantly contribute to the escalation in PM_{2.5} and health related O₃ concentrations, accounting for the majority of their total increases. Notably, the rise in methane (CH₄) concentrations emerges as the second most influential factor driving increases in health-related O₃ levels, underscoring its significance in exacerbating respiratory mortalities associated with industrial O₃ exposure [3].

Additionally, the findings shed light on the disproportionate impact of CH₄ on respiratory mortalities across various regions, highlighting the pressing need for CH₄ mitigation strategies to mitigate the health risks posed by industrial O₃ pollution [4]. By identifying cost-effective CH₄ mitigation options internationally, particularly in regions where mortality burdens are more sensitive to CH₄ concentrations, significant reductions in premature mortalities associated with O₃ exposure can be achieved [5]. These findings underscore the crucial role of controlling CH₄ emissions in air quality policy and advocate for the implementation of available CH₄ mitigation measures to alleviate the health burdens associated with industrial O₃ pollution [3].

The proportionate impact of elevated CH₄ on O₃-related mortality is expected to persistently escalate, thereby amplifying the relative health advantages of CH₄ mitigation.

1.2.2 Greenhouse gas

The intricate role of methane in atmospheric chemistry remains a subject of ongoing exploration, with many facets yet to be fully elucidated. Methane undergoes a complex series of photochemical reactions, resulting in its oxidation to carbon monoxide (CO), carbon dioxide (CO₂), water (H₂O), and CH₂O. This oxidation process serves as the predominant sink for methane in the atmosphere, primarily mediated by the hydroxyl radical (OH) [6], [7]. Notably, this reaction involves a spectrum of trace gases, including ozone (O₃) [8].

The impact of atmospheric methane extends beyond its direct chemical transformations. It plays a multifaceted role in Earth's radiative balance, contributing to the formation of other greenhouse gases like CO₂ and water vapor through its oxidation. Moreover, methane's absorption spectrum for infrared radiation directly influences global warming. Additionally, methane's presence influences the lifetimes of various other climatically significant gases, such as ozone (O₃) [8].

In summary, methane's involvement in atmospheric chemistry is intricate and far-reaching, with implications for both atmospheric composition and climate dynamics. Despite significant advances in understanding, there remains much to uncover about the complexities of methane's interactions within the Earth's atmosphere.

1.2.3 Sources

Based on the existing literature, methane emissions arise from six primary sources:

1. Anaerobic decomposition of vegetation in natural wetlands, as documented by [9], [10]
2. Emissions from livestock production systems, encompassing enteric fermentation in animals as noted by [11], [12], along with methane release from animal waste.
3. Natural gas losses during fossil fuel exploration, processing, and distribution, including coal mining, natural gas, and the petrochemical industry, as observed by [13].
4. Anaerobic decomposition in paddy rice fields, as evidenced [14], [15], [16].
5. Biomass burning activities, encompassing forest and savanna fires, burning of agricultural waste, charcoal production, and firewood combustion, as discussed by [17], [18].
6. Anaerobic decomposition of waste in landfills, as highlighted by [19].

These sources collectively contribute to methane emissions and underscore the importance of understanding and mitigating their impacts on the environment.

1.2.4 Current and outlook

In nearly all scenarios outlined in the SRES [20] and RCP [21] emissions projections, CH₄ is anticipated to rise, with exceptions noted in the SRES B2 and RCP2.6 scenarios. Methane ranks as the second most significant anthropogenic greenhouse gas in the atmosphere after carbon dioxide. It also has a global warming potential (GWP) of 25 over a 100-year timeframe meaning that 1 kg of methane has a GWP equal to 25 kg of CO₂ [22]. This makes it a focal point for climate mitigation strategies.

Recently, on the 14th of February 2024, Google announced that it will use its AI and infrastructure mapping in combination with satellite data from the MethaneSAT satellite to create a better understanding for how to mitigate methane emissions. This shows that the relevance of methane mitigation, especially today, is significant. It also indicates that it is commercially relevant to engage in methane mitigation since Google is a profit-seeking enterprise [23].

1.3 Methanol

Methanol occupies a crucial role in the chemical industry as a remarkably versatile building block for the production of a myriad of everyday items, including paints, carpets, plastics, and more. Its significance extends further as it is increasingly utilized worldwide in innovative applications to address the escalating energy demand. Methanol serves as a fuel for various transportation modes such as cars, trucks, and marine vessels, as well as for heating systems like boilers, cookstoves, and kilns, among other emerging market applications. The versatility of methanol is underscored by its presence in numerous ubiquitous household products, indispensable components for automobiles, and the manufacturing of other valuable chemicals. This versatility stems from its ability to be derived from diverse feedstocks, including natural gas, waste, and captured CO₂ combined with green hydrogen [24].

Furthermore, there is a shifting perception of methanol from being merely a petrochemical to being recognized as a clean and sustainable fuel. Its inherent clean-burning properties result in reduced emissions and improved fuel efficiency during combustion in land and marine vehicles. Moreover, when produced from renewable feedstocks such as captured CO₂ or waste, methanol transitions into a net carbon-neutral fuel, aligning with climate change policies aimed at mitigating greenhouse gas emissions [24].

However there are also some concerns towards the toxicity of methanol and therefore its use in certain applications. Methanol toxicity arises from its metabolism into formate, which is responsible for acidosis, blindness and possible death [25], [26].

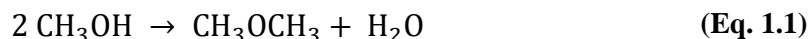
1.3.1 Applications

The primary utilization of methanol is within the chemical market, with a significant portion, approximately 35%, directed towards formaldehyde production. Additionally, the remaining quantities find application in various sectors, including the manufacturing of fuel additives, acetic acid, methyl and vinyl acetates, and other chemical compounds [27]. Notably, there has been a notable surge in the demand for methanol synthesis, positioning it as the second-largest consumer of hydrogen, following ammonia production [28].

1.3.1.1 Conversion to dimethyl ether (DME)

In the realm of technological advancements, the utilization of methanol as a fundamental C1 building block within the petrochemical industry stands out as one of the most promising developments. DME, an alternative fuel derived from methanol, represents a significant portion of methanol production. This fuel exhibits characteristics akin to diesel fuel, with a close cetane number and ignition temperature. Notably, DME offers advantages such as reduced NO_x emissions, diminished smoke, and minimized engine noise compared to traditional diesel engines. Moreover, its ease of transportability adds to its appeal in various applications [29], [30].

Additionally, DME finds utility as a chemical feedstock in the production of various products, including short olefins such as ethylene and propylene, gasoline, hydrogen, acetic acid, and dimethyl sulphate. The contemporary manufacturing process for DME entails a double-step (indirect) synthesis. Initially, methanol synthesis is undertaken, followed by dehydration as in **Eq. 1.1**.



According to estimates, the Dimethyl Ether (DME) Market is projected to be approximately 4,92 million tons in size by 2024 and is anticipated to expand to about 7,48 million tons by 2029. This growth represents a Compound Annual Growth Rate (CAGR) of 8,76% over the forecast period spanning from 2024 to 2029 [31].

1.3.2 Hydrogen production

Hydrogen is widely recognized as a clean energy vector with pivotal roles in refining, the chemical industry, and electronics. However, as highlighted in the introduction, its storage and transportation present significant challenges, limiting its widespread application. An alternative approach involves producing hydrogen from easily transportable liquid feedstocks, with methanol emerging as a promising option [27]. Methanol is valued for its attributes as a liquid hydrogen source, characterized by low toxicity and minimal chain-alcohol content [32].

Consequently, numerous research groups are actively exploring various technologies utilizing methanol in hydrogen production [27]. These advancements span several thermochemical methods, including direct decomposition [32], [33], [34], steam reforming reactions [35], [36], [37], [38], [39] and partial oxidation [40], alongside methanol-water solution electrolysis [41], [42].

The mentioned technologies will not be elaborated upon as they are beyond the scope of this thesis.

1.3.3 Methanol fuel cells

In today's era, there is a continuous rise in the prevalence of systems reliant on an external power source for charging, such as electric cars and bikes, smartphones, laptops and portable speakers. Consequently, researchers are actively seeking viable solutions based on rechargeable batteries, specifically those composed of lithium (Li) and nickel (Ni). Efforts are underway to implement this technology from an energy perspective, with a particular focus on eliminating the need for external charging sources as in fuel cells [27].

One such technology under investigation is the Proton Exchange Membrane (PEM) fuel cell, an electrochemical device designed to convert chemical energy into electrical energy. Within the realm of PEMFCs, the direct methanol fuel cell (DMFC) stands out. The DMFC utilizes methanol or methanol solutions as fuel and operates at ambient temperatures [43]. This system bears resemblance to methanol-water solution electrolysis, presenting a promising avenue for self-sustaining energy systems.

The exact functioning of these cells will not be discussed further as it is beyond the scope of this thesis.

1.3.4 Other applications

Some chemical applications of methanol include its reaction with oxygen to produce formaldehyde [44], [45]. Additionally, methanol can form acetic acid when combined with carbon monoxide [46], [47]. Furthermore it can react with ammonia to yield mono-, di-, and trimethylamine [48], [49].

Moreover, another important application is in the Methanol-to-Olefins (MTO) process, where methanol is converted into light olefins like ethylene and propylene, which are essential raw materials for the chemical industry. This process involves dehydration to dimethyl ether, followed by passing the mixture of methanol and dimethyl ether over a catalyst at high temperatures, typically consisting of a crystalline aluminium silica zeolite (either synthetic or natural, such as erionite and chabazite) [50], [51].

Additionally, the Methanol-to-Gasoline (MTG) process aims at producing higher hydrocarbons from methanol, which can serve as fuel for gasoline engines. This process resembles the MTO process, but the light olefins undergo further conversion into higher hydrocarbons, including alkanes, alkenes, and naphthenes [52], [53], [54].

1.4 Methane-to-methanol

Methanol production from methane, also known as methane-to-methanol (MTM) conversion, is a significant area of interest in the chemical industry due to the abundance of methane, often sourced from natural gas reserves or renewable biogas. The direct conversion of methane to methanol is highly desirable as methanol serves as a versatile chemical feedstock and fuel precursor.

Traditional methods for methanol production involve a multi-step process, with syngas (a mixture of hydrogen and carbon monoxide) being the primary intermediate. However, direct conversion methods aim to streamline this process by bypassing the syngas stage, thereby potentially reducing costs and energy consumption. One of the challenges in methane-to-methanol conversion is overcoming the high stability nature of methane's C-H bonds. This requires the development of efficient catalysts and reaction conditions that can activate methane molecules and facilitate their conversion to methanol selectively.

Several approaches are being explored for methane-to-methanol conversion, including biological processes using enzymes such as methane monooxygenase (MMO), thermochemical processes employing high temperatures and pressures, and catalytic processes utilizing heterogeneous catalysts. Recent advancements in catalyst design have shown promise in activating methane and promoting its conversion to methanol under milder reaction conditions. Additionally, innovative reactor designs and process optimization strategies are being investigated to improve the overall efficiency and selectivity of the methane-to-methanol conversion process.

Overall, the development of efficient and sustainable technologies for methane-to-methanol conversion holds great potential for meeting the growing demand for methanol as a chemical feedstock and clean energy carrier, while also contributing to the utilization of abundant methane resources and reducing greenhouse gas emissions.

1.4.1 Direct Oxidative Methane Conversion

Direct oxidative methane conversion involves the direct oxidation of methane to methanol using oxygen or air as the oxidant. This approach aims to bypass the conventional syngas route, offering potential advantages in terms of process simplicity and energy efficiency.

1.4.1.1 High-temperature route based on homogeneous radical gas phase reactions

Gas-phase reactions occur due to a free radical mechanism at high temperature and pressure [55]. Thermodynamic and kinetic analyses have revealed that the partial oxidation of methane is the rate-limiting step, primarily due to the formation of methyl radicals. Initiators and sensitizers are introduced into the reaction mixture to decrease the energy barrier of H-abstraction. Barbero et al. [56] introduced nitrous oxide as a novel initiator to promote the gas-phase reaction with methane, while Tabata et al. [57] compared the effectiveness of oxygen and nitrous oxide for this purpose. Fujimoto [58] reported that consuming small quantities of hydrocarbons, such as ethane, indicated a lower initiation temperature and increased selectivity and yield of methanol.

High methane conversion to methanol can also be achieved under non-catalytic reaction conditions. The process begins at 350 °C and increases to 500 °C under fuel-rich mixtures with the oxidant to minimize combustion reactions. However, this method tends to lower methanol selectivity [55]. Some researchers have investigated non-catalytic gas-phase reactions, achieving methane conversion rates from 10% to 80% [59], [60].

1.4.1.2 Low temperature catalytic route involving heterogeneous catalysis

Developing an active and selective catalyst is crucial for the partial oxidation conversion of methane to methanol, particularly as gas-phase operations pose challenges in controlling selectivity and necessitate high operating pressures. At lower pressures, such as 1 atm, the catalyst selection significantly impacts yield. Various catalysts have been explored to enhance catalytic performance, such as optimizing catalytic activity with slightly reduced states by storing isolated metal oxides on a silica substrate [55]. Tabata et al. [61] proposed a method involving the insertion of oxygen into CH₃ from the first H-abstraction molecules of methane through reduction of molybdenum and vanadium to their oxides (MoO₃ and V₂O₃).

Also the formation of a silicomolybdic acid (SMA)-like structure on a MoO₃/SiO₂ catalyst, which promoted the successive oxidation of methanol and increased oxygenate production during methane partial oxidation was observed by Aoki et al. [62]. Sohrabi et al. [63] optimized a V₂O₅/SiO₂ catalyst using a computational fluid dynamics (CFD) mathematical model for stimulated direct methane-to-methanol conversion in a Fixed-Bed Reactor. While Zhang et al. [64] prepared lanthanum cobalt oxide impregnated with varying amounts of a (NH₄)₆Mo₇O₂₄ aqueous solution, demonstrating good activity in methane partial oxidation. On the other hand Zhang et al. [65] achieved high methanol production without catalysts. Catalysts based on iron have also shown promise, with Fe³⁺ species impregnated on copper iron pyrophosphate catalysts exhibiting high reactivity for selective oxidation of methane to methanol. Additionally, ZSM-5 zeolite supported catalysts, modified with iron or cobalt impregnation, have demonstrated significant methane conversion and methanol yield improvements [66], [67], [68], [69], [70].

Furthermore, the utilization of metal-organic frameworks in methane to methanol conversion presents a promising avenue for sustainable catalysis. MOFs are crystalline materials composed of metal ions or clusters coordinated with organic ligands, forming a porous structure with a high surface area. Their tuneable properties make them attractive candidates for catalytic applications, including methane conversion to methanol. Several studies have investigated the feasibility and efficiency of MOFs in this conversion process. By leveraging the unique properties of MOFs and optimizing catalytic sites, researchers aim to develop efficient and selective catalysts for this industrially significant process, contributing to the advancement of clean energy technologies and environmental sustainability [71], [72], [73], [74].

1.4.1.3 Homogeneous catalysis in solution

The conversion of methane to methanol can also be achieved through homogeneous catalysts under low-temperature conditions in solution. Unlike heterogeneous catalysts operating at high temperatures, this method does not involve radicals in the activation of C-H bonds, potentially leading to more selective reactions. By controlling parameters such as temperature, CH_4/O_2 ratio, OH concentration, and residence time, higher conversion rates can be attained. Notably, temperatures around 100°C have been found to be optimal for maximum conversion [75].

Several catalysts have been explored for this approach. For instance, Shilov et al. [76] utilized Pt (II) and Pt (IV) complexes, contributing to this field since the 1970s. Periana et al. [77], [78] developed oxidation catalysts based on Pt (II), Pd (II), and Hg (II) salts, including bipyridyl platinum (II) complex, which effectively functionalizes C-H bonds to yield partially oxidized products. PtCl_2 catalyses the selective oxidation of methane in fuming sulfuric acid, resulting in methyl bisulphate, which can be hydrolysed to methanol. However, using H_2SO_4 as a solvent poses challenges in methanol separation and necessitates expensive corrosion-resistant materials [75].

Rahman et al. [79] improved catalyst performance using strong oxidizing agents like SO_3 , $\text{K}_2\text{S}_2\text{O}_8$, and NaIO_4 . Li et al. [80] achieved methane conversion of 24,9%, with a selectivity of up to 71,5% and methanol yield of 17,8% by employing a gold nanoparticle $[\text{Au}/\text{SiO}_2]$ catalyst in ionic liquids as solvents. $\text{Pd}(\text{OAc})_2$ -p-benzoquinone-CO catalyst and Co-ZSM-5 zeolite catalysts have also been explored, with the latter showing selectivity towards methanol due to the presence of cobalt in ion-exchange positions. Additionally, a Cu-ZSM-5 zeolite catalyst exhibited over 98% selectivity when oxygen was used as the oxidizing agent [75].

1.4.2 Thermochemical Methane Conversion

Thermochemical methane conversion involves the use of heat and chemical reactions to convert methane to methanol. This pathway typically begins with steam reforming of methane to produce synthesis gas (syngas), which is then catalytically converted to methanol. Other thermochemical routes, such as partial oxidation or gasification of methane, may also be used to produce syngas for subsequent methanol synthesis.

Methanol is industrially produced from natural gas through a process involving steam reforming, followed by conversion and distillation of the resulting gas mixture. The production of methanol typically involves an equilibrium reaction system with intercooler multistage reactors to achieve higher conversion rates [81]. Recent efforts by researchers focus on methanol production from carbon dioxide, utilizing CO_2 gas as a potential feedstock [82]. During production, the reaction system is exothermic with a limited equilibrium state, prompting efforts to improve process yield by in situ removal of methanol from production sites to enhance conversion efficiency. Researchers are exploring process intensification through the integration of membrane separation into methanol production reactors, with membrane reactors emerging as a promising option for methanol synthesis and separation [83], [84].

A promising approach for methanol production involves converting natural gas directly into methanol without the need for syngas intermediates. Given the abundant availability of natural gas, especially methane, found in reservoirs and subarctic tundra, converting methane to methanol presents significant challenges due to the need to activate the C-H bond [85]. Methane molecules are structured in perfect tetrahedrons with uniform C-H bonds, and the oxidation of CO and H_2 during the conversion process can lead to unwanted CO_2 and water formation.

Efficiency in conversion processes can be improved in modern plants by utilizing the released heat for steam reforming tasks and partially oxidizing methane with O_2 and reform steam [86], [87]. However, syngas production processes face various operating design and economic limitations, particularly in regulating the H_2/CO ratio, which can be unstable and problematic [88]. The complex operating conditions, including the need for elevated temperatures and harsh processes, such as high and low water-gas shift (WGS) reactors, can lead to operational issues and reduce the economic efficiency of methanol production from synthesis gas as a feedstock [88], [89].

1.4.3 Plasma-Assisted Methane Conversion

Plasma-assisted methane conversion employs electric discharges to activate methane molecules and facilitate their conversion to methanol. This approach operates at relatively low temperatures and pressures, offering potential advantages in terms of energy efficiency and process control. Investigating plasma-catalyst interactions and optimizing reactor design could enhance the efficiency and selectivity of methane conversion to methanol.

The oxidation of methane to methanol can be accomplished under plasma conditions, typically at atmospheric gas pressure. Plasma, often referred to as the fourth state of matter, consists of positive ions, negative ions, electrons, and neutral species. Reddy et al. [90] noted the wide-ranging applications of plasma, including the oxidative decomposition of methane. Plasma technology can be categorized into thermal plasma and non-thermal plasma. Roth [91] extensively discusses both conditions, with thermal plasma comprising highly excited atoms, ions, and radicals, while non-thermal plasma, also known as low-supplied power plasma, is characterized by electrons with significantly higher energy than surrounding particles.

Okazaki et al. [92] demonstrated the conversion of methane to methanol using non-equilibrium plasma chemical reactions under atmospheric pressure, employing ultra-short pulsed barrier discharge in an extremely thin glass tube reactor. Diverse designs for plasma reactors have been proposed to enhance methane conversion to methanol. Larkin et al. [93] utilized a dielectric barrier discharge (DBD) reactor for methanol synthesis from methane, akin to a catalytic reactor, enabling control over reaction temperature, pressure, and product selectivity. Nozaki et al. [94] reported on a single-step, non-catalytic synthesis of methanol via methane partial oxidation at room temperature using a new non-thermal discharge micro-reactor, achieving one-pass methane conversion of 40% with selectivity for useful oxygenates. Additionally, Wang et al. [95] conducted non-catalysed reactions in an argon environment using a radiofrequency plasma system, with the CH₄/O₂ plasma system exhibiting higher methanol composition and conversion rates. Furthermore, Tsuchiya et al. [96] studied low-pressure discharge without catalysis in low-pressure steam plasma, exploring different discharge parameters to optimize methane conversion. The integration of non-thermal plasma with catalysts has shown promise, with recent studies employing Cu-doped Ni supported on CeO₂ enhancing methanol selectivity [97]. Additionally, efforts to combine multicomponent catalysts with plasma, either in-plasma catalysis (IPC) or post-plasma catalysis (PPC) configurations, aim to achieve high levels of methane conversion and methanol selectivity through synergistic effects [98].

1.4.4 Biological Methane Conversion

Biological methane conversion utilizes microbial fermentation or enzymatic reactions to convert methane to methanol. Certain microorganisms, such as methanotrophic bacteria, possess enzymes like methane monooxygenase (MMO) capable of oxidizing methane to methanol. Understanding the metabolic pathways and optimizing conditions for microbial or enzymatic methane conversion could provide insights for bio-based methanol production.

Methane monooxygenase (MMO) enzymes represent natural catalysts with the potential to facilitate the direct conversion of methane to methanol under ambient or physiological conditions [68]. Lunsford [99] made significant strides in methane conversion technology by uncovering the ability of MMO enzymes to form oxygenates such as methanol. These enzymes activate O₂ at iron centres with the assistance of a reductant like NADH. Michalkiewicz [100] investigated the partial oxidation of methane to formaldehyde and methanol using zeolite catalysts, such as Fe-ZSM-5 and Fe-NaZSM-5, alongside MMO enzymes. The activation of methane over Fe-ZSM-5 mirrors methane activation within MMO during methanotrophic bacteria catalysis. Studies conducted by Razumovsky et al. [101] explored another biocatalyst based on *Methylosinus sporium* B-2121 bacteria cells for converting methane to methanol through biochemical processes.

1.4.5 Hybrid and Integrated Processes

Hybrid and integrated processes in methane-to-methanol conversion involve combining multiple conversion steps or technologies to enhance overall efficiency and methanol yield. These approaches leverage synergies between different pathways to overcome individual limitations and maximize process benefits. For example, integrating biological and catalytic conversion steps or combining thermochemical and plasma-assisted methods could offer synergistic advantages. Designing integrated process schemes and assessing their techno-economic feasibility are critical aspects of research in this area, aiming to develop sustainable and efficient methanol production technologies for future applications.

1.5 Intended methodology

1.5.1 Parallel researched technique

As mentioned in 1.1.2.2 the parallel researched technique has as objective to convert propane to propanol in a continuous flow reactor. This is a direct oxidation technique which uses MOFs as catalysts and N_2O gas as oxidising agent.

1.5.1.1 Activation

In the parallel researched technique, the metal-organic framework, specifically MIL-100, undergoes in situ activation at $240^\circ C$ and 1 atm. This process of in situ activation holds paramount significance as it notably diminishes the likelihood of deactivation. Through this controlled activation procedure, the MOF's structural integrity and catalytic activity are preserved, ensuring sustained performance over extended reaction periods. The conditions of $240^\circ C$ and 1 atm serve as ideal parameters for activating the MIL-100 MOF. In literature, activation commonly occurs under vacuum conditions [102], yet it is deemed unnecessary for activating the MOF currently utilized.

1.5.1.2 Oxidation

At the specified conditions of $200^\circ C$ and 5 bar pressure, the oxidation reaction proceeds within the system. In this process, both the oxidant, nitrogen dioxide (N_2O), and the reagent, propane, are introduced into the column simultaneously. The oxidation mechanism by N_2O of active Fe-sites can be found in Figure 3 [103], while the overall oxidation idea for MIL-100 is shown in Figure 4 [104]. As the reaction progresses, propane undergoes oxidation to produce propanol, which is then expected to exit the reactor after its desorption from the corresponding catalytic sites. In the exceptional case that propanol does not leave the column immediately, desorption must be forced using water vapour injection.

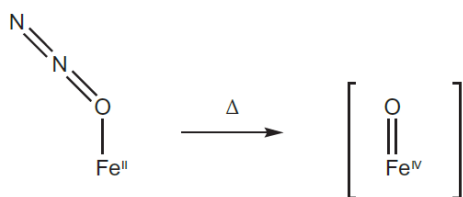


Figure 3: Oxidation active Fe site

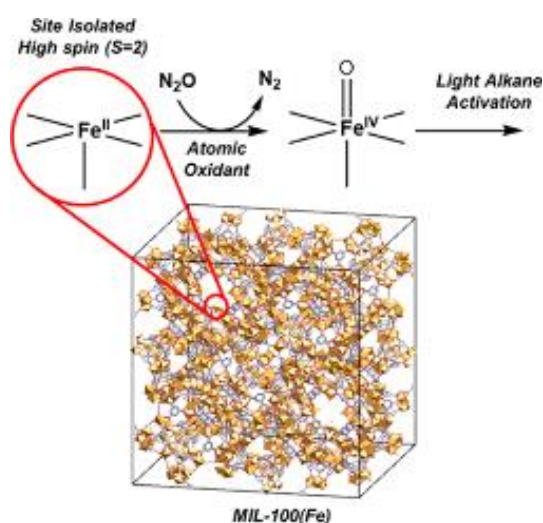


Figure 4: Oxidation active site MIL-100

1.5.1.3 Desorption

Only if needed, desorption will be done by H₂O at 200°C and 1 atm. The aim of this procedure is to replace the propanol that is still bound to the active sites by water. By doing so the propanol will leave the column.

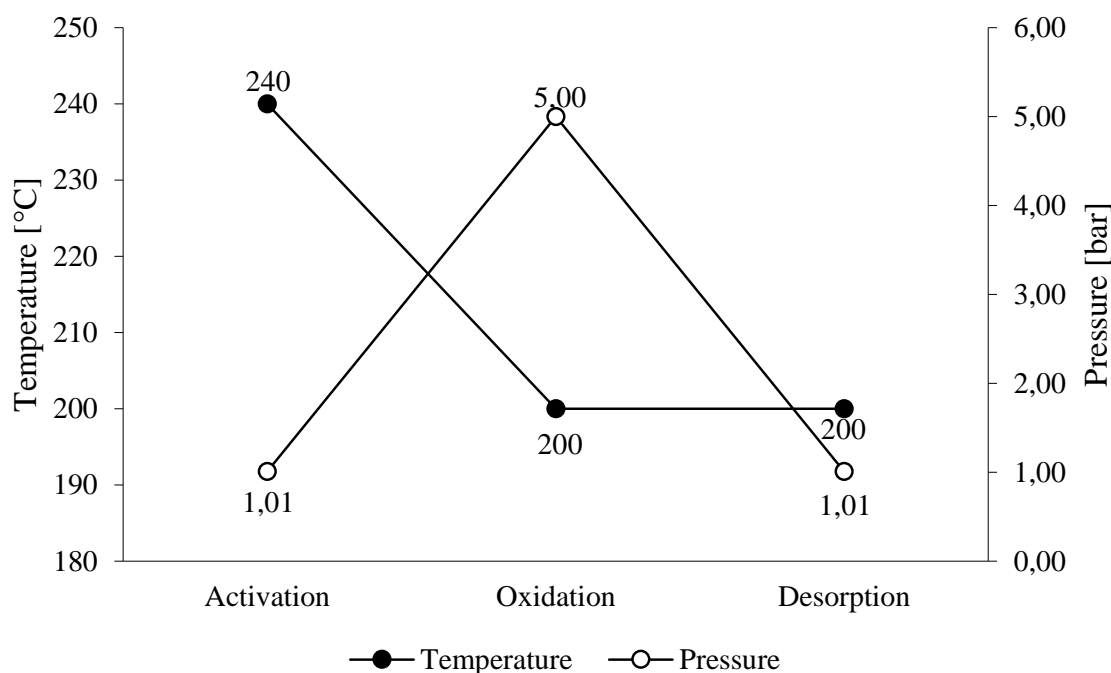


Figure 5: Operation conditions or the different stages in the parallel researched technique

1.5.2 Process under development

The methodology employed by the 'DEMO project' partnership involves utilizing both metal-organic frameworks (MOFs) and enzymes to facilitate the conversion of methane to methanol. However, in the DEMO project, two distinct strategies are being investigated. The first involves supporting new and enhanced enzymes on MOFs, while the second approach, which aligns with this master thesis' work, focuses on mimicking the active moieties of enzymes within MOFs. Specifically, the MOFs used in this master thesis do not contain enzymes; rather, they replicate the behaviour of iron ions and their chemical environments, mimicking the active sites of enzymes capable of selectively oxidizing hydrocarbons to alcohols. These mechanisms are evaluated under continuous gas flow conditions, resembling a plug flow reactor (PFR) concept. In both cases the research team employs N₂O as the oxidizing agent, with the reactor operating at a pressure of 5 bar. Despite the relatively low operating temperature of 200°C, which aligns with the innovative approach of methane oxidation to methanol at mild conditions, as stated earlier. Another notable distinction from the current industrial techniques, as discussed in section 1.4.2, is that methanol formation results directly from the oxidation of methane. This novel approach to industrial methanol production from methane is expected to offer greater economic efficiency compared to existing techniques, owing to its enhanced energy efficiency and reduced equipment requirements.

1.5.2.1 Components

a) Reagents

It is not necessary to discuss methane as this has already been extensively covered in 1.2. However, it is certainly useful to extensively mention N₂O as the oxidant in this reaction.

When considering gas-phase catalytic oxidation by N₂O, it's important to recognize both the significant potential of nitrous oxide as a selective oxygen donor and the challenges that often arise when attempting to capitalize on this potential. The primary obstacle is the slow desorption of the desired hydroxylated product from the catalyst. To address this issue, increasing the temperature is typically necessary, but this can result in side reactions within zeolites and catalyst deactivation due to coking [105].

b) Products

Since methanol, the main product of the studied reaction, has been extensively covered in **1.3**, further discussion on it is unnecessary. However, it is pertinent to address the by-products such as CH₃OH, CH₃OCH₃, CH₂O, CO, and CO₂, N₂ [73]. All of these carbon molecules originate from the over-oxidation of methane. Nitrogen gas, on the other hand, is formed because N₂O previously oxidized the framework, resulting in the loss of an oxygen atom.

During the oxidation of methane, it commonly progresses beyond methanol due to the intricate chemistry involved. This oxidation process typically initiates with the abstraction of hydrogen atoms from methane molecules, forming methyl radicals (CH₃•). These radicals exhibit high reactivity and can undergo various subsequent reactions with oxygen-containing species or other radicals. As a result, a multitude of intermediate compounds are generated, including formaldehyde (CH₂O), formic acid (HCOOH), carbon monoxide (CO), carbon dioxide (CO₂), and a diverse array of oxygenates [106].

The complexity of methane oxidation arises from the interplay of multiple factors, including reaction conditions (such as temperature, pressure, and residence time), catalyst characteristics, and the presence of co-reactants or catalyst promoters. These factors collectively influence the selectivity and distribution of oxidation products. Consequently, the oxidation of methane yields a spectrum of products beyond methanol, reflecting the diverse reaction pathways and competing transformations involved in this process.

c) Reaction conditions

Continuous flow

For the conversion of methane to methanol, the research group will employ a continuous flow system. Working in continuous flow offers several advantages over batch processes. Firstly, it allows for a steady and consistent supply of reactants, leading to more stable reaction conditions and improved control over reaction parameters. Additionally, continuous flow systems often result in higher product yields and selectivity due to better mixing and enhanced mass transfer. Furthermore, continuous flow operations are typically more efficient in terms of energy and resource utilization, as they minimize downtime between batches and require less manual intervention. Overall, adopting a continuous flow approach enables the research group to achieve greater productivity, reproducibility, and efficiency in the conversion of methane to methanol.

Temperature

Working at a temperature of 200°C offers several advantages for the conversion of methane to methanol. Firstly, this temperature falls within a range that facilitates the activation of methane molecules, allowing them to react more readily with other reagents. Additionally, operating at 200°C ensures that the reaction proceeds at a reasonable rate without excessively high energy requirements.

Moreover, this temperature provides an optimal balance between reaction kinetics and energy consumption, making the process more efficient. At 200°C, the reaction can achieve high conversion rates while minimizing the formation of unwanted by-products. Additionally, the chosen temperature allows for better control over the reaction conditions, ensuring reproducibility in the production process.

Furthermore, working at 200°C offers practical advantages in terms of equipment and infrastructure. Many industrial-scale reactors and heat exchange systems are designed to operate efficiently within this temperature range, reducing the need for costly modifications or specialized equipment. Overall, the decision to work at 200°C reflects a careful consideration of both technical and practical factors to optimize the methane-to-methanol conversion process.

Pressure

Operating at a pressure of 5 bar offers several advantages for the conversion of methane to methanol. Firstly, this pressure level provides sufficient driving force for the reaction to proceed efficiently while maintaining a manageable system. Higher pressures increase the concentration of reactants, promoting

collisions between molecules and enhancing reaction rates. Moreover, working at 5 bar allows for better control over the reaction conditions, ensuring that the desired chemical transformations occur with high selectivity. By carefully adjusting the pressure, researchers can optimize the yield of methanol while minimizing the formation of undesired by-products.

Additionally, operating at this pressure facilitates the use of standard equipment and infrastructure commonly available in industrial settings. Many reactors and processing units are designed to operate safely and efficiently within the 5-bar pressure range, reducing the need for specialized or custom-built equipment. Furthermore, the chosen pressure level offers practical advantages in terms of scalability and process economics. Operating at 5 bar allows researchers to develop and assess methane-to-methanol conversion processes on a laboratory scale with confidence that the results can be scaled up to industrial production levels without significant modifications.

Overall, working at a pressure of 5 bar provides a balance between reaction kinetics, safety, and practical considerations, making it an optimal choice for the research group's efforts to convert methane to methanol.

d) Metal-organic frameworks

MIL-100(Fe) is a metal-organic framework (MOF) composed of iron ions coordinated with organic ligands. In the case of *MIL-100(Fe)*, the organic ligand is benzene-1,3,5-tricarboxylate (BTC), also known as trimesic acid. This MOF exhibits a large-pore structure with permanent porosity, making it suitable for various applications such as gas storage, catalysis, and separation. *MIL-100(Fe)* is synthesized through hydrothermal methods and has been studied extensively due to its unique properties and potential practical uses [107].

HKUST-1, also known as Cu-BTC or MOF-199, is a type of metal-organic framework (MOF) composed of copper (Cu) ions coordinated with benzene-1,3,5-tricarboxylate (BTC) ligands [108]. The name "HKUST-1" is derived from the Hong Kong University of Science and Technology (HKUST), where it was first synthesized [109]. This MOF exhibits a three-dimensional porous structure with high surface area and tuneable pore size, making it suitable for various applications such as gas storage, separation, catalysis, and sensing. *HKUST-1* has been widely studied and utilized in scientific research and industrial applications due to its unique properties and versatility [110].

MOF-808 is a type of metal-organic framework (MOF) composed of zirconium (Zr) ions coordinated with trimesic acid ligands [111]. *MOF-808* exhibits a three-dimensional porous structure with high surface area and tuneable pore size, making it suitable for various applications such as gas storage, separation, catalysis, and sensing. This MOF has been of particular interest in recent years due to its potential in diverse fields of research and industrial applications [112]. However, in this thesis a modified version of this MOF will be used, more specifically *MOF-808 @His-Cu*.

MOF-808 @His-Cu is a *MOF-808* functionalised with histidine and copper doped. Adding copper sites to a *MOF-808* serves a crucial purpose in catalysis. Copper ions function as active catalytic centres, enhancing the material's ability to facilitate various chemical reactions. By incorporating copper sites into *MOF-808*, the catalytic activity of the material can be significantly improved, making it more effective in promoting specific reactions. This enhancement in catalytic performance opens opportunities for *MOF-808* to be used in a wide range of catalytic applications, including oxidation, reduction, and coupling reactions. With copper sites present, *MOF-808* becomes a versatile catalyst capable of driving diverse chemical transformations with high efficiency and selectivity [113]. This catalytic functionality makes copper-modified *MOF-808* a promising candidate for catalytic processes in industries such as pharmaceuticals, fine chemicals, and environmental remediation [114].

e) Enzymes

Enzymes are not used in the parallel researched technique as it focuses on the oxidation of alkanes solely using MOF's. However the use of enzymes, more specifically MMO, is part of the process under development as earlier mentioned in 1.1.1. Methane monooxygenase (MMO) is a key enzyme involved

in the conversion of methane to methanol, playing a crucial role in the biological oxidation of methane. There are two main forms of MMO: soluble methane monooxygenase (sMMO) and particulate methane monooxygenase (pMMO).

sMMO is a cytoplasmic enzyme found in certain bacteria and archaea. It consists of three components: a reductase, a hydroxylase, and a regulatory protein. The hydroxylase component contains a di-iron active site responsible for catalysing the oxidation of methane to methanol. sMMO operates under mild conditions and exhibits high selectivity for methane oxidation [115], [116].

pMMO, on the other hand, is a membrane-bound enzyme found in methanotrophic bacteria. It is composed of a trimeric structure and contains a copper active site responsible for methane oxidation. The exact mechanism and structure of pMMO are still being elucidated, but recent research suggests that it plays a crucial role in methane oxidation in certain bacterial species [115], [117].

Understanding the mechanisms and properties of MMO enzymes is essential for developing efficient biocatalysts for the conversion of methane to methanol. By engineering and optimizing MMO enzymes, researchers aim to enhance catalytic activity, stability, and selectivity, ultimately contributing to the development of sustainable and efficient methods for methane conversion in industrial processes.

1.5.2.2 Difficulties

Oxidizing methane to methanol directly using metal-organic frameworks (MOFs) impregnated with methane monooxygenase (MMO) enzymes presents several challenges and limitations:

Enzyme stability: One major challenge is maintaining the stability of the MMO enzymes within the metal-organic frameworks (MOFs). Enzymes can be sensitive to various environmental factors such as temperature, pH, and the presence of inhibitors. Ensuring that the enzymes remain active and stable under the reaction conditions for an extended period is crucial for sustained catalytic activity.

Mass Transfer Limitations: Another significant issue is the diffusion of methane and oxygen molecules through the porous structure of the MOFs to reach the active sites of the MMO enzymes. The size and structure of the pores in the MOFs can influence the rate of mass transfer, potentially leading to diffusion limitations and reduced reaction rates.

Selective Activation of Methane: Methane is chemically inert under normal conditions, requiring elevated temperatures and pressures or the presence of catalysts to activate its C-H bonds selectively. Ensuring selective activation of methane while minimizing over-oxidation to other by-products is a significant challenge.

Product Separation: Methanol production from methane typically involves multiple reaction steps, leading to a mixture of products. Separating methanol from other by-products efficiently can be challenging and may require additional purification steps, impacting the overall process economics.

Optimization of Reaction Conditions: Finding the optimal reaction conditions, including temperature, pressure, and reactant concentrations, is essential for maximizing the conversion of methane to methanol. The reaction conditions must be carefully controlled to balance the rate of methanol production with the selectivity of the reaction and the stability of the enzymes.

Catalyst Deactivation: Over time, the MMO enzymes may undergo deactivation or denaturation, leading to a decline in catalytic activity. Factors such as enzyme degradation, fouling of active sites by reaction intermediates or by-products, and chemical instability of the MOF support material can contribute to catalyst deactivation. Strategies to mitigate catalyst deactivation, such as enzyme immobilization techniques or the use of stabilizing agents, are essential for maintaining long-term catalytic performance.

Scale-up Challenges: Transitioning from laboratory-scale experiments to industrial-scale production presents additional challenges. Scaling up the methane-to-methanol conversion process requires addressing issues such as reactor design, mass transfer limitations, and process integration. Ensuring the scalability and economic feasibility of the process is critical for its commercial viability.

Cost Considerations: Enzyme production, MOF synthesis, and process operation can be costly. Balancing the costs of enzyme immobilization, MOF fabrication, and process optimization against the potential benefits of direct methane oxidation to methanol is critical for assessing the feasibility of the technology from an economic standpoint.

Overall, while direct oxidation of methane to methanol using MOFs impregnated with MMO enzymes holds promise as a sustainable and efficient approach, overcoming these challenges and limitations will require interdisciplinary research efforts and technological advancements. By addressing these difficulties and limitations through careful design and optimization of the catalytic system, it may be possible to develop an efficient and sustainable process for directly oxidizing methane to methanol using metal-organic frameworks impregnated with MMO enzymes. Therefore this thesis aims to contribute to the removal of some of the above mentioned difficulties, such as selective activation and optimization of reaction conditions.

1.6 Research methodology

The parallel researched technique, which converts propane to propanol in a continuous flow reactor operating in the gas phase, and the research methodology in this thesis, which transforms hexane to hexanol in a batch reactor with liquid reagents, share commonalities and distinctions. Both processes involve the oxidation of alkanes to alcohols, utilizing different oxidizing agents— N_2O gas in the former and H_2O_2 in the latter. Despite this difference, both approaches allow for control over several parameters such as temperature, pressure and reaction time, facilitating similar reaction conditions.

While the continuous flow reactor in the parallel researched technique enables a steady supply of reactants and efficient gas-phase reactions, the batch reactor operates with liquid reagents, offering a different mode of reaction control. Furthermore, the choice of the oxidizing agent differs between the two methods, potentially influencing reaction kinetics and product selectivity.

Nevertheless, both experiments aim to elucidate the underlying reaction mechanisms and optimize conditions for efficient alkane oxidation. By exploring the similarities and differences between these approaches, valuable insights can be gained into the fundamental principles governing alkane oxidation reactions. Additionally, understanding the nuances of each method contributes to the broader knowledge base of chemical synthesis and process optimization, ultimately advancing the field of catalysis.

1.6.1 Components

1.6.1.1 Reagents

a) Hexane

Hexane, a highly flammable liquid hydrocarbon, is a colourless and odourless alkane with the chemical formula C_6H_{14} . It belongs to the family of alkanes and is composed of six carbon atoms bonded together in a straight chain, with 14 hydrogen atoms completing its structure. Hexane is commonly found in petroleum and natural gas, and it is produced as a byproduct of crude oil refining and natural gas processing. Due to its low boiling point of approximately $68,7^\circ C$ and its relatively low toxicity, hexane is widely used as a solvent in various industrial processes, including extraction, cleaning, and degreasing. It is also utilized as a component in the formulation of glues, adhesives, and coatings. Additionally, hexane serves as a valuable reagent in organic synthesis, particularly in reactions involving alkane transformations [118], [119].

b) Hydrogen peroxide

Hydrogen peroxide (H_2O_2) is a versatile oxidizing agent commonly used in various chemical processes and industrial applications. It is a clear, colourless liquid with a slightly acidic taste and a distinctive odour. Chemically, hydrogen peroxide consists of two hydrogen atoms and two oxygen atoms arranged in a peroxide bond, giving it the formula H_2O_2 .

One of the key characteristics of hydrogen peroxide is its ability to release oxygen when it decomposes, making it a powerful oxidizing agent. This property allows hydrogen peroxide to react with a wide range of organic and inorganic compounds, facilitating oxidation reactions that lead to the formation of new products.

In the context of this study, hydrogen peroxide will be employed as the oxidizing agent for the direct oxidation of hexane to hexanol. Starting from a concentration of 35 v%, hydrogen peroxide will be diluted to test lower concentrations, allowing for the examination of its effect on the oxidation reaction. Additionally, the ratio of hydrogen peroxide to hexane will be varied to assess its impact on reaction kinetics and product selectivity.

The use of hydrogen peroxide offers several advantages, including its relatively low cost, ease of handling, and environmentally friendly nature. Moreover, hydrogen peroxide can selectively oxidize organic compounds without producing harmful byproducts, making it a preferred reagent for many oxidation processes [120], [121].

1.6.1.2 Products

a) Hexanol

Hexanol is a six-carbon alcohol with the chemical formula $\text{C}_6\text{H}_{14}\text{O}$. It is a colourless liquid with a characteristic odour and is commonly found in various natural sources such as fruits, flowers, and essential oils. Hexanol is primarily used as a solvent in industries such as paints, coatings, and pharmaceuticals due to its ability to dissolve a wide range of substances.

In the context of this study, hexanol serves as the desired product of the oxidation reaction of hexane. Through the oxidation process, hexane is converted into hexanol, offering a valuable intermediate compound with numerous potential applications. Hexanol is particularly valuable as a precursor in the synthesis of plasticizers, flavouring agents, and fragrances.

The direct conversion of hexane to hexanol presents several challenges and requires careful optimization of reaction conditions, including temperature, pressure, and choice of catalyst. By studying the conversion process and analysing the factors influencing product yield and selectivity, valuable insights can be gained into the fundamental mechanisms of alkane oxidation and catalyst design.

Hexanol's versatility and wide range of applications make it a valuable compound in various industries, and understanding its production through direct oxidation processes contributes to advancements in sustainable chemical synthesis and process optimization. Additionally, the utilization of hexanol as a renewable and environmentally friendly alternative to traditional petrochemical-derived compounds aligns with efforts to promote greener and more sustainable chemical processes [122], [123].

b) Over-oxidation products

The over-oxidation of hexane, the process by which hexane is subjected to excessive oxidation conditions, can lead to the formation of various byproducts in addition to the desired hexanol. These byproducts may include:

Ketones: Over-oxidation of hexane can result in the formation of ketone compounds, such as hexanone or higher molecular weight ketones. Ketones contain a carbonyl group bonded to two carbon atoms and are formed when a carbon atom within the hexane molecule undergoes oxidation, typically to form a double bond with oxygen.

Aldehydes: Similar to ketones, aldehydes may form as intermediates or byproducts during the oxidation of hexane. Aldehydes contain a carbonyl group bonded to a hydrogen atom and are typically more reactive than ketones. Examples of aldehydes that may form from hexane over-oxidation include hexanal.

Carboxylic acids: Continued oxidation of hexane can lead to the formation of carboxylic acids, such as hexanoic acid or higher molecular weight fatty acids. Carboxylic acids contain a carboxyl group (COOH) and are more oxidized than ketones or aldehydes.

Epoxides: In some cases, hexane oxidation may lead to the formation of epoxides, which are cyclic ethers containing a three-membered ring. Epoxides can be formed when an oxygen atom adds to a double bond within the hexane molecule, resulting in a cyclic ether structure.

Other oxygenated compounds: Depending on the reaction conditions and the presence of catalysts or initiators, various other oxygenated compounds may form as byproducts of hexane over-oxidation. These may include alcohols with higher molecular weights than hexanol, as well as ethers, esters, and peroxides [124].

Overall, the formation of these byproducts can occur due to excessive exposure of hexane to oxidizing agents or harsh reaction conditions. Optimizing reaction parameters such as temperature, pressure, and the concentration of oxidizing agents is crucial to minimizing the formation of unwanted byproducts and maximizing the yield of the desired hexanol product.

c) Water

Water (H₂O) plays a crucial role in various chemical processes, including the oxidation of hydrocarbons like hexane. In the context of hexane oxidation, water can serve multiple functions:

Solvent: Water is often used as a solvent or reaction medium in chemical reactions, including oxidation reactions. In the presence of water, hexane molecules can dissolve and react with oxidizing agents more effectively, facilitating the oxidation process.

Reactant: Water itself can participate in oxidation reactions under certain conditions. In the presence of certain catalysts or reactive species, water molecules can donate oxygen atoms to hydrocarbons like hexane, leading to their oxidation. This process, known as hydroxylation, can result in the formation of alcohol products, such as hexanol, from hexane.

Hydrolysis: Water can also catalyse hydrolysis reactions, where chemical bonds within hexane molecules are cleaved in the presence of water molecules. While hydrolysis may not directly lead to hexane oxidation, it can generate reactive intermediates that are susceptible to oxidation by other reagents or conditions present in the reaction mixture.

Controlling reaction conditions: The presence of water in the reaction mixture can influence reaction conditions such as temperature, pressure, and pH, which in turn can affect the rate and selectivity of hexane oxidation. Water may act as a heat sink, moderating temperature changes during exothermic oxidation reactions, and may also help maintain optimal reaction conditions for catalyst activity.

However, it is important to note that water can also potentially interfere with certain oxidation processes or promote undesired side reactions, particularly if it reacts directly with the oxidizing agent or competes with hexane for active sites on catalyst surfaces. Therefore, controlling the amount and distribution of water in the reaction system is essential for achieving desired reaction outcomes and minimizing unwanted byproducts [125].

Overall, water's multifaceted role in hexane oxidation underscores its importance as both a solvent and a reactive species, highlighting the need for careful consideration of its effects on reaction kinetics and product selectivity in the design of oxidation processes.

1.6.1.3 Reaction conditions

a) Batch reactor

Working in a batch reactor offers several advantages for the oxidation of hexane to hexanol. Firstly, batch reactors allow for precise control over reaction conditions such as temperature, pressure, and reactant concentrations, which is essential for optimizing the oxidation process and maximizing the yield of hexanol while minimizing the formation of undesired byproducts. Additionally, batch reactors offer flexibility in terms of reaction time and sequence, making it possible to vary the duration of the reaction to study its kinetics and optimize the conversion of hexane to hexanol. Moreover, different batches can be run under varying conditions to explore the effects of different parameters on the reaction outcome. Vigorous stirring implies nearly ideal or perfect mixing and as a result at a given time of reaction homogeneous concentrations and temperature in all the reaction volume. Another advantage is the ease of sampling and analysis facilitated by batch reactors. As a researcher, you can sample the reaction mixture at various time points during the reaction, allowing for real-time assessment of reaction kinetics and analysis of intermediate products. This provides valuable insights into the mechanism of hexane oxidation. Lastly, batch reactors are easily scalable for industrial production, making them suitable for process development and scale-up studies. By optimizing reaction conditions at the laboratory scale, it is possible to establish the foundation for larger-scale production of hexanol through batch oxidation of hexane. Overall, working in a batch reactor offers the flexibility, control, and scalability needed to study the oxidation of hexane to hexanol effectively, enabling systematic exploration of reaction parameters and optimization of process conditions to achieve high yields of hexanol with minimal side reactions.

b) Different temperatures

Testing different temperatures is a crucial aspect of investigating the oxidation of hexane to hexanol in a batch reactor. The impact of temperature on reaction kinetics, selectivity, and overall conversion efficiency can be explored by varying the temperature. Higher temperatures generally accelerate chemical reactions by providing more energy to overcome activation barriers, potentially leading to faster conversion rates. However, excessively high temperatures may also promote side reactions or thermal degradation of reactants or products. Conversely, lower temperatures may slow down the reaction kinetics but could enhance selectivity towards the desired product by minimizing side reactions. Through systematic experimentation at different temperature settings, it is possible to identify the optimal temperature range for maximizing hexanol yield while maintaining acceptable selectivity and minimizing undesirable byproducts. This comprehensive temperature study contributes valuable insights into the temperature dependence of the hexane oxidation reaction and informs the development of precise temperature control strategies for industrial-scale batch reactors.

c) Different pressures

Using pressure control in the investigation of hexane oxidation to hexanol in a batch reactor is a critical parameter to consider. The manipulation of pressure levels primarily influences the solubility of gases within the reaction mixture, crucial for maintaining reactants in the liquid phase. By systematically exploring various pressure conditions, it is possible to pinpoint the optimal pressure range for achieving high yields of hexanol with desired selectivity while minimizing energy consumption. This thorough examination of pressure dependencies provides valuable insights into the intricacies of hexane oxidation and aids in the design of pressure-controlled batch reactors for large-scale industrial production processes. It is important to notice that pressure will be held high enough to keep all the chemicals in liquid phase.

1.6.1.4 Metal-organic frameworks

MIL-100, HKUST-1 and MOF-808 @His-Cu will be the used MOFs. These will not further be discussed as they already extensively were earlier.

1.6.2 P&ID

The P&ID of the installation that is used for the research methodology can be found in **Figure 6**. The reaction occurs within a stirred reactor setup. This reactor is capable of being pressurized by opening 'Valve 2', which connects to a gas tank supplying pressure of up to 300 bar. The gas within the tank is helium (He), chosen for its inert properties. Pressure indicators 'P4' and 'P3' monitor the pressure within the gas tank and the line connecting it to 'Valve 2', respectively. Additionally, 'P2' measures the pressure between the stirred reactor and 'Valve 2', reflecting the pressure within the reactor when both valves are closed during the reaction. It has a measurement range of up to 100 bar, suitable for the working pressure range. 'P1' measures lower pressures within the tank, up to 15 bar, compensating for 'P2's less precise measurements at lower pressures. In addition to pressure monitoring, the liquid temperature within the reactor is measured by 'T1', while the reactor is heated using a heating mantle. Stirring of the reactor is achieved via a stirrer powered by a motor. To release pressure from the reactor, 'Valve 1' can be opened.

It is in this setup that the different aspects of the research methodology, as mentioned in the beginning **1.1.2.1**, will be researched.

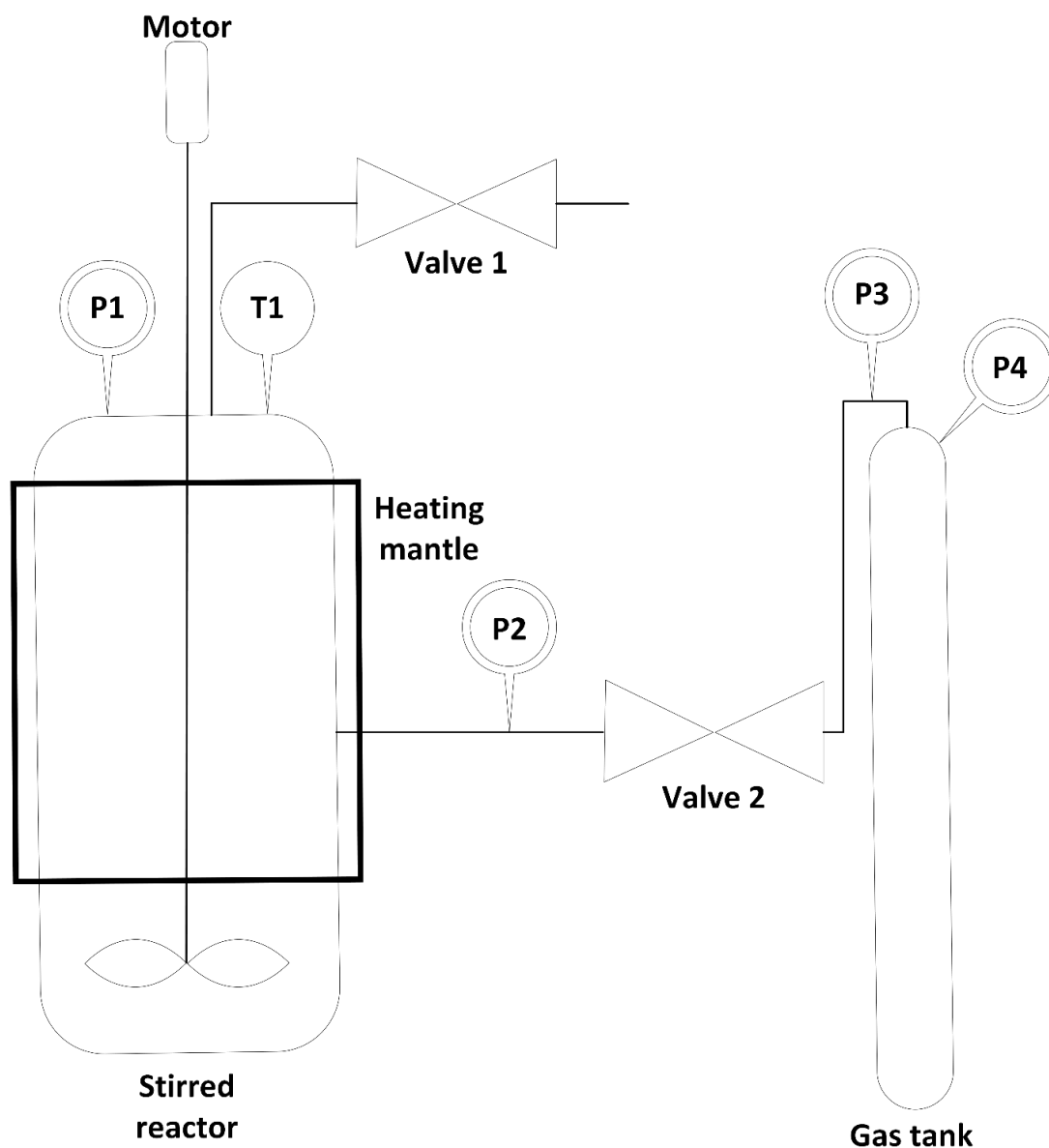


Figure 6: P&ID research methodology

2 Materials and methods

2.1 Materials

Hexane (95%) [126] and H₂O₂ (35%) [127] were utilized in the experimental procedures. The synthesis of MIL-100 involved trimesic acid (95%) [128], NaOH ($\geq 98,0\%$) [129], FeCl₂·4H₂O (98%) [130], and ethanol (96%) [131]. For the preparation of HKUST-1, trimesic acid (95%) [128], NaHCO₃ (99,0-100,5%) [132], Cu(NO₃)₂·5H₂O (98%) [133] and ethanol (96%) [131] were employed. The synthesis of MOF-808 @His-Cu required acetic acid (99,8%) [134], ZrCl₄ ($\geq 99,5\%$) [135], histidine ($\geq 99\%$) [136], methanol ($\geq 99,8\%$) [137], Cu(CO₂CH₃)₂·H₂O ($\geq 98\%$) [138], and acetonitrile ($\geq 99,9\%$) [139].

2.2 Experimental setup

The experimental setup involved conducting experiments using two different methods. The first method, as shown in **Figure 7** [140], commenced with measuring both the volume of hexane and hydrogen peroxide (35%). Following this, a specific mass of MOF was weighed out. Initially, volumes of 35% hydrogen peroxide (blue) and hexane (purple) were decanted into the reactor. Subsequently, the metal organic frameworks were added. The reactor was then immediately sealed, and the stirrer was activated. Depending on the chosen parameters, the reactor was also heated and/or pressurized. After the specified reaction time, the reactor was brought back to standard conditions, namely room temperature and atmospheric pressure. The resulting liquid was transferred to a graduated cylinder, and samples were taken from each phase (polar and non-polar) using a micropipette. These samples were then analysed using a gas chromatograph (GC).

The second method followed a similar procedure. Here, a volume of 35% hydrogen peroxide and hexane, along with a certain mass of MOF, were combined in a vial. Unlike the reactor, which has a total volume of 100 mL, the vial has a total volume of 30 mL. Stirring was accomplished using a magnetic stirrer, and heating was achieved via a water bath, as opposed to the reactor, which was stirred with a stirrer and heated with a heating mantle. However, the vial cannot be pressurized. The advantage of this setup lies in its ability to conduct multiple experiments in parallel. Furthermore, the process unfolds in a manner analogous to that of the reactor. As with the first method, the resulting liquid was transferred to a graduated cylinder, and samples were taken for analysis by a GC.

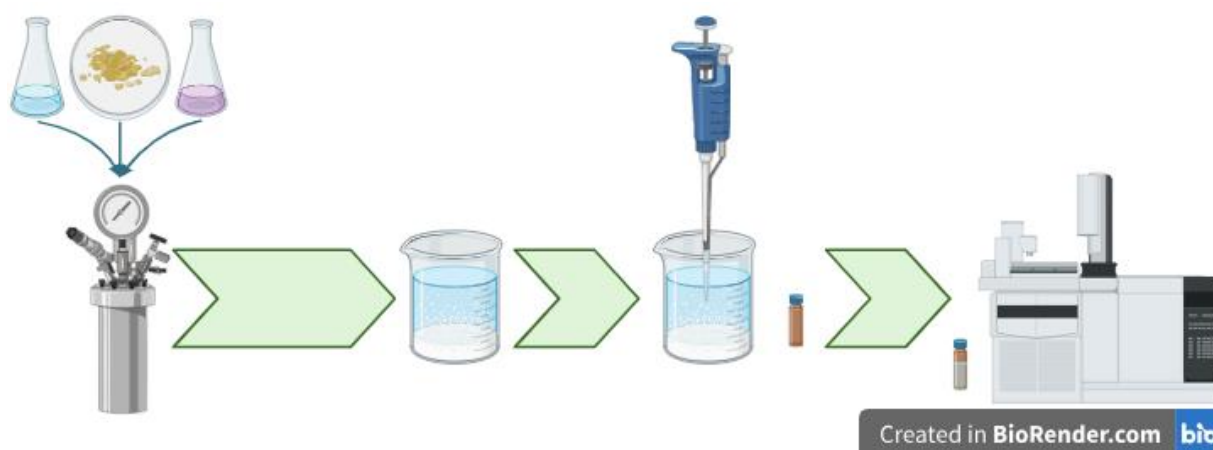


Figure 7: Experimental setup

2.3 MOF synthesis

2.3.1 MIL-100

To initiate the synthesis, 3,06 g of benzene-1,3,5-tricarboxylic acid (trimesic acid) was dissolved in 42,81g of 1M aqueous NaOH at room temperature, with stirring for 5-10 minutes until complete dissolution occurred. Meanwhile, 4,08 g of FeCl₂·4H₂O was dissolved in 175,59 mL of Milli-Q[®] water, also known as Type 1 water, at room temperature, ensuring thorough mixing. Subsequently, the first

solution from was added dropwise and slowly into the second solution while continuously stirring. The resulting mixture was allowed to stir for 24 hours at room temperature. Afterward, the brown precipitate formed was collected through centrifugation at 3500 rpm for 5 minutes. To eliminate any unreacted reagents, the solid was redissolved in a small amount of Milli-Q[®] water with stirring and subjected to another centrifugation step. This washing process was repeated three times with Milli-Q[®] water and three times with ethanol to ensure thorough purification. Finally, the solid product was dried at 100°C for 24 hours to obtain the desired material. The structure of MIL-100 is presented as **Figure 8** [141], where the blue octahedra are the iron clusters connected by the organic H₃BTC ligands. Hydrogen atoms are omitted for clarity purposes.

2.3.2 HKUST-1

HKUST-1 was prepared following the method outlined by Loera-Serna et al. [142]. In this procedure, 2,38 mmol of trimesic acid (H₂BTC) and 7,14 mmol of NaHCO₃ (in a 1:3 ratio) were dissolved in 150 mL of deionized water. Subsequently, a solution containing 3,57 mmol of copper nitrate pentahydrate (in a molar 3:2 Cu(NO₃)₂/H₂BTC ratio) and 40 mL of ethanol was slowly added dropwise to the mixture. The reaction mixture was then stirred at room temperature for 12 hours. After completion, the resulting HKUST-1 product was isolated via centrifugation and subsequently dried at 323 K for 2 hours. The structure of HKUST-1 is presented as **Figure 9** [143], where the framework structure of HKUST-1 displays two different types of pores represented by spheres within the structure. Metal atoms are depicted in blue, oxygen atoms in red, and carbon atoms in black. Hydrogen atoms are omitted for clarity purposes.

2.3.3 MOF-808 @His-Cu

First, a mixture of 20 mL of Milli-Q[®] water and 20 mL of acetic acid was prepared and stirred. Then, 1,86 g of ZrCl₄ and 0,56 g of trimesic acid were added to the solution. The stirring continued for 24 hours at 105°C. The resulting mixture was washed every 6 hours with 25 mL of Milli-Q[®] water three times and once with methanol. Subsequently, the material was dried at 80°C for 24 hours. For functionalization, 150 mg of MOF-808 was added to a solution containing 100 mL of 0,05 M histidine, and the mixture was stirred for 24 hours at room temperature. Similar to the previous step, the material was washed every 6 hours with 25 mL of Milli-Q[®] water three times and once with methanol before being dried at room temperature. Lastly, for metal doping, A solution of Cu(CO₂CH₃)₂H₂O (4,86 g) in acetonitrile (ACN, 60 mL) was added to a suspension of MOF-808 @His (600 mg) in ACN (15,2 mL) in a vial while stirring under ambient conditions. The vial was sealed and the mixture was stirred for 3 days at room temperature. The powder was collected by centrifugation (3 000 rpm, 5 min) and washed with ACN 6 times over 2 days. Finally, MOF-808 @His-Cu was dried at room temperature. This synthesis procedure is based on the method proposed by Baek et al. [71]. The structure of MOF-808 @His-Cu is presented as **Figure 10** [71], where carbon atoms are depicted in black, oxygen in red, nitrogen in green, copper in orange, and zirconium as blue polyhedra. Hydrogen atoms are omitted for clarity purposes.

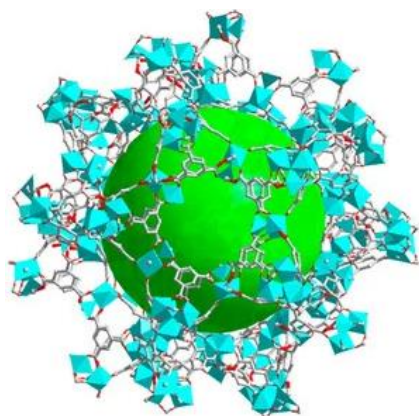


Figure 8: MIL-100

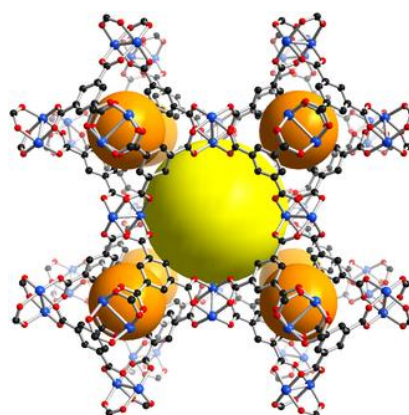


Figure 9: HKUST-1

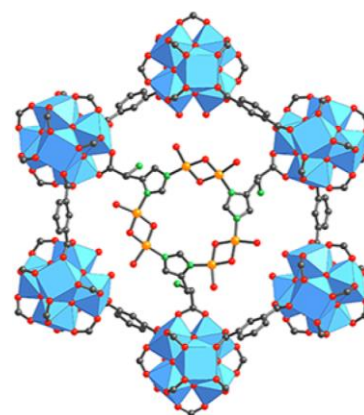


Figure 10: MOF-808 @His-Cu

2.4 MOF characterisation techniques

2.4.1 Nitrogen adsorption analysis

Nitrogen adsorption is a widely used technique for characterizing metal-organic frameworks (MOFs) due to its effectiveness in determining specific surface area and pore volume, which are critical parameters for evaluating the performance of MOFs in various applications such as gas storage, separation, and catalysis.

One of the primary advantages of nitrogen adsorption is its ability to provide detailed information about the surface area of MOFs. By measuring the amount of nitrogen gas adsorbed onto the surface of the MOF at different pressures, it is possible to construct an adsorption isotherm. Using models such as the Brunauer-Emmett-Teller (BET) theory, it is possible to calculate the specific surface area of the material. This measurement is essential for understanding the capacity of MOFs to adsorb gases or catalyse reactions, as a higher surface area generally indicates more active sites available for interaction.

In addition to surface area, nitrogen adsorption can also be used to determine the pore volume and pore size distribution of MOFs. The technique involves analysing the volume of nitrogen adsorbed at various relative pressures to identify the point at which the pores are filled. This information is crucial for applications where the size and volume of pores can significantly impact performance, such as in gas storage, where larger pore volumes can enhance storage capacity, or in catalysis, where specific pore sizes can facilitate the selective interaction of reactants.

Nitrogen adsorption is particularly suitable for MOFs due to its ability to probe both micropores (pores less than 2 nm in diameter) and mesopores (pores between 2 and 50 nm in diameter). MOFs often possess a hierarchical pore structure, and nitrogen adsorption can provide a comprehensive understanding of this structure, which is vital for tailoring MOFs to specific applications.

Overall, nitrogen adsorption is a robust and informative technique for characterizing MOFs, providing essential insights into their surface area, pore volume, and pore size distribution. These parameters are critical for optimizing the design and application of MOFs in various fields, making nitrogen adsorption an indispensable tool in MOF research.

2.4.1.1 Principle of nitrogen adsorption analysis

a) Isotherms

To draw conclusions from adsorption-desorption isotherms and hysteresis loops, a systematic approach involving the comparison of experimental isotherms with standard types defined by the International Union of Pure and Applied Chemistry (IUPAC) will be employed. The images of isotherm types and hysteresis loop types serve as critical reference tools in this process. The first step involves matching the experimental isotherm to one of the six standard types (Type I to Type VI), as shown in **Figure 11** [144]. Each type is indicative of different adsorption characteristics and pore structures:

- Type I: Isotherm indicates microporous materials with high adsorption at low relative pressures.
- Type II: Isotherm is characteristic of non-porous or macroporous materials, showing monolayer-multilayer adsorption.
- Type III: Isotherm suggests weak adsorbent-adsorbate interactions.
- Type IV: Isotherm is typical for mesoporous materials, with a hysteresis loop indicating capillary condensation.
- Type V: Isotherm is similar to Type III but with a hysteresis loop, indicating mesoporosity with weak interactions.
- Type VI: Isotherm shows stepwise multilayer adsorption on a uniform surface.

By visually comparing the experimental data to these standard types, initial insights into the material's porosity and surface characteristics can be drawn. When a hysteresis loop is present in the isotherm, its shape and type provide additional information about the pore structure [145].

The types of hysteresis loops (H1, H2, H3, and H4), as shown in **Figure 12** [146], are:

- H1: Hysteresis indicates well-defined cylindrical pores.
- H2: Hysteresis suggests a complex pore structure, possibly ink-bottle pores with narrow necks and wide bodies.
- H3: Hysteresis is associated with slit-like pores or plate-like particles.
- H4: Hysteresis is often linked to narrow slit-like pores or microporous materials.

Matching the hysteresis loop from the experimental isotherm to these types helps refine the understanding of pore shapes and connectivity within the material. By combining the information obtained from isotherm type and hysteresis loop analysis, a comprehensive profile of the material's porosity can be constructed. For instance, a Type IV isotherm with an H1 hysteresis loop would indicate a mesoporous material with cylindrical pores. This combined approach allows for the systematic classification and interpretation of experimental adsorption-desorption data, facilitating a detailed understanding of material properties and guiding the selection and optimization of materials for various scientific and industrial applications [147].

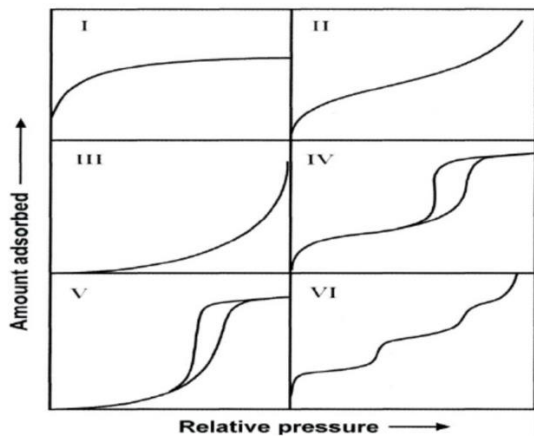


Figure 11: IUPAC classification of adsorption isotherms

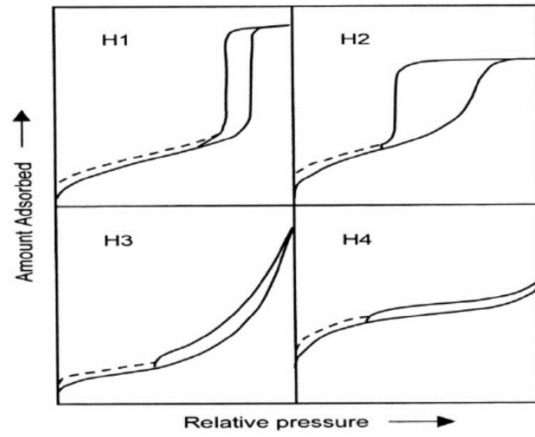


Figure 12: IUPAC Classification of Hysteresis Loops

b) Specific surface area

Calculating the surface area of a material using nitrogen adsorption and the BET (Brunauer-Emmett-Teller) theory [148] involves several steps. First, nitrogen adsorption measurements are performed to obtain the adsorption isotherm, which plots the volume of nitrogen adsorbed against the relative pressure at the temperature of saturated liquid nitrogen (77 K). Then the linear region of the BET plot is identified, typically corresponding to relative pressures between 0.05 and 0.35, though this range can vary depending on the material [149].

Next, the BET equation [148] is applied:

$$\frac{P}{V(P_0 - P)} = \frac{1}{V_m C} + \frac{C - 1}{V_m C} \times \frac{P}{P_0}$$

Where P is the equilibrium pressure of nitrogen, P₀ is the saturation pressure of nitrogen, V is the volume of nitrogen adsorbed at pressure P, V_m is the volume of nitrogen adsorbed at monolayer coverage, and C is the BET constant related to the energy of adsorption.

Then $\frac{P}{V(P_0 - P)}$ is plotted against $\frac{P}{P_0}$ to yield a straight line in the BET region. After this, the slope S and intercept I are determined by performing linear regression on the BET plot. The monolayer volume V_m is calculated using the slope and intercept with the formula $V_m = \frac{1}{S+I}$, and the BET constant C using $C = 1 + \frac{S}{I}$.

To calculate the surface area, the molar volume of nitrogen at standard temperature and pressure (STP), which is 22,414 L/mol, is used. The surface area per gram of adsorbent S_{BET} is given by

$$S_{BET} = \frac{V_m \times N_A \times \sigma}{V_m \times m}$$

Where N_A is Avogadro's number ($6,022 \times 10^{23}$ molecules/mol), σ is the cross-sectional area of a nitrogen molecule (typically $0,162 \text{ nm}^2$), and m is the mass of the adsorbent (in grams) [150].

c) Pore volume and size distribution

Calculating pore volume and pore size distribution using nitrogen adsorption involves several key steps. The process involves measuring the amount of nitrogen gas adsorbed by the material at various relative pressures [149].

Before conducting the adsorption measurements, the sample must be properly prepared by degassing to remove any adsorbed moisture or contaminants, typically by heating the sample under vacuum or an inert gas flow. For this master thesis the first option was chosen. In the adsorption experiment, the sample is cooled to liquid nitrogen temperature (77 K), and the adsorption measurements are taken by incrementally increasing the relative pressure (P/P_0), and measuring the amount of nitrogen adsorbed at each step. This is followed by desorption measurements where the relative pressure is gradually decreased, and the amount of nitrogen desorbed is measured to obtain a desorption isotherm.

The adsorption isotherm, which is a plot of the amount of nitrogen adsorbed (V_{ads}) versus the relative pressure (P/P_0), provides essential information about the surface properties and porosity of the sample. The total pore volume can be estimated from the nitrogen adsorption isotherm using the single-point method, where at a relative pressure close to 1 (usually around 0,99), the volume of adsorbed nitrogen corresponds to the total pore volume. This is because, at high relative pressures, the pores are filled with condensed nitrogen. The volume of adsorbed nitrogen is then converted to the volume of liquid nitrogen using the molar volume of liquid nitrogen ($34,7 \text{ cm}^3/\text{mol}$).

To determine the pore size distribution, the Barrett-Joyner-Halenda (BJH) method [151] is commonly used, and so also in this master thesis. This involves calculating the cumulative pore volume as a function of pore radius using the adsorption isotherm data and applying the Kelvin equation to relate the relative pressure to the pore size. The Kelvin equation [152] is given by

$$\ln\left(\frac{P}{P_0}\right) = -\frac{2 \times \gamma \times V_m}{r \times R \times T}$$

where γ is the surface tension of liquid nitrogen, V_m is the molar volume of liquid nitrogen, r is the pore radius, R is the gas constant, and T is the temperature (in Kelvin). The incremental pore volume is calculated for each pore size interval, and the pore volume distribution is plotted as a function of pore size to obtain the pore size distribution curve.

To specifically determine micropores, the t-plot method is employed. The t-plot method is based on the concept of statistical thickness (t) of the adsorbed layer. It involves plotting the volume of gas adsorbed versus the thickness of the adsorbed film to identify different types of pores in the material. The statistical thickness is calculated using reference data obtained from non-porous standard materials, commonly using the Harkins-Jura equation [153], [154]:

$$t = \left(\frac{0,13}{0,034 - \log(P/P_0)} \right)^{1/2}$$

Where t is the thickness of the adsorbed layer and P/P_0 is the relative pressure.

From the linear portion of the t-plot (mesopore region), the micropore volume can be determined from the intercept of the linear region with the y-axis (volume adsorbed), while the external surface area can be obtained from the slope of the linear region. The t-plot method is valuable for distinguishing between micropores and mesopores and for determining the specific surface area and micropore volume, complementing the information obtained from the BJH method.

2.4.2 X-ray diffraction (XRD)

Incorporating X-ray Diffraction (XRD) analysis for the characterization of Metal-Organic Frameworks (MOFs) offers numerous advantages and insights into the structural properties of these materials. XRD is integral to MOF characterization, enabling phase identification and structural analysis without additional labelling. By comparing diffraction patterns with databases, it is possible to confirm MOF crystalline structure and purity, providing insights into its performance. Additionally, XRD offers detailed information on MOF crystal structure, including unit cell dimensions and atomic arrangement. Analysis of diffraction peaks extracts structural parameters, enhancing understanding of MOF structure-property relationships. Moreover, XRD facilitates the study of phase transformations and structural changes in MOFs under varying conditions like temperature or guest molecule adsorption. Monitoring diffraction pattern changes yields critical insights for MOF design and optimization. Furthermore, XRD serves as a quality control tool for assessing MOF crystallinity and purity, aiding in method optimization. Quantitative analysis techniques like Rietveld refinement enable phase composition determination and defect assessment within the MOF lattice. Overall, the use of XRD provides valuable structural and phase information about MOFs, facilitating their characterization.

2.4.2.1 Principle of XRD

X-ray diffraction relies on the interaction between X-rays and matter, particularly the periodic arrangement of atoms within a substance. X-rays, which have wavelengths comparable to the size of atoms, are diffracted by the atomic planes within crystalline materials. This diffraction phenomenon produces a characteristic diffraction pattern, consisting of diffracted beams with specific directions and intensities, which can be used to deduce valuable information about the material's crystal structure, phase, orientation, and internal stress.

The principle of X-ray diffraction is based on the concept of wave diffraction, which occurs when a wave encounters a periodic structure. In the case of X-rays, the periodic arrangement of atoms in a crystalline material acts as an effective diffraction grating, splitting the incident X-ray beam into several diffracted beams traveling in different directions. The resulting diffraction pattern reflects the internal arrangement of atoms within the material, providing insights into its crystallographic properties.

X-ray diffraction is widely used in materials science and various fields of research and technology. It is employed for phase identification, orientation determination, lattice parameter measurement, assessment of crystal quality, and determination of crystal structure. Additionally, X-ray diffraction is indispensable for the non-destructive characterization of thin films, providing information such as phase, lattice parameter, film thickness, orientation relation with the substrate, and internal stress and strain [155].

2.4.2.2 Application of Bragg's law

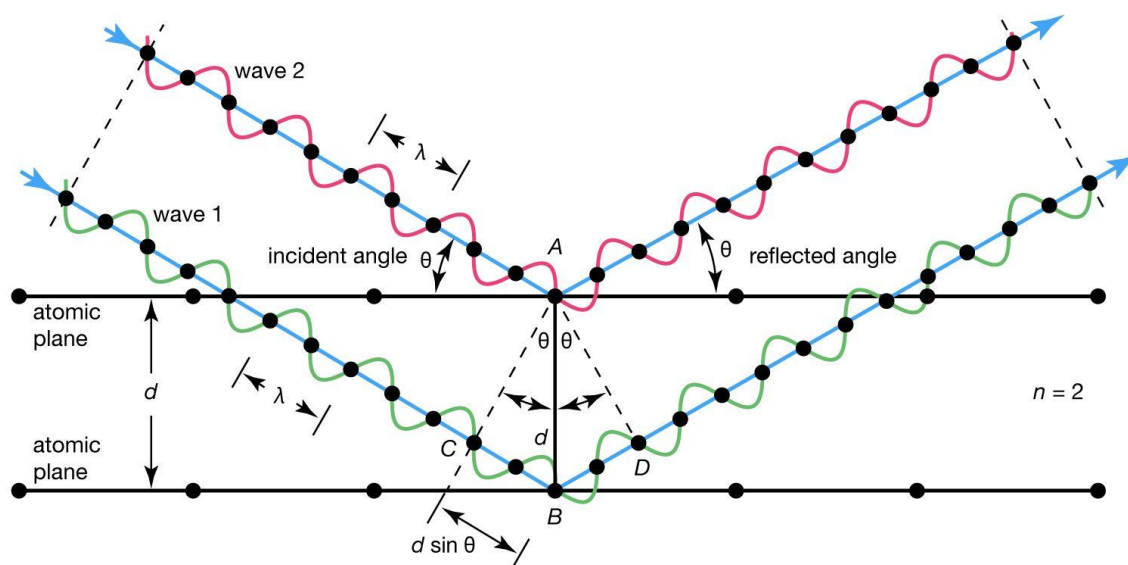
Bragg's law is one of the most important aspects of XRD. The equation is:

$$n \lambda = 2d \sin (\theta)$$

Where n is the diffraction order, λ is the wavelength in nm, d is the inner spacing, and theta (θ) is the angles of the diffractions. This equation is used to create a graph that plots the angles to find intensity [156].

As visible in **Figure 13** [157] Bragg diffraction occurs when waves 1 and 2, maintaining phase alignment, encounter atoms A and B of a crystal separated by a distance d between lattice planes. Experimentally, the angle of reflection θ equals the incident angle θ . For constructive interference, the path length CBD must equal an integer multiple (n) of wavelengths (λ), or $n\lambda$. Geometrically, CB and BD are equal and equivalent to d times the sine of θ , or $d \sin \theta$. Therefore, $n\lambda = 2d \sin \theta$, known as the Bragg law. In the diagram, when $n = 2$, there is one wavelength along CB , and the reflected angle is smaller compared to higher n values. Reflection angles corresponding to different n values are termed orders of reflection. Reflections corresponding to fractional n values result in destructive interference

[157].



© Encyclopædia Britannica, Inc.

Figure 13: Bragg's law for X-ray diffraction

2.4.3 Field emission scanning electron microscopy (FE-SEM)

FE-SEM offers high-resolution imaging for visualizing MOF surface morphology, texture, and nanostructure at nanometre-scale resolution, aiding in particle size, shape, pore structure, and surface roughness analysis. Surface topography analysis reveals features like pores, channels, defects, and crystalline domains, crucial for understanding adsorption capacity, catalytic activity, and structural stability. Moreover, FE-SEM facilitates particle size distribution analysis, assessing uniformity and identifying size-related irregularities affecting material performance. Overall, FE-SEM is a versatile tool for morphological, structural, and chemical characterization of MOFs, aiding in understanding microstructure, surface properties, and functional behaviour, essential for optimization its applications.

2.4.3.1 Principle of FE-SEM

FESEM typically adheres to the same principles as traditional SEM, with the primary distinction lying in the electron generation mechanism. Unlike SEM, which utilizes thermionic emission, FESEM employs a Field Emission Gun (FEG) to generate electrons. In FEGs, an electric field gradient is applied to emit the electron beam, enhancing the instrument's performance compared to conventional SEM setups [158]. In **Figure 14** [159] the typical build up of a SEM is shown where the type of electron source is not specified. In the case of FE-SEM the electron source is a FEG.

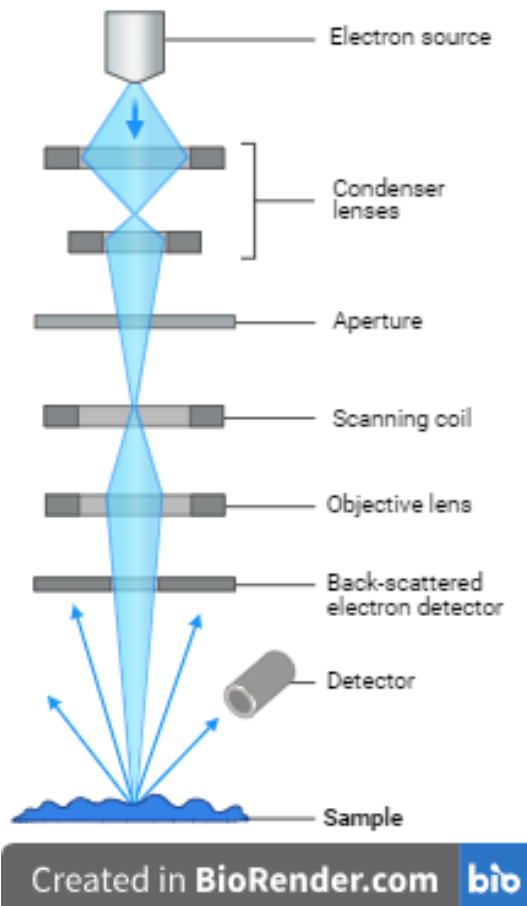


Figure 14: Scanning electron microscope

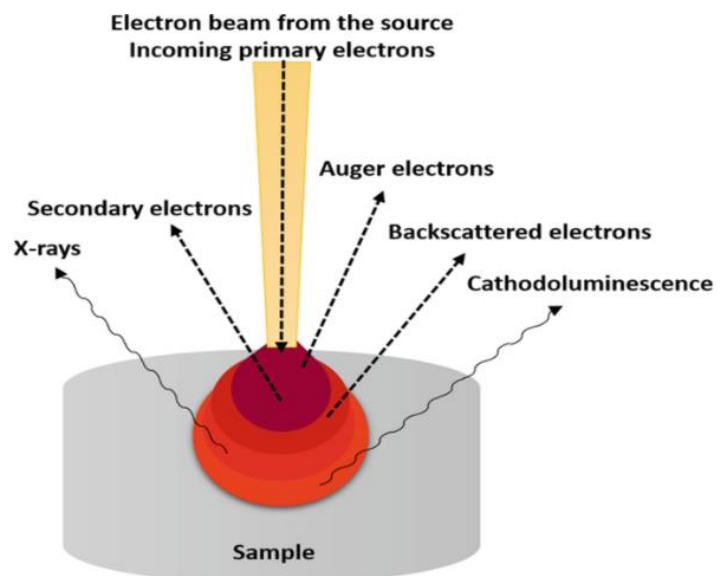


Figure 15: Interaction of specimen with electron beam

Scanning Electron Microscopy (SEM) requires specific sample preparation techniques for optimal imaging. Typically, a sample holder with a stub is employed to secure the sample on the surface. Carbon tape is commonly used to affix the sample to the stub. Initially, two-sided carbon tape is applied to the stub, followed by the addition of a thin layer or small amount of material. This thin layer adheres well to the carbon tape, minimizing charging issues and ensuring clear imaging. After sample preparation, the sample-covered stub is placed in the sample holder within the SEM chamber. Unlike Transmission Electron Microscopy (TEM), which requires thin samples, SEM can examine relatively thick specimens.

The fundamental principle of SEM, as shown in **Figure 15** [160], involves the release of primary electrons from a source, which then interact with the specimen's atomic electrons. These interactions result in the emission of secondary electrons (SEs), forming an image by collecting these SEs from each point of the specimen. SEM operates under vacuum conditions to achieve high resolution and avoid electron interactions with gas molecules.

Primary electrons emitted from the electron gun are accelerated by applying high energy, typically in the range of 1–40 keV. These electrons are focused into a monochromatic beam by magnetic field lenses and metal slits within a vacuumed column. The focused electron beam scans across the sample surface in a raster pattern. When the primary electron beam strikes the sample surface, it interacts with the near-surface area, generating various signals due to interactions with the specimen's nucleus and electrons. These signals include secondary electrons (SEs), backscattered electrons (BSEs), photons (X-rays used for elemental analysis), and visible light (cathodoluminescence – CL). Different detectors collect these signals, which are then processed by a computer to form the required image. The two primary electrons used for image creation are secondary electrons (indicating sample morphology and topography) and backscattered electrons (demonstrating contrasts in sample composition).

Moreover, X-rays are generated when incident electrons collide with the electrons in the orbitals of sample atoms, producing characteristic X-rays for each element present. SEM is non-destructive, allowing repeated analysis of the same material. In SEM, interactions between electrons and the specimen occur through inelastic and elastic interactions. Inelastic interactions involve the transfer of energy from the primary electron beam to the specimen atom's electron, resulting in the emission of secondary electrons. Elastic interactions cause the direction of primary electrons to change without significant energy loss, resulting in backscattered electrons.

Overall, SEM offers valuable insights into sample morphology, composition, and elemental analysis, making it a powerful tool in materials science and engineering research [160].

2.4.4 Thermogravimetric analysis (TGA)

TGA is used to assess MOF thermal stability. It identifies temperature ranges associated with framework decomposition, ligand degradation, or guest molecule desorption, offering insights into material suitability. Additionally, TGA can provide information on MOF-guest molecule interactions by monitoring weight changes during heating, helping distinguish decomposition processes and detect thermal events related to guest molecule behaviour. Quantitative analysis of framework stability can be performed using TGA data, allowing for comparisons between different MOF formulations and evaluations of synthetic parameters. TGA also detects defects, disorder, or impurities in MOF samples, aiding in quality control and process optimization by optimizing synthesis conditions or post-synthetic treatments. Coupled with EGA techniques like mass spectrometry or FTIR, TGA can elucidate degradation mechanisms and thermal decomposition pathways, informing materials design and stability enhancement strategies. Overall, TGA is a powerful technique for characterizing the thermal properties and stability of MOFs, providing essential information for materials design, process optimization, and application development in areas such as gas storage, catalysis, sensing, and drug delivery.

2.4.4.1 Principles of TGA

The International Confederation for Thermal Analysis and Calorimetry (ICTAC) defines thermal analysis (TA) as a set of techniques that observe changes in the physical or chemical properties of a sample over time as it undergoes a programmed temperature regimen. Thermogravimetric analysers (TGA) monitor and record sample mass, time, and temperature, with temperature programs typically including heating, cooling, isothermal holds, or a combination thereof [161]. The analyser comprises a precise microbalance connected to a sample pan housed within a furnace equipped with a temperature programmer and controller, known as a thermo-balance [162]. Sample loading into the TGA can be performed from the bottom (hang-down), top, or side, with a thermocouple near the pan monitoring the sample temperature, as shown in **Figure 16**, **Figure 17** and **Figure 18** [163]. A protective tube isolates the heating elements and cooling coils from the sample pan, while a dynamic purge gas flows over the sample at a rate of 20-200 mL/min [163].

Various configurations of TGAs exist, including bottom-loading, top-loading, and side-loading designs, each with specific sample pan support mechanisms and gas flow arrangements. The furnace, sample holder, gas entry, and exit points are strategically configured to minimize turbulence near the sample pan and prevent noise in the mass flow signal. Counter pans are employed to counteract the weight of the sample pan and support rods, ensuring that sample mass changes remain within the dynamic range of the balance. Symmetrical TGAs utilize electromagnetic-optical balances with counter pans housed in their own furnace chambers to counteract buoyancy effects and maintain balanced gas flow on both samples [163]. TGAs operate under different gas atmospheres, such as oxidizing, inert, or reducing environments, depending on the desired analysis [164], [165].

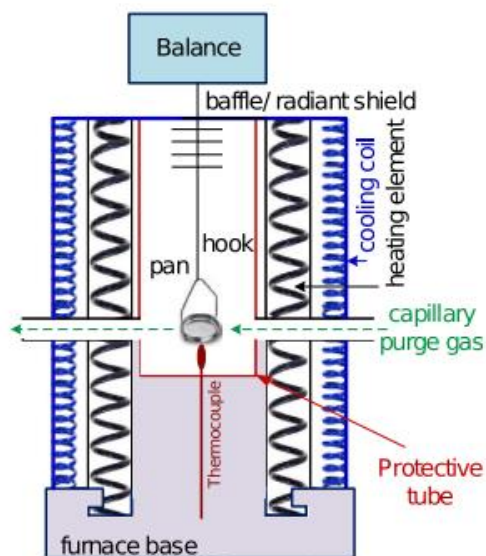


Figure 16: Bottom loading or hang-down

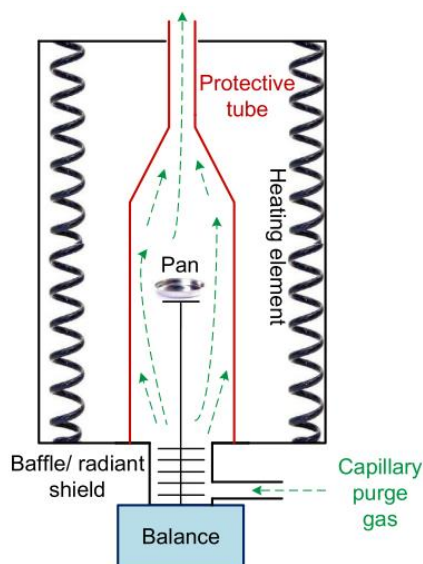


Figure 17: Top loading

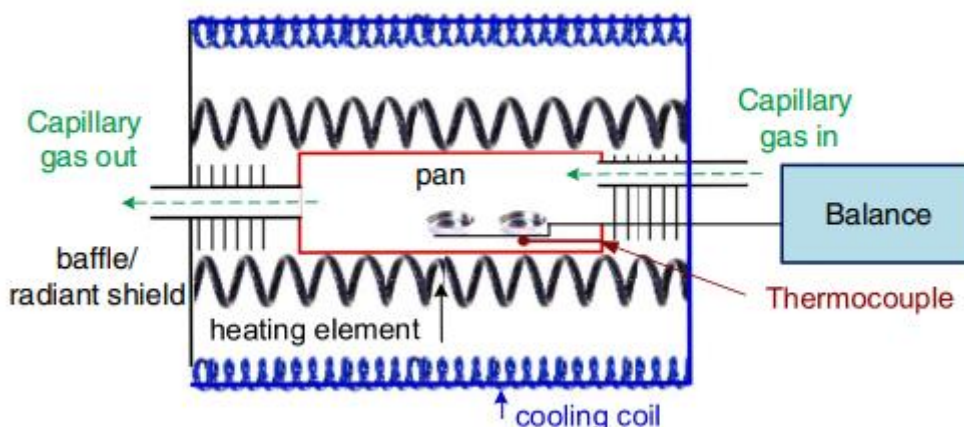


Figure 18: Side loading

2.5 Sample analysis and calibration measurements

For the identification of the compounds that were found in the samples the GC-MS (2.5.2.2) was used. Once each compound and its retention time were determined the use of a GC (2.5.2.1) appeared to be faster and more practical, while still providing the necessary precision. The calibration measurements were all measured with the GC (2.5.2.1) since identification of the components was not required.

2.5.1 Gas chromatography

Gas chromatography (GC) is a powerful analytical technique used for separating and analysing volatile compounds present in complex mixtures. The fundamental principle behind GC involves the separation of analyte molecules based on their differential partitioning between a stationary phase and a mobile phase within a chromatographic column. The various components of a GC are shown in **Figure 19** [166].

In a typical GC setup, the sample containing the analyte mixture is introduced into the system through an injection port, where it is vaporized and carried by an inert gas, known as the carrier gas, into the chromatographic column. The chromatographic column is typically packed with a stationary phase, such as a thin film coated on the inner wall of a capillary column or a packed bed of solid particles. The choice of stationary phase depends on the properties of the analytes being separated.

As the sample components travel through the column, they interact with the stationary phase to varying degrees. Components that have a stronger affinity for the stationary phase will spend more time interacting with it and consequently elute from the column later, while those with weaker affinity will elute earlier. This differential partitioning leads to the separation of the analyte mixture into individual components as they exit the column. Additionally, adjusting the column temperature can be employed to either enhance component separation at lower temperatures or shorten the analysis time at higher temperatures, providing further control over the chromatographic process.

The separated components are then detected by a detector, such as a Flame Ionization Detector (FID), a Thermal Conductivity Detector (TCD), or a Mass Spectrometer (MS), based on their unique physical or chemical properties. The detector generates a signal proportional to the concentration of each component, which is recorded and plotted as a chromatogram.

When coupled with a mass spectrometer (GC-MS), see **Figure 20** [167], [168], gas chromatography enables not only separation but also identification of individual compounds within complex mixtures. In GC-MS, the effluent from the chromatographic column is introduced directly into the mass spectrometer, where the separated analytes are ionized and fragmented into characteristic mass spectra. These spectra are then compared to a reference database to identify the compounds present in the sample.

Overall, gas chromatography is a versatile and widely used technique in analytical chemistry, offering high sensitivity, resolution, and selectivity for the separation and analysis of a wide range of volatile compounds. Its combination with mass spectrometry further enhances its capabilities for compound identification and structural elucidation.

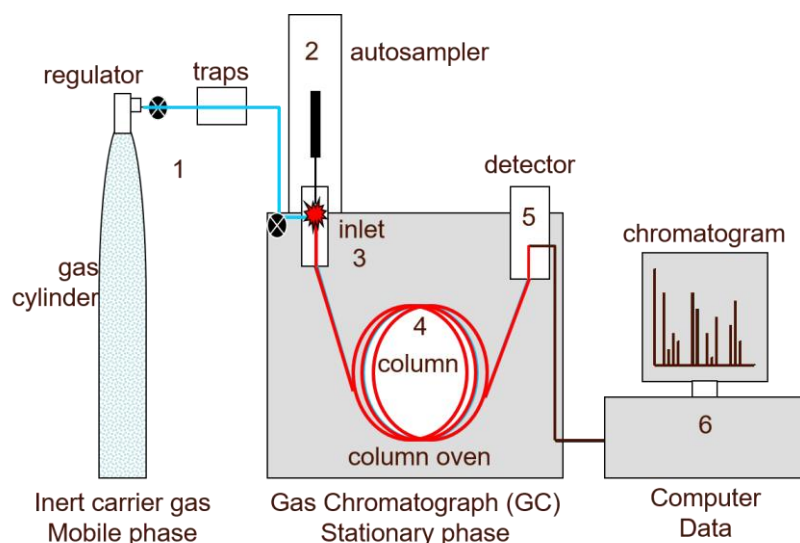


Figure 19: GC

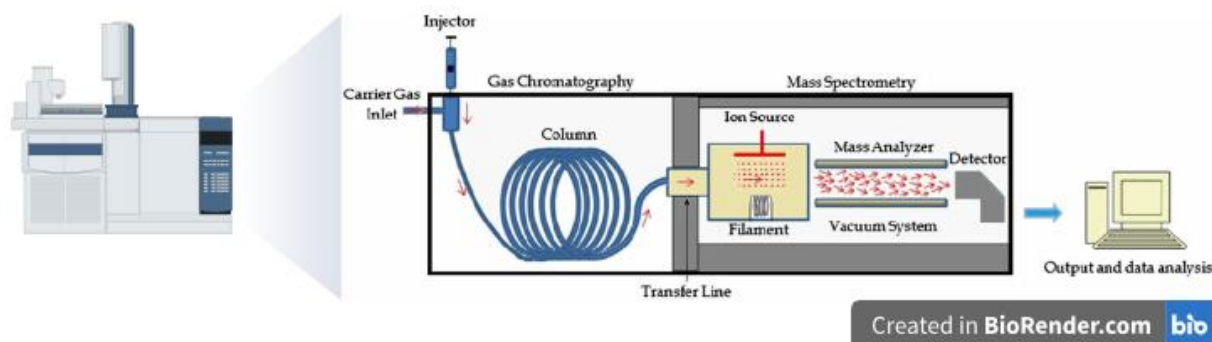


Figure 20: GC-MS

2.5.2 Used chromatographs

2.5.2.1 GC

The utilization of the 'HP 6890 GC system' equipped with a Flame Ionization Detector (FID) and a Thermal Conductivity Detector (TCD), along with the 7683B series injector, presents a robust and versatile analytical technique for sample analysis and calibration curve generation. The GC system offers high sensitivity and selectivity, allowing for the accurate quantification and identification of analytes present in complex mixtures. The FID detector excels in detecting organic compounds, providing excellent sensitivity and a wide dynamic range, while the TCD detector offers enhanced sensitivity to non-organic compounds, expanding the scope of analyte detection. Additionally, the 7683B series injector ensures precise and reproducible sample introduction, minimizing variability in injection volumes and enhancing measurement accuracy. Overall, the integration of these components within the GC system enables comprehensive and reliable analysis, making it an ideal choice for analytical tasks requiring high performance and versatility [169], [170].

a) Method specifications

The gas chromatography analysis was conducted using a series of specific instrument settings. The analysis involved a stepwise process beginning with the oven, which was initially set to a temperature of 40°C and held for 5 minutes before ramping up to 150°C at a rate of 10°C per minute. The final post-run temperature was set to 220°C and held for an additional 2 minutes.

For the injection process, a front injector was utilized with an injection volume of 0,2 µL, using a syringe size of 10,0 µL. The EPC Split-Splitless Inlet was employed in Split mode, with helium gas as the carrier at a split ratio of 10:1 and a split flow rate of 148 mL/min. The inlet was heated to 275°C, with a total flow rate of 166 mL/min, including a gas saver function set at 20 mL/min for a duration of 2,00 minutes.

The column operated under constant pressure mode, with helium flow maintained at 9,08 psi, corresponding to a flow rate of 14,8 mL/min and a velocity of 89 cm/sec. A specific column model, the DB-WAX Ultra Inert Column from Agilent, with dimensions of 30,0 m length, 1,00 µm thickness, and 0,53 mm diameter, was utilized [171].

Detection was performed using two detectors: the front detector (FID) and the back detector (TCD). The FID operated with a heater temperature of 300°C, hydrogen flow of 40,0 mL/min, air flow of 450 mL/min, and a makeup flow of nitrogen (N₂) at 23,0 mL/min. The flame was turned off during analysis, with a lit offset set to 2,0 and a data rate configured for a minimum peak width of 5 Hz over a duration of 0,04 minutes.

The TCD detector was set to a heater temperature of 250°C, with a reference flow of 30,0 mL/min and a makeup flow of helium at 2,0 mL/min. No negative polarity was applied, and the filament was utilized for detection. Similar to the FID, the data rate for the TCD detector was set for a minimum peak width of 5 Hz over a duration of 0,04 minutes.

2.5.2.2 GC-MS

Gas chromatography-mass spectrometry (GC-MS) is a powerful analytical technique commonly employed for the identification of various compounds in complex mixtures, making it particularly suitable for analysing the products resulting from the oxidation of hexane to hexanol. The GC-MS system utilized in this study, comprising the GCMS-QP2010 SE [172] coupled with a GC-2010 Plus [173] and an AOC-20i auto injector [174], offers several advantages for compound identification.

Firstly, GC-MS allows for the separation of individual compounds present in a mixture based on their chemical properties and boiling points. The gas chromatograph separates the compounds as they travel through a chromatographic column, while the mass spectrometer detects and analyses the separated compounds based on their mass-to-charge ratios. This separation capability enables the identification of a wide range of compounds in the sample, including both major and minor components.

Secondly, the mass spectrometer provides highly specific information about the molecular structure of the separated compounds. By ionizing the individual compounds and measuring the mass-to-charge ratios of the resulting ions, the mass spectrometer generates unique mass spectra for each compound, which serve as molecular fingerprints. These spectra can be compared against reference databases to identify unknown compounds with high confidence.

Additionally, GC-MS offers exceptional sensitivity and selectivity, allowing for the detection and quantification of compounds present in trace amounts. This is particularly advantageous when analysing complex mixtures, as it enables the detection of low-concentration compounds that may be critical for understanding reaction pathways or assessing product purity.

Furthermore, the automation capabilities of the GC-MS system, facilitated by the AOC-20i auto injector, streamline the analytical process and enhance reproducibility. The auto injector precisely introduces samples into the chromatographic system, reducing the risk of human error and ensuring consistent sample handling across multiple analyses.

Overall, the combination of gas chromatography and mass spectrometry in the GC-MS system provides a robust and versatile platform for the identification and characterization of compounds in the oxidation products of hexane to hexanol.

a) Method specifications

The injector settings include performing 3 rinses with solvent both before and after the run, along with 3 rinses with the sample. The plunger speed for suction is set to high, with a viscosity compensation time of 0,2 seconds. High speeds are also applied for plunger injection and syringe insertion. The injection mode is set to normal.

Moving on to the gas chromatograph, the column oven temperature is maintained at 35°C, while the injection temperature is set to 280°C. Split injection mode is utilized with a sampling time of 1 minute. Helium is used as the carrier gas, with primary pressure ranging from 72,5 to 130,5 psi and a fixed pressure of 7,3 psi. The total flow rate is 61,4 mL/min, with a column flow rate of 2,78 mL/min and a linear velocity of 60,0 cm/sec. Purge flow is set at 3,00 mL/min, and the split ratio is 20,0.

In the oven, a hold time of 7 minutes at 35°C is followed by a ramp of 10°C/min until reaching 270°C, where it is held for 3 minutes, resulting in a total run time of 33,5 minutes.

The column specifications include the use of a TRB-WAX column, with dimensions of 30,0 m length, 0,25 µm thickness, and 0,32 mm diameter [175].

For the mass spectrometer, the ion source temperature is maintained at 200°C, with an interface temperature of 250°C. Solvent cut time is set to 0 minutes, and a micro scan width of 0 u is applied. The detector voltage is relative to the tuning result (0 kV), with a threshold of 0. The program parameters include a start time of 0,20 minutes, an end time of 34,00 minutes, a scan acquisition mode, an event time of 0,05 seconds, a scan speed of 10000, and start and end m/z values of 10,00 and 300,00, respectively.

2.6 Conversion and selectivity

In the context of oxidizing hexane to hexanol, measuring conversion and selectivity is crucial for evaluating the success and quality of the experiments.

Conversion refers to the percentage of the reactant (hexane) that has been converted during the reaction. It provides insight into the efficiency of the reaction process, indicating how effectively the reactant is being transformed into the products. A high conversion rate suggests that a significant portion of the hexane is being converted to hexanol or other compounds, indicating much oxidation. Conversely, a low conversion rate may indicate inefficiencies in the reaction conditions or catalyst activity, highlighting areas for improvement.

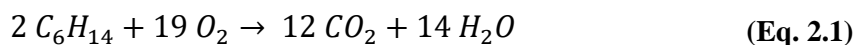
Selectivity, on the other hand, refers to the ratio of the desired product (hexanol) formed to the total products generated during the reaction. It indicates the extent to which the desired product is selectively produced over undesired by-products or side reactions. High selectivity implies that the reaction predominantly yields the desired product, minimizing the formation of by-products. This is desirable as it maximizes the yield of the target compound while reducing waste and simplifying downstream purification processes. Low selectivity, on the contrary, suggests that the reaction may be producing a significant amount of undesired by-products, indicating the need for optimization to enhance the selectivity towards hexanol.

In summary, measuring conversion and selectivity provides valuable insights into the efficiency, effectiveness, and quality of the hexane oxidation process. High conversion and selectivity rates are indicative of successful reactions with minimal side reactions, leading to improved process efficiency and higher-quality product yields. Tracking these parameters allows to optimize reaction conditions, catalysts, and protocols to achieve desired outcomes and advance the development of efficient oxidation processes.

2.6.1 Calculations

Since the detector in the used GC is of the FID type, it is possible to simply compare the peak areas. This is because, for FID detections, the sample gets oxidized to CO_2 and H_2O , as given in the case of hexane in **Eq. 2.1**. Afterwards, the amount of CO_2 that passes the detector is measured. For all C6 molecules, the same peak area corresponds to the same amount of moles and therefore concentration. Since all of the by-products are organic molecules, it is possible to compare peak areas. However, since the by-product are possibly C2 and C3, a correction may be needed in order to compare the areas to each other because both conversion and selectivity are calculated on a molar basis. C2 molecules give a 3 times weaker signal per mole at the FID compared to C6 molecules, and C3 molecules give a 2 times weaker signal, as follows from the explanation given at the beginning of this paragraph. Because of this phenomenon, each peak shown in the chromatogram must be carefully assigned to a certain molecule. For the identification of these molecules, GC-MS is used. Later, the peak area relative to hexanol (C6) is calculated by multiplying the peak area by the relevant multiple. For example, in the case of propanoic acid (C3), the peak area needs to be multiplied by 2 to obtain the relative peak area.

The definition of conversion is the amount of moles of products formed divided by the amount of moles of hexane before reaction. This means that the conversion is equal to the sum of the relative peak areas of the products divided by the peak area of 100% hexane, since the non-polar phase consists of pure hexane at the beginning of the reaction (**Eq. 2.2**). Moreover, selectivity is calculated by dividing the amount of moles of hexanol by the amount of products after reaction. When translated to the practical calculations, using peak area, it comes down to the division of the peak area of the formed hexanol by the sum of the relative peak areas of the products (**Eq. 2.3**).



$$\begin{aligned} \text{Conversion \%} &= \frac{\text{moles of products formed}}{\text{moles of hexane before reaction}} \times 100 \\ &= \frac{\sum \text{relative areas of the products}}{\text{peak area of hexane}} \times 100 \end{aligned} \quad \text{(Eq. 2.2)}$$

$$\begin{aligned} \text{Selectivity \%} &= \frac{\text{moles of hexanol formed}}{\text{moles of products formed}} \times 100 \\ &= \frac{\text{peak area of hexanol}}{\sum \text{relative areas of the products}} \times 100 \end{aligned} \quad \text{(Eq. 2.3)}$$

3 Results and Discussion

3.1 Characterisation

3.1.1 Nitrogen adsorption analysis

3.1.1.1 Isotherms

The nitrogen adsorption-desorption isotherms for MIL-100 MOF, HKUST-1, and MOF-808 @His-Cu provide critical insights into their pore structures and surface properties. The isotherm for MIL-100 MOF (**Figure 21**) exhibits a steep initial increase, followed by a plateau, and then a sharp rise at high relative pressures with a clear hysteresis loop. This pattern is indicative of a combination of Type I and Type IV isotherms, characteristic of respectively microporous and mesoporous materials. The hysteresis loop, resembling either type H1 or H2, suggests the presence of uniform cylindrical pores or ink-bottle shaped pores. The initial steep increase signifies the presence of micropores, the plateau indicates multilayer adsorption on the surface of mesopores, and the hysteresis loop confirms capillary condensation occurring within these mesopores.

In contrast, the isotherm for HKUST-1 (**Figure 22**) also demonstrates an initial increase, a plateau, and a sharp rise at high relative pressures with a hysteresis loop. This isotherm similarly aligns with a Type IV classification, indicating mesoporous materials. However, the hysteresis loop appears more complex, likely indicating ink-bottle shaped pores (type H2). The gradual increase and plateau observed in the isotherm suggest the presence of mesopores, while the sharp rise at high relative pressures and the hysteresis loop corroborate the existence of mesopores with ink-bottle shapes.

The isotherm for MOF-808 @His-Cu (**Figure 23**) presents a very gradual increase, a slight plateau, and a sharp rise at high relative pressures, accompanied by a hysteresis loop. This isotherm, though less pronounced in adsorption at lower pressures, also falls under the Type IV category, suggesting mesoporous characteristics. The hysteresis loop, potentially of type H3 or H4, indicates the presence of slit-shaped mesopores. The very gradual increase points to fewer mesopores or possibly smaller mesopores, while the slight plateau reflects limited multilayer adsorption. The hysteresis loop confirms the existence of mesopores, likely with a slit-like shape.

In summary, the nitrogen adsorption-desorption isotherms for MIL-100 MOF, HKUST-1, and MOF-808 @His-Cu reveal significant details about their pore structures. MIL-100 MOF and HKUST-1 exhibit mesoporous characteristics with distinct hysteresis loops indicative of uniform cylindrical or ink-bottle shaped pores. In contrast, MOF-808 @His-Cu shows a more gradual adsorption behaviour with slit-shaped mesopores, as evidenced by its hysteresis loop.

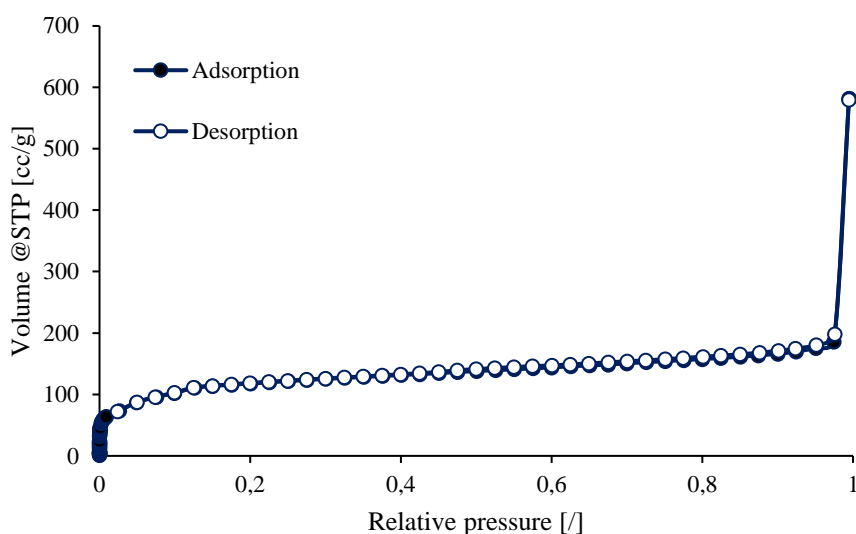


Figure 21: Nitrogen adsorption-desorption isotherm MIL-100

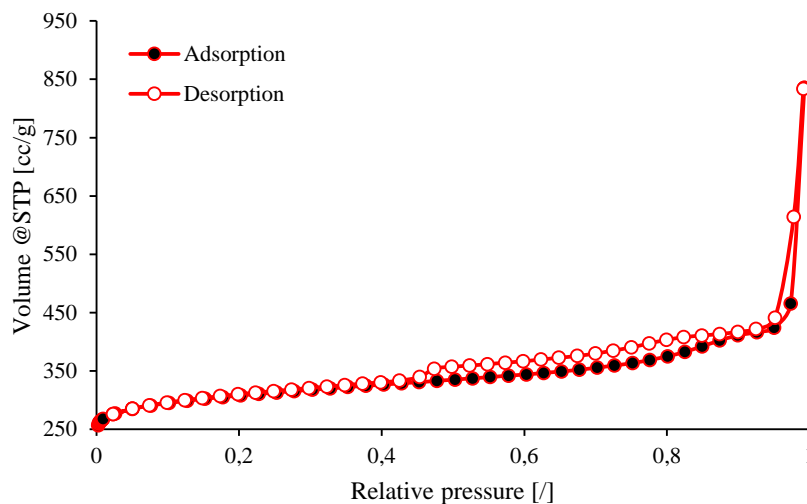


Figure 22: Nitrogen adsorption-desorption isotherm HKUST-1

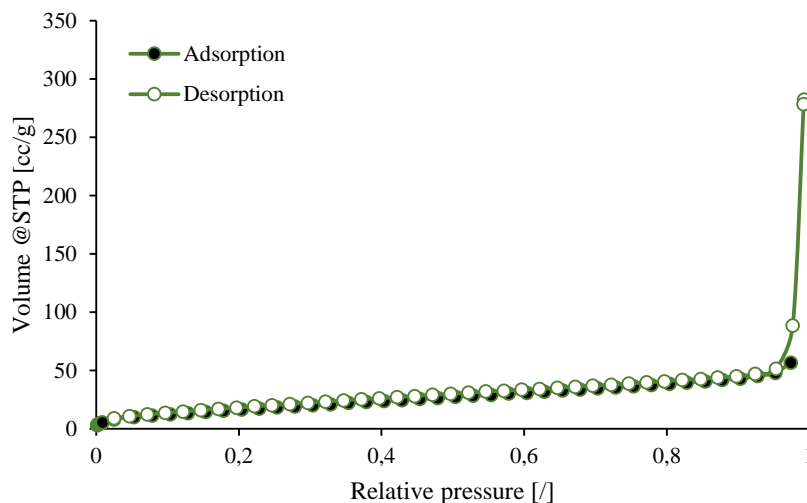


Figure 23: Nitrogen adsorption-desorption isotherm MOF-808 @His-Cu

3.1.1.2 Surface area

As shown in **Table 1**, MIL-100 exhibits a high micropore surface area of 1373,8 m²/g, indicating significant microporosity. Additionally, it has a considerable mesopore surface area of 173,7 m²/g and a macropore surface area of 154,3 m²/g. The total surface area of MIL-100 is 1701,7 m²/g, reflecting its highly porous nature due to the combined contributions from micropores, mesopores, and macropores. Moreover, the external surface area is 327,9 m²/g, indicating a substantial outer surface area accessible without entering the pore network.

HKUST-1 also demonstrates notable microporosity with a micropore surface area of 751,5 m²/g. Its mesopore surface area is similar to MIL-100, at 174,2 m²/g, while the macropore surface area is relatively small at 29,7 m²/g. The total surface area of HKUST-1 is 955,4 m²/g, which, although substantial, is lower than that of MIL-100. The external surface area of HKUST-1 is 203,9 m²/g, indicating significant accessibility to the surface without penetrating the pores.

In contrast, MOF-808 @His-Cu shows no microporous surface area, reflecting an absence of micropores in its structure. It has a relatively low mesopore surface area of 39,3 m²/g and a macropore surface area of 27,5 m²/g. The total surface area of MOF-808 @His-Cu is significantly lower than both MIL-100 and HKUST-1, at 66,7 m²/g. Interestingly, the external surface area is equal to the total surface area (66,7 m²/g), indicating that all the surface area is on the outer surface with no internal porosity contributing to the surface area.

In summary, MIL-100 is highly porous with significant contributions from micropores, mesopores, and macropores, resulting in a high total and external surface area. HKUST-1 has substantial microporous and mesoporous surface areas with fewer macropores, leading to a considerable total surface area, though less than MIL-100. MOF-808 @His-Cu lacks microporosity, has limited mesoporosity and macroporosity, and all surface area is external, resulting in a low total surface area compared to the other two MOFs. These surface area characteristics influence the potential applications of these MOFs in fields such as gas adsorption, catalysis, and separation processes. MIL-100's high surface area and diverse pore sizes make it particularly versatile, while HKUST-1's balanced porosity offers significant utility, and MOF-808 @His-Cu's properties might be suited for specific applications requiring predominantly external surface interactions.

Table 1: Surface areas

	MIL-100	HKUST-1	MOF-808 @His-Cu
Micropore surface area [m ² /g]	1373,8	751,5	0,0
Mesopore surface area [m ² /g]	173,7	174,2	39,3
Macropore surface area [m ² /g]	154,3	29,7	27,5
Total surface area [m ² /g]	1701,7	955,4	66,7
External surface area [m ² /g]	327,9	203,9	66,7

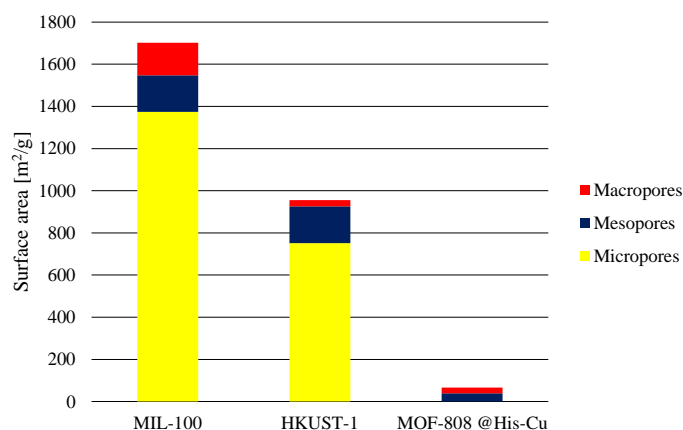


Figure 24: Surface areas per MOF

3.1.1.3 Pore volume and size distribution

Table 2 provides a detailed breakdown of the pore volumes for the three different Metal-Organic Frameworks: MIL-100, HKUST-1, and MOF-808 @His-Cu.

MIL-100 shows a significant micropore volume of 0,686 cc/g, indicating a substantial proportion of its porosity is due to micropores. This is complemented by a mesopore volume of 0,524 cc/g, suggesting that MIL-100 also has a considerable amount of mesoporosity. Additionally, the macropore volume of 0,104 cc/g, although smaller compared to the micropore and mesopore volumes, indicates the presence of macropores. The total pore volume of MIL-100 is 1,314 cc/g, reflecting its highly porous nature, with a balanced distribution across micropores, mesopores, and macropores.

HKUST-1, on the other hand, has a micropore volume of 0,389 cc/g, which is lower than that of MIL-100, indicating less microporosity. However, HKUST-1 exhibits a higher mesopore volume of 0,873 cc/g, suggesting a greater contribution from mesopores. The macropore volume for HKUST-1 is relatively low at 0,033 cc/g. The total pore volume of HKUST-1 is 1,295 cc/g, which is slightly less than that of MIL-100, but still indicates significant porosity primarily contributed by mesopores and micropores.

MOF-808 @His-Cu displays no microporosity with a micropore volume of 0,000 cc/g, indicating an absence of micropores. The mesopore volume is 0,417 cc/g, which shows that mesopores are the primary contributors to its porosity. The macropore volume is also low at 0,020 cc/g. Consequently, the total pore volume for MOF-808 @His-Cu is 0,437 cc/g, significantly lower than both MIL-100 and HKUST-1. This indicates that MOF-808 @His-Cu has a much lower overall porosity, with the mesopores contributing the most to the limited pore volume.

In summary, MIL-100 has a well-distributed porosity with significant contributions from micropores, mesopores, and macropores, resulting in the highest total pore volume among the three MOFs. HKUST-1 has a lower micropore volume but compensates with a high mesopore volume, leading to a total pore volume almost equivalent to MIL-100. MOF-808 @His-Cu, with no micropores and limited mesopore and macropore volumes, has the lowest total pore volume, indicating a significantly less porous structure compared to MIL-100 and HKUST-1. These differences in pore volumes are crucial for determining the suitability of each MOF for specific applications, such as gas adsorption, catalysis, and separation processes.

Table 2: Pore volumes and size distribution

	MIL-100	HKUST-1	MOF-808 @His-Cu
Micropore volume [cc/g]	0,686	0,389	0,000
Micropore volume [%]	52,21%	30,04%	0,00%
Mesopore volume [cc/g]	0,524	0,873	0,417
Mesopore volume [%]	39,88%	67,41%	95,47%
Macropore volume [cc/g]	0,104	0,033	0,020
Macropore volume [%]	7,91%	2,55%	4,53%
Total pore volume [cc/g]	1,314	1,295	0,437

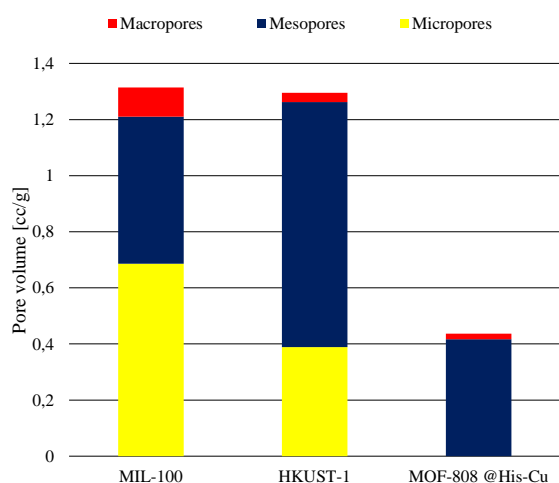


Figure 25: Pore volume per MOF

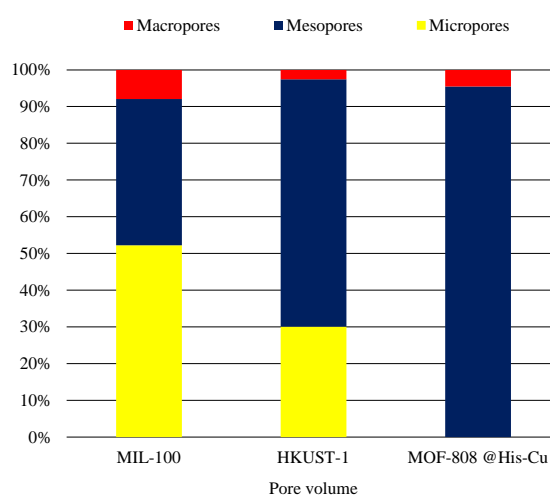


Figure 26: Pore size distribution per MOF

3.1.2 XRD

After analysing the XRD diagrams of my metal-organic frameworks (MOFs) and comparing them with simulated versions from a trustworthy databases, several conclusions can be drawn about the quality and structural characteristics of MIL-100, HKUST-1, and MOF-808 @His-Cu as stated below. The data for the simulated versions can be found for MIL-100 in the Crystallography Open Database (COD ID: 7102029) [176], HKUST-1 in the Crystallography Open Database (COD ID: 2300381) [177], and MOF-808 @His-Cu in [178].

For MIL-100, the XRD pattern (**Figure 27**) shows the same peaks as the simulated version, indicating that the synthesized material is indeed the intended MOF and free from impurities. The peaks, while broader than those in the simulated pattern, are not especially wide compared to literature values, suggesting a relatively high degree of crystallinity, though not ideal. However, the peaks are not very symmetrical, which might indicate the presence of structural defects or strain within the crystal lattice. Additionally, the intensity of the peaks at lower angles is lower compared to the simulated version, which could imply a reduction in long-range order or changes in particle size and shape.

In the case of HKUST-1, the XRD pattern (**Figure 28**) is almost identical to the simulated version, with the exception of one unidentified peak. This discrepancy could suggest the presence of impurities, secondary phases, or incomplete synthesis. The peaks in the experimental pattern are broader than in the simulated version but, similar to MIL-100, are not especially wide compared to literature, indicating a relatively high degree of crystallinity. The peaks are quite symmetrical, suggesting fewer structural defects or strain compared to MIL-100. However, the intensity of the peaks at lower angles is lower than in the simulated version, implying a potential decrease in long-range order or variations in particle size and shape.

For MOF-808 @His-Cu, the experimental XRD peaks (**Figure 29**) can be more or less assigned to the simulated ones, but not completely. This partial alignment suggests that impurities, secondary phases, or incomplete synthesis are present. The peaks are wider than in the simulated version but not excessively wide compared to literature, implying a relatively high degree of crystallinity, though not ideal. The peak symmetry for MOF-808 @His-Cu is in between that of MIL-100 and HKUST-1, indicating that there may be moderate structural defects or strain present. Moreover, the intensity of the peaks at lower angles is lower than in the simulated version, suggesting a possible reduction in long-range order or alterations in particle size and shape.

Overall, the XRD analysis indicates that MIL-100 is synthesized with high purity and relatively high crystallinity, though it may have some structural defects or strain. HKUST-1 is nearly as pure but has a minor impurity and displays good crystallinity with fewer structural issues. MOF-808 @His-Cu shows signs of impurities or incomplete synthesis and moderate structural defects, though it still maintains a relatively high degree of crystallinity. The reduced intensity of peaks at lower angles in all the MOFs points to a potential decrease in long-range order or changes in particle size and shape, which could affect their material properties and applications. These insights contribute to the understanding of the material properties and potential applications of these MOFs.

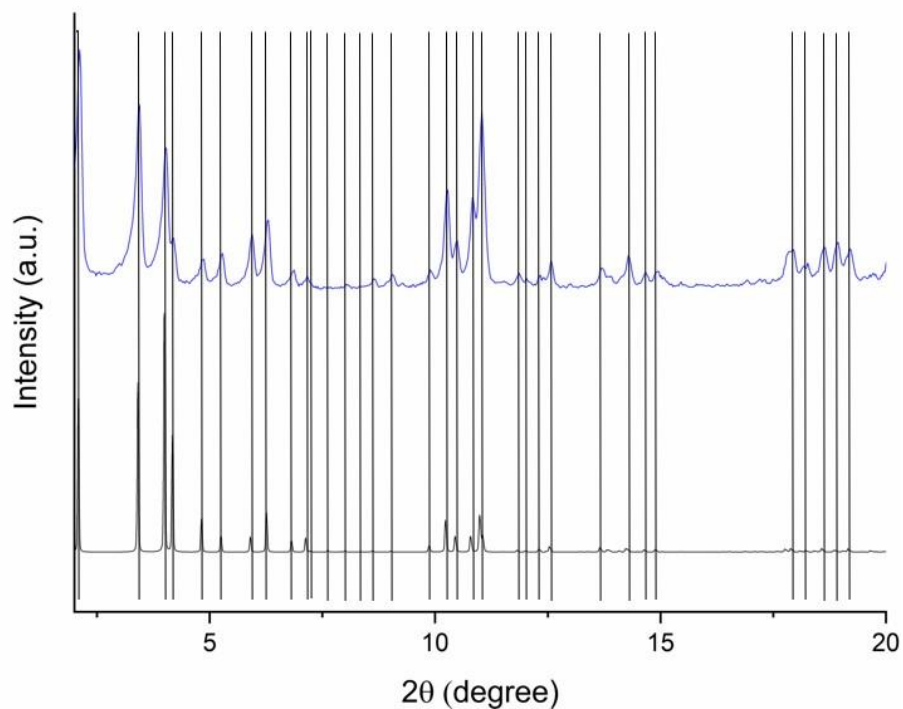


Figure 27: XRD MIL-100 used (top) and simulated (bottom)

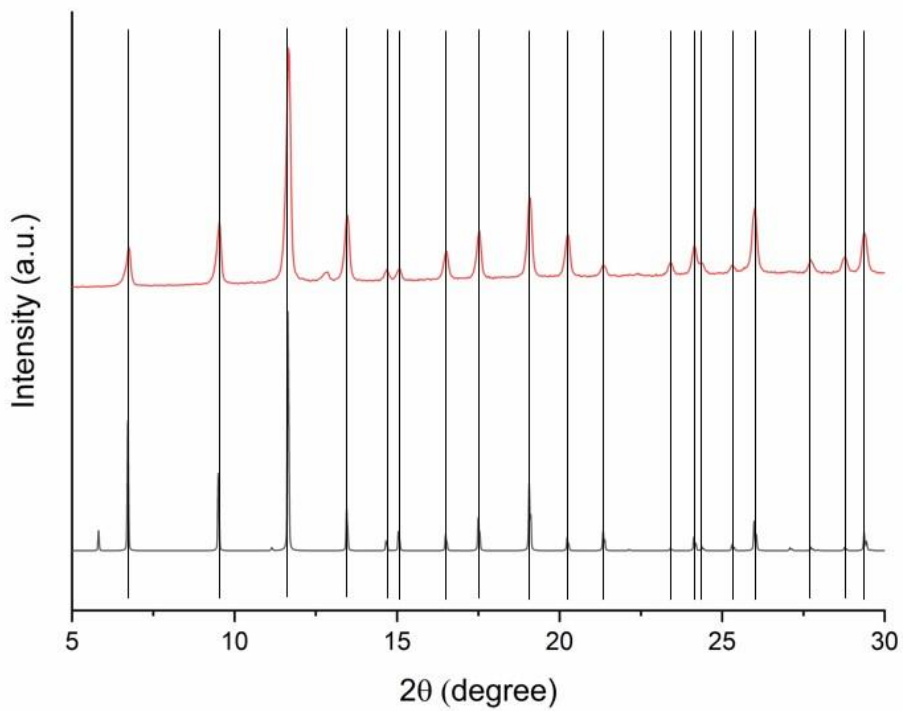


Figure 28: XRD HKUST-1 used (top) and simulated (bottom)

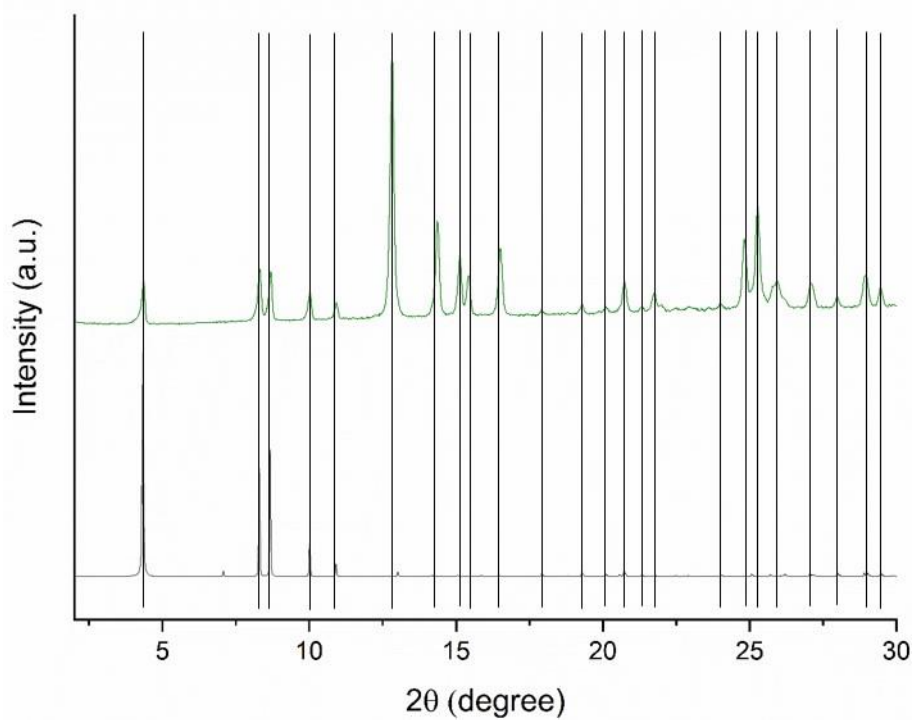


Figure 29: XRD MOF-808 @His-Cu used (top) and simulated (bottom)

3.1.3 FE-SEM

3.1.3.1 MIL-100

The SEM images of MIL-100 (**Figure 30** and **Figure 31**) display a highly porous structure composed of polyhedral like structures. These structures differ slightly in size but are relatively consistent. The small variation in size can be attributed to the practical limitations of maintaining identical synthesis conditions. The polyhedral shape is a characteristic feature of MIL-100, reflecting its highly ordered and crystalline nature. The surfaces of these polyhedral grains are rather smooth and well-defined, with visible planes that indicate a lack of significant surface roughness or irregularities. This smoothness is a sign of high crystallinity and minimal structural defects, as confirmed by XRD analysis.

The SEM images do not show foreign particles or amorphous regions, indicating the high purity synthesis of MIL-100. Additionally, the morphology observed is consistent across different regions of the sample, demonstrating uniform synthesis conditions and reliable replication of the MIL-100 structure. The SEM images closely match those found in the literature for MIL-100 samples. These features collectively suggest that the synthesis process has produced high-quality MIL-100 with the expected morphology, structural integrity, and purity, making it suitable for various applications such as gas adsorption, catalysis, and separation processes.

3.1.3.2 HKUST-1

The SEM images of HKUST-1 (**Figure 32** and **Figure 33**) display octahedral crystals, a distinctive morphology characteristic of HKUST-1, reflecting its highly ordered and crystalline nature. These octahedral crystals differ slightly in size but are relatively consistent, similar to MIL-100. This small variation in size can be attributed to the practical limitations of maintaining identical synthesis conditions. The faces of the octahedral crystals are smooth and well-defined, without significant surface roughness or irregularities. This smoothness is indicative of high crystallinity and minimal defects. The overall image reflects high crystallinity, with sharp and distinct edges of the octahedra, aligning with the high purity and well-ordered structure of HKUST-1 as indicated by XRD analysis.

The SEM images do not show foreign particles or amorphous regions, indicating the high purity synthesis of HKUST-1. Additionally, the morphology observed is consistent across different regions of the sample, demonstrating uniform synthesis conditions and reliable replication of the HKUST-1 structure. The SEM images closely match those found in the literature for high-quality HKUST-1 samples. These features collectively suggest that the synthesis process has produced high-quality HKUST-1 with the expected morphology, structural integrity, and purity, making it suitable for various applications such as gas adsorption, catalysis, and separation processes.

3.1.3.3 MOF-808 @His-Cu

The SEM images of MOF-808 @His-Cu (**Figure 34** and **Figure 35**) reveal a less porous structure characterized by octahedral crystals. These crystals exhibit slight variations in size, similar to what is observed for MIL-100 and HKUST-1. The octahedral shape of the crystals is a distinctive trait of MOF-808 @His-Cu, indicative of its highly organized and crystalline nature.

The surfaces of these octahedral crystals appear smooth and precisely defined, featuring sharp edges and flat faces that suggest minimal surface roughness or irregularities, consistent with XRD analysis. Notably, the SEM images show no significant presence of foreign particles or amorphous regions. These SEM observations closely correspond to those reported in the literature for MOF-808 @His-Cu samples.

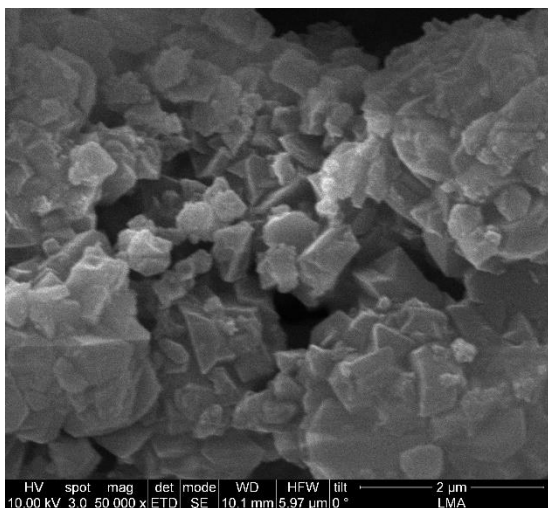


Figure 30: SEM image MIL-100 (2 μm)

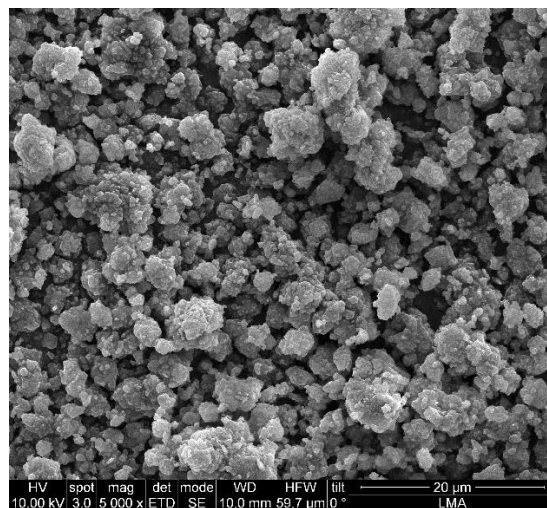


Figure 31: SEM image MIL-100 (20 μm)

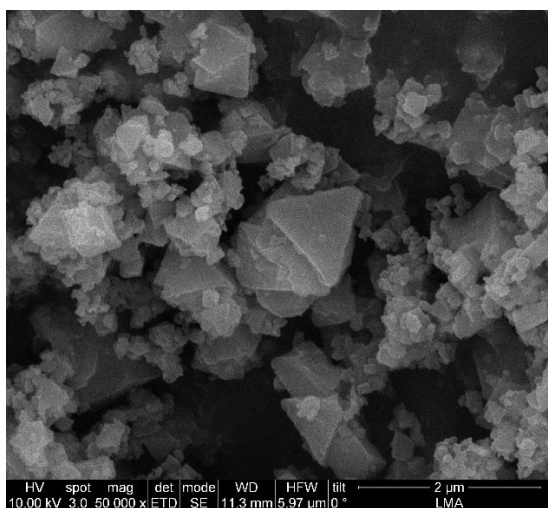


Figure 32: SEM image HKUST-1 (2 μm)

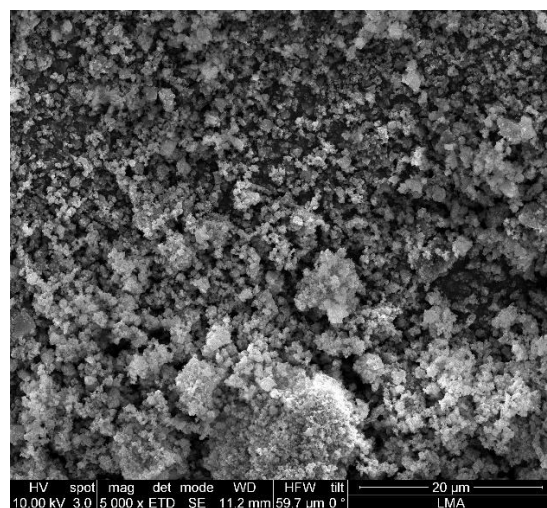


Figure 33: SEM image HKUST-1 (20 μm)

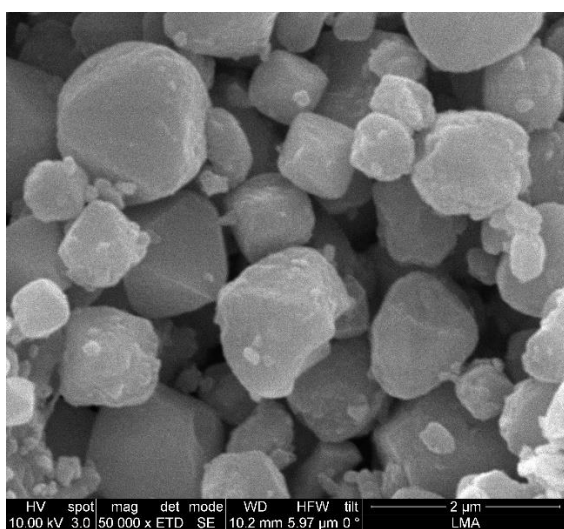


Figure 34: SEM image MOF-808 @His-Cu (2 μm)

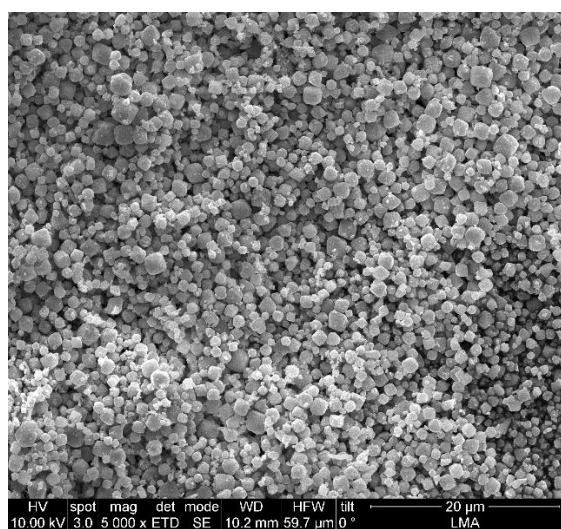


Figure 35: SEM image MOF-808 @His-Cu (20 μm)

3.1.4 TGA

3.1.4.1 N₂ gas flow of 20mL/min with 5,0 K/min ramp

The thermogravimetric analysis (TGA) of MIL-100, presented in **Figure 36**, reveals that the decomposition of this MOF starts at 422°C under inert conditions, reaching its peak at 485°C. These values notably exceed those observed for HKUST-1 and MOF-808 @His-Cu, as depicted in **Figure 37** and **Figure 38**, respectively. Under inert conditions, HKUST-1 begins to decompose at 253°C, while MOF-808 @His-Cu starts decomposing at an even lower temperature of 140°C. The decomposition rates for HKUST-1 and MOF-808 @His-Cu reach their maximums at 327°C and 230°C, respectively.

It is also important to note that all samples exhibit significant weight loss at relatively low temperatures, which is attributed to the removal of adsorbed or residual solvent molecules used during synthesis. This solvent loss does not indicate the decomposition of the MOFs themselves and, therefore, does not reflect the intrinsic thermal stability of the MOF structures.

In summary, under inert conditions, MIL-100 demonstrates the highest resistance to decomposition at elevated temperatures, followed by HKUST-1 and then MOF-808 @His-Cu. This order reflects the decreasing thermal stability of the MOFs, with MIL-100 showing the greatest stability, indicating its suitability for applications requiring higher thermal resistance in inert (N₂ gas flow) circumstances.

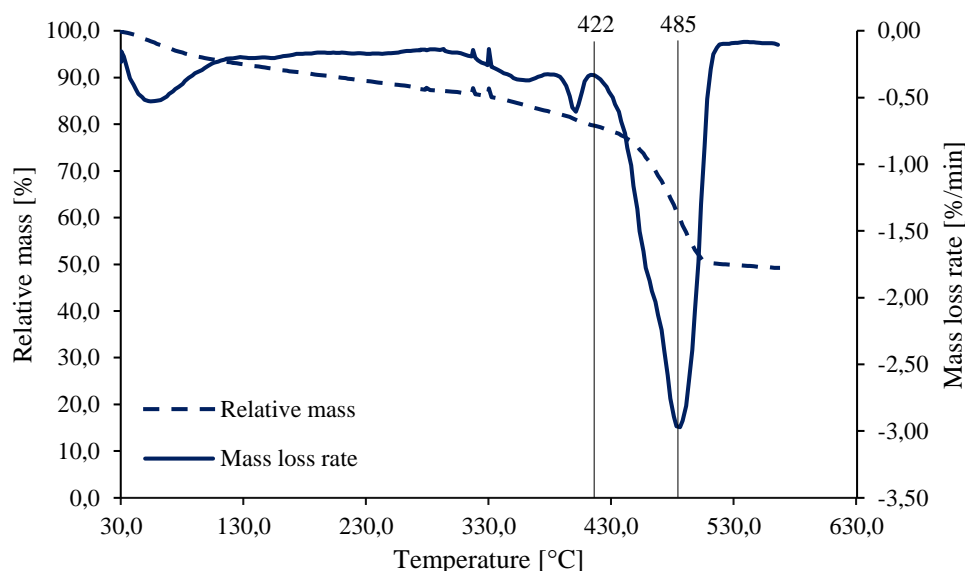


Figure 36: TGA of MIL-100 at constant N₂ gas flow with 5,0 K/min ramp

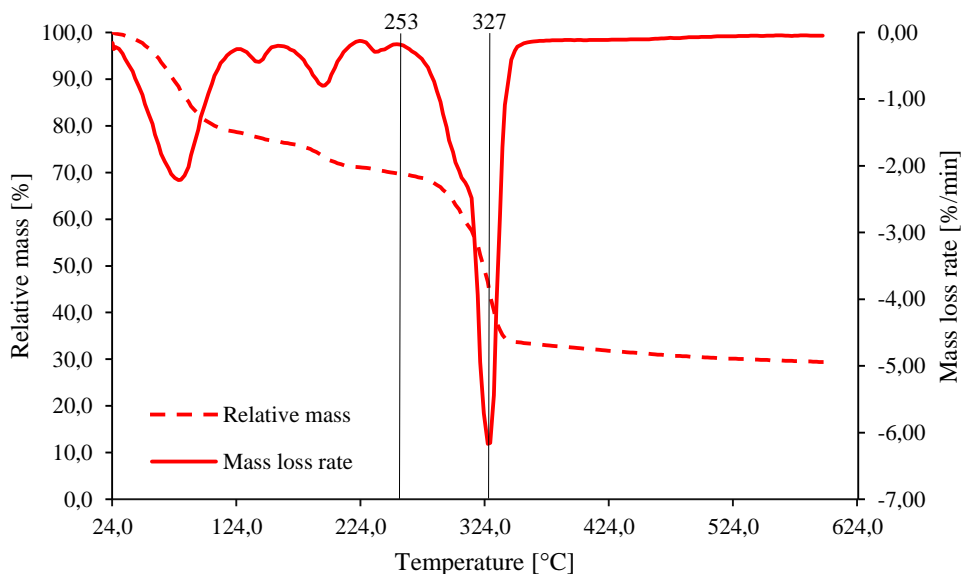


Figure 37: TGA of HKUST-1 at constant N₂ gas flow with 5,0 K/min ramp

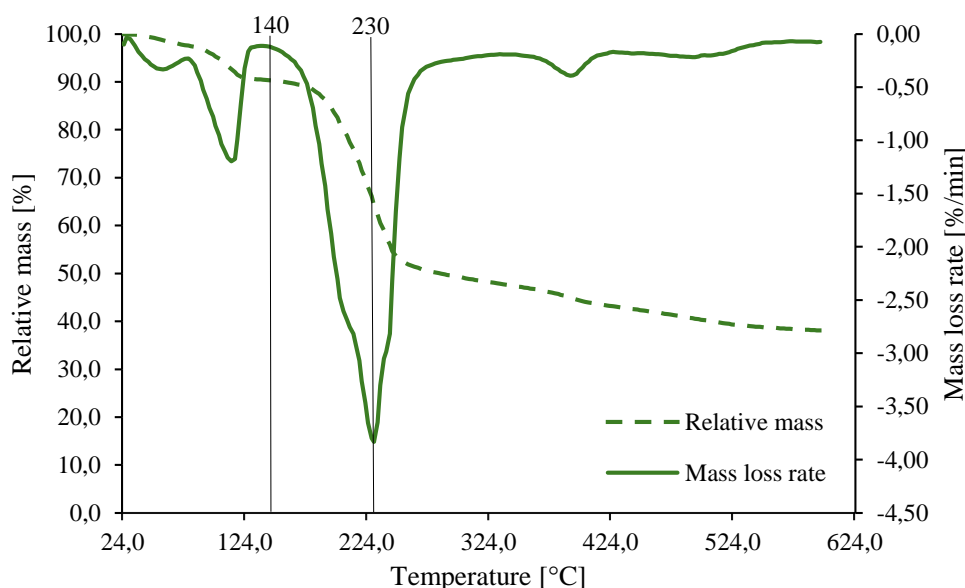


Figure 38: TGA of MOF-808 @His-Cu at constant N₂ gas flow with 5,0 K/min ramp

3.1.4.2 O₂ gas flow of 20mL/min with 5,0 K/min ramp

Under oxidative conditions (Figure 39), MIL-100 begins to decompose at a lower temperature compared to its decomposition in an inert atmosphere (Figure 36). This can be explained by the fact that the presence of oxygen facilitates the oxidative degradation of the organic linkers within the MOF structure. The oxygen molecules can react with the organic components of MIL-100, leading to an earlier onset of decomposition. Furthermore, the maximum decomposition rate of MIL-100 also occurs at a lower temperature in the oxidative atmosphere. This indicates that the overall decomposition process is accelerated in the presence of oxygen, likely due to oxidative cleavage of the bonds within the framework, resulting in a faster breakdown of the structure.

Contrary to MIL-100, MOF-808 @His-Cu shows an increase in both the onset and maximum decomposition temperatures under oxidative conditions (**Figure 41**) compared to an inert atmosphere (**Figure 38**). This suggests that the presence of oxygen enhances the stability of MOF-808 @His-Cu up to a certain temperature. One possible explanation for this behaviour is that the oxidative environment might induce a passivation effect, where a protective oxide layer forms on the surface of the MOF, temporarily increasing its thermal stability. This oxide layer could inhibit further degradation until higher temperatures are reached, thus shifting the decomposition to higher temperatures.

For HKUST-1, the decomposition behaviour under oxidative conditions (**Figure 40**) is more complex. The onset of decomposition occurs at a higher temperature than in an inert atmosphere, indicating that the initial thermal stability is improved in the presence of oxygen. This could be due to similar passivation effects as seen in MOF-808 @His-Cu or possibly due to the formation of stable intermediate compounds that delay the initial decomposition. However, the maximum decomposition rate is reached at a lower temperature under oxidative conditions. This dual behaviour suggests that while the initial stages of decomposition are inhibited, once the decomposition starts, it proceeds more rapidly. This rapid decomposition could be due to the oxidative cleavage of the linkers or the interaction of oxygen with the decomposition products, which might catalyse further degradation of the MOF.

The observed differences in the decomposition behaviour of MIL-100, HKUST-1, and MOF-808 @His-Cu under oxidative and inert conditions highlight the intricate interplay between the MOF structures and their gaseous environments. The presence of oxygen can either facilitate or inhibit the decomposition process depending on the specific interactions between the MOF components and the oxidative atmosphere. Understanding these interactions is crucial for optimizing the thermal stability and performance of MOFs in various applications, particularly those involving oxidative environments.

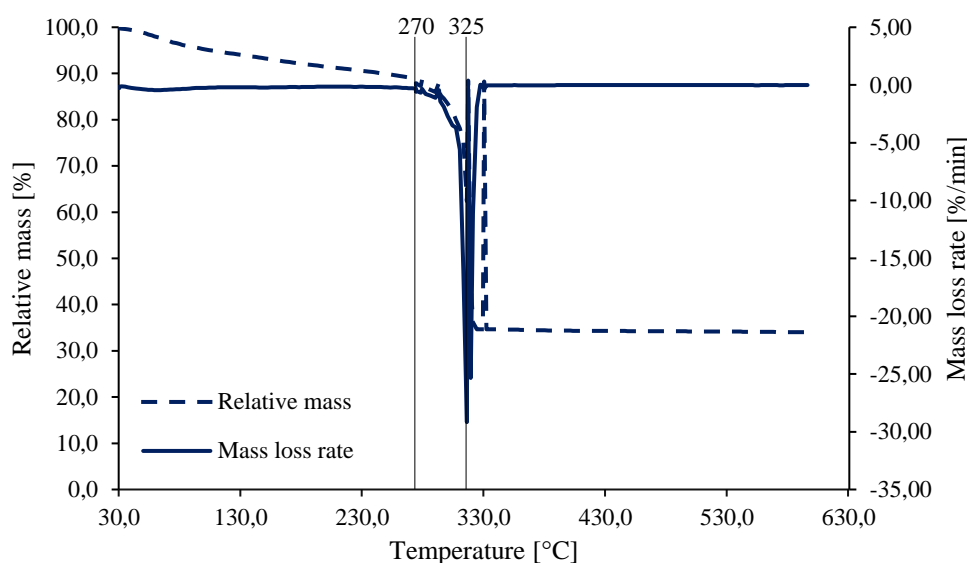


Figure 39: TGA of MIL-100 at constant O₂ gas flow with 5,0 K/min ramp

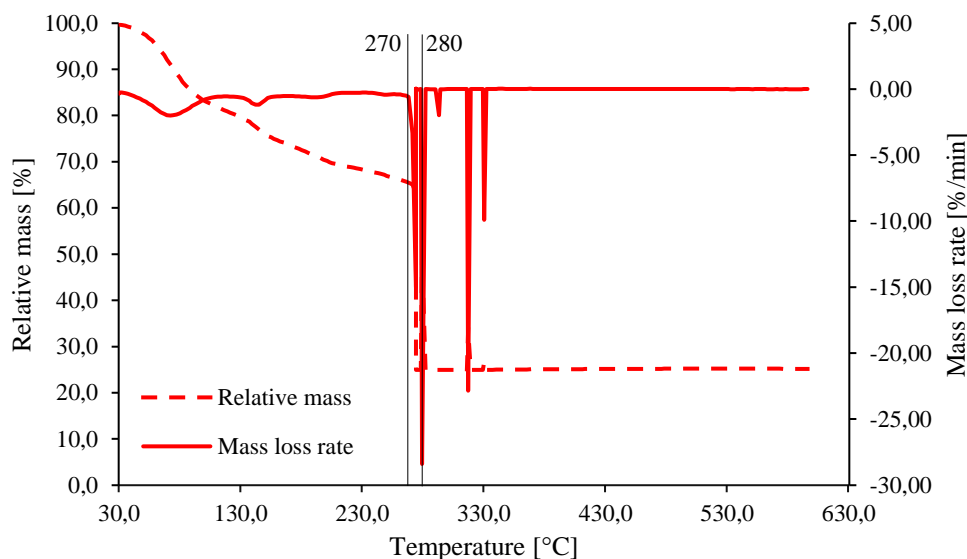


Figure 40: TGA of HKUST-1 at constant O₂ gas flow with 5,0 K/min ramp

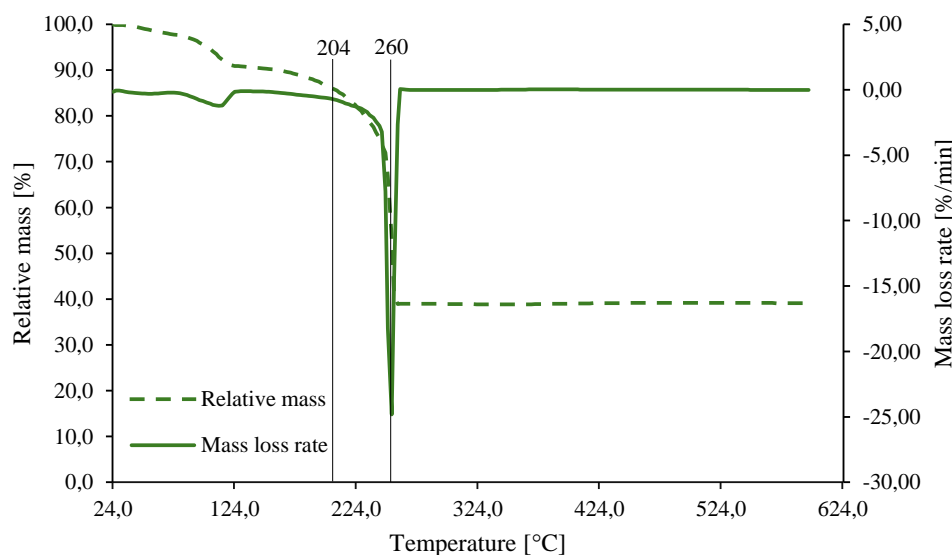


Figure 41: TGA of MOF-808 @His-Cu at constant O₂ gas flow with 5,0 K/min ramp

3.1.4.3 Isothermal conditions at 200°C with constant 250 mL/min N₂ gas flow

When analysing the isothermal TGA data for the considered metal-organic frameworks (MOFs), as plotted in **Figure 42**, it is observed that the least stable MOFs decompose the fastest initially, but after some time, all samples appear to be stable. This phenomenon can be explained by considering the decomposition kinetics and the structural properties of the MOFs. The most stable MOF, MIL-100, decomposes the slowest initially and maintains stability throughout the isothermal period, indicating strong bonds and a highly robust structure at the given circumstances. HKUST-1 shows moderate initial decomposition, indicating it has intermediate bond strengths and structural stability compared to the other two. The least stable MOF, MOF-808 @His-Cu, decomposes the fastest initially due to weaker bonds and more structural defects, as observed from XRD characterisation (3.1.2), but stabilizes over time as the labile components decompose and a more stable residue forms.

In the initial stages of the isothermal TGA, MOF-808 @His-Cu decomposes the fastest. This is because MOF-808 @His-Cu has weaker bonds and less robust structural integrity compared to MIL-100 and HKUST-1. MOF-808 @His-Cu likely has weaker bonds between its metal ions and organic linkers, leading to easier bond cleavage under thermal stress. This results in a rapid initial mass loss as the

weaker parts of the framework break down. Additionally, MOF-808 @His-Cu has a lower activation energy for decomposition, meaning that at a given temperature, a larger fraction of its molecules will have enough energy to overcome the energy barrier for decomposition compared to MIL-100 and HKUST-1. Moreover, MOF-808 @His-Cu may have more structural defects, as observed from XRD characterisation (3.1.2), which can act as initiation sites for decomposition, leading to a faster initial mass loss.

After the initial decomposition, MOF-808 @His-Cu, along with MIL-100 and HKUST-1, reaches a relatively stable phase. This stabilization can be attributed to the complete decomposition of the most thermally labile components, such as solvent molecules trapped within the pores and weakly bound organic linkers. Once these components are fully decomposed, the remaining structure is more thermally robust. During the initial decomposition, a stable residue or char may form, which is more resistant to further thermal degradation. In MOF-808 @His-Cu, after the easily decomposable parts are gone, what remains is a more stable structure that can withstand the isothermal conditions for a longer period. Once the easily decomposable fractions have decomposed, the system reaches a thermal equilibrium where the remaining material does not have sufficient energy to undergo further rapid decomposition at the given temperature.

Overall, the observed TGA behaviour makes sense because the initial rapid decomposition reflects the breakdown of the weakest parts of the MOFs. Once these parts are decomposed, the remaining structure is more thermally stable, leading to the observed stabilization in the TGA curve. MIL-100, HKUST-1, and MOF-808 @His-Cu demonstrate a clear correlation between initial decomposition rates and overall thermal stability, with MIL-100 being the most stable and MOF-808 @His-Cu the least stable.

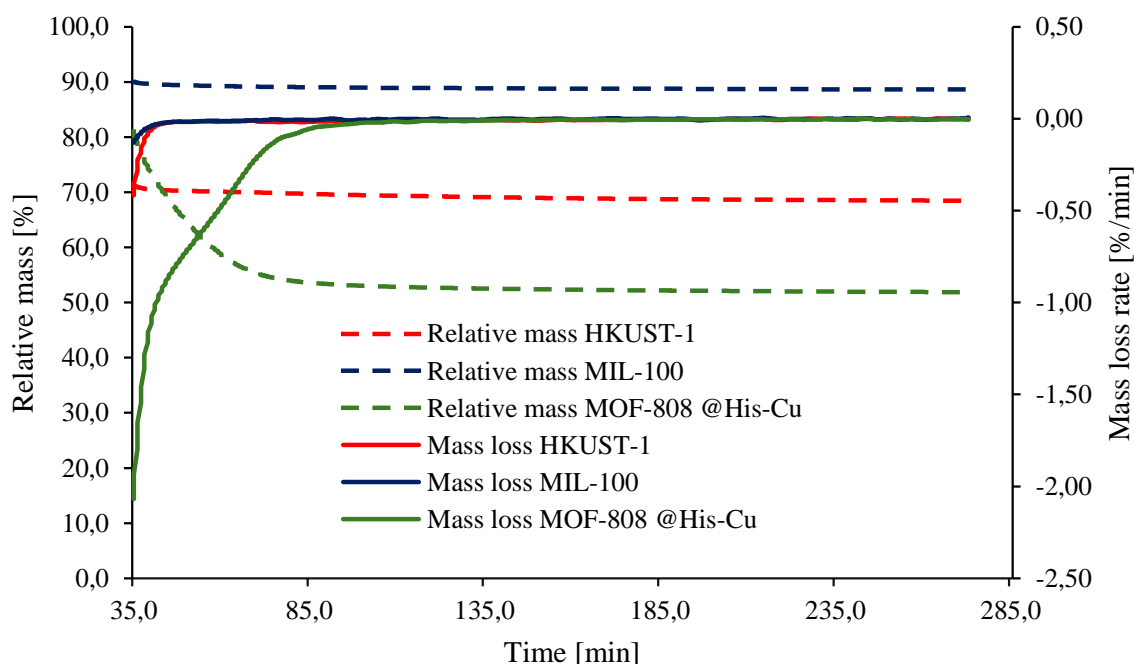


Figure 42: TGA all MOFs under isothermal (200°C) and N₂ gas flow conditions

3.2 Parameters

3.2.1 Presence of MOFs

The observed results, as presented in **Table 3**, indicate that the presence of metal-organic frameworks (MOFs) significantly enhances both the conversion and selectivity in the oxidation of hexane to hexanol when compared to experiments conducted without MOFs. This enhancement can be attributed to several key factors inherent to the catalytic properties of MOFs. Additionally, it is important to note that the conversion is kept low to remain in the kinetic regime, thereby minimizing the formation of byproducts.

MOFs provide a highly organized and porous structure, which increases the surface area available for reactions. This structural characteristic allows for greater interaction between the reactants—hexane and hydrogen peroxide—and the active catalytic sites within the MOFs. This results in a higher conversion rate of hexane to hexanol.

Moreover, MOFs are designed to offer specific active sites that stabilize the transition state of the desired reaction pathway. This selective stabilization ensures that the reaction predominantly proceeds towards the formation of hexanol, thus significantly improving selectivity. In the absence of MOFs, the reaction lacks these tailored catalytic sites, leading to lower conversion rates and potentially higher formation of undesired byproducts.

The enhanced performance in the presence of MOFs can also be attributed to their ability to facilitate the adsorption and activation of hydrogen peroxide. This activation is crucial for initiating and sustaining the oxidation process. MOFs can effectively decompose hydrogen peroxide into reactive oxygen species, which are essential for the oxidation of hexane. Without MOFs, the activation of hydrogen peroxide is less efficient, resulting in lower conversion rates.

In summary, the presence of MOFs not only increases the conversion rate of hexane to hexanol by providing an extensive surface area and highly efficient catalytic sites but also enhances selectivity by stabilizing the transition state of the desired reaction pathway. These findings underscore the significant role of MOFs as catalysts in optimizing the oxidation process, making them an invaluable component in achieving higher yields and purity of hexanol.

Table 3, as shown below, presents the data concerning the effect of the presence of MOFs. This data indicates that the presence of MOFs results in an increase in both conversion as well as selectivity, as stated earlier in this section.

Table 3: Effect of MOFs

Reaction conditions	Catalyst	Conversion	Selectivity
^a	None	0,04%	29,4%
^a	MIL-100	0,07%	42,2%
^a	HKUST-1	0,11%	37,7%

Notes: ^aReaction conditions: Catalyst mass = 100 mg, Temperature = 200 °C, Starting pressure = 1 bar, Reaction time = 2 h, *n*-hexane = 30 mL, *n*-hexane:H₂O₂ (molar) ratio = 4:1.

In **Figure 43** and **Figure 44** the effect of the presence of MOFs is presented graphically concerning conversion and selectivity respectively, as for the reaction conditions mentioned in the notes of **Table 3**.

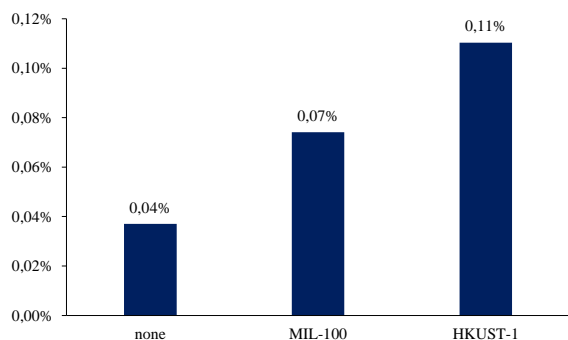


Figure 43: Effect of MOFs on conversion

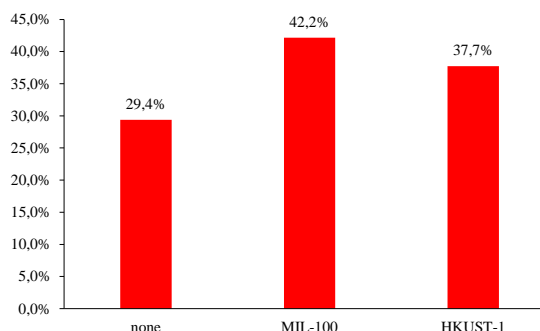


Figure 44: Effect of MOFs on selectivity

3.2.2 MOF type

Based on the comparative analysis of the catalytic performance of MIL-100, HKUST-1, and MOF-808 @His-Cu in the oxidation of hexane to hexanol, several conclusions can be drawn. Nevertheless, it is important to notice that the differences in catalytic performance are rather small and therefore of relative small importance to most other tested parameters. MIL-100 exhibits lower conversion rates compared to HKUST-1, but it achieves higher selectivity towards the desired product, hexanol. This indicates that while MIL-100 may not convert as much hexane overall, it more effectively directs the reaction towards hexanol, minimizing the formation of byproducts.

In contrast, MOF-808 @His-Cu shows both lower conversion and lower selectivity compared to HKUST-1. This suggests that MOF-808 @His-Cu is less efficient in catalysing the oxidation of hexane to hexanol and also less selective, leading to a higher proportion of byproducts. These findings highlight the superior performance of HKUST-1 in terms of conversion efficiency, but also underscore the exceptional selectivity of MIL-100. Understanding these differences is crucial for selecting the appropriate MOF for specific applications where either conversion efficiency or product selectivity is the primary concern.

Table 4: Effect MOF type

Reaction conditions	Catalyst	Conversion	Selectivity
<i>a</i>	MIL-100	0,07%	42,2%
<i>a</i>	HKUST-1	0,11%	37,7%
<i>b</i>	HKUST-1	0,13%	98,4%
<i>b</i>	MOF-808	0,03%	94,3%

Notes: *a*Reaction conditions: Catalyst mass = 100 mg, Temperature = 200 °C, Starting pressure = 1 bar, Reaction time = 2 h, *n*-hexane = 30 mL, *n*-hexane:H₂O₂ (molar) ratio = 4:1. *b*Reaction conditions: Catalyst mass = 100 mg, Temperature = 150 °C, Starting pressure = 1 bar, Reaction time = 2 h, *n*-hexane = 30 mL, *n*-hexane:H₂O₂ (molar) ratio = 4:1.

3.2.3 Relative MOF mass

When varying the mass of the MOF, both conversion and selectivity remain relatively constant, as presented in **Table 5**. This observation can be attributed to the low reaction temperature of 50°C, which is insufficient for the MOF to effectively perform heterogeneous catalysis. At this temperature, the activation energy required for the catalytic activity of the MOF is not met, leading to negligible impact of varying MOF mass on the reaction outcome.

To properly assess the impact of MOF mass on conversion and selectivity, it is recommended to conduct experiments at higher temperatures where the MOF can effectively act as a catalyst. Higher temperatures would provide the necessary activation energy for the MOF to engage in the catalytic process, thereby potentially enhancing both conversion and selectivity. Such conditions would allow for a more accurate

evaluation of the relationship between MOF mass and reaction performance. However, this is beyond the scope of this master thesis and therefore subject to future research.

Table 5: Effect of relative MOF mass

Reaction conditions	Catalyst mass [mg]	Conversion	Selectivity
^a	None	0,03%	91,9%
^a	100	0,03%	93,2%
^a	200	0,03%	94,3%
^a	300	0,03%	94,9%

Notes: ^aReaction conditions: Catalyst = MOF-808 @His-Cu, Temperature = 50 °C, Starting pressure = 1 bar (constant over reaction time), Reaction time = 2 h, *n*-hexane = 3,3 mL, *n*-hexane:H₂O₂ (molar) ratio = 1:1.

3.2.4 Temperature

From the experiments it was noted that as the temperature increases, the conversion of hexane rises, but the selectivity for hexanol decreases, as shown in **Table 6**. This phenomenon can be attributed to several underlying factors that influence the reaction kinetics and pathways at elevated temperatures.

Firstly, higher temperatures generally increase the rate of chemical reactions, leading to a higher conversion of hexane. This is explained by the Arrhenius equation, which states that the reaction rate increases exponentially with temperature due to the greater number of molecules having sufficient energy to overcome the activation energy barrier. Consequently, more hexane molecules are activated and undergo oxidation, resulting in a higher overall conversion rate.

However, while higher temperatures accelerate the oxidation of hexane, they also promote the formation of various byproducts. The oxidation of hexane is a complex process that can lead to multiple reaction pathways. At elevated temperatures, secondary reactions become more prevalent, and these often lead to the formation of undesired byproducts such as carbon dioxide, carbon monoxide, and lower alcohols. This results in a decrease in the selectivity for hexanol, as a larger proportion of the hexane is converted into these byproducts rather than the desired product.

The reduction in selectivity can also be linked to the thermal stability of the reaction intermediates. At higher temperatures, intermediates such as hydroperoxides, which are crucial for the selective formation of hexanol, may decompose more rapidly or follow alternative pathways that lead to other oxidation products. This reduces the efficiency of the desired hexane-to-hexanol conversion pathway, further contributing to the lower selectivity observed.

Additionally, the catalytic activity of the MOFs may change with temperature. MOFs are known to possess specific active sites that facilitate the oxidation process. However, these sites may become less selective at higher temperatures, favouring a broader range of reactions and thereby producing more byproducts. The structural integrity of the MOFs could also be compromised at elevated temperatures, potentially leading to deactivation or the formation of less selective catalytic sites.

In summary, the observed increase in hexane conversion with rising temperature is due to the enhanced reaction rates facilitated by higher thermal energy. However, this comes at the cost of selectivity, as elevated temperatures also favour secondary reactions and byproduct formation. Balancing the temperature to optimize both conversion and selectivity is crucial for achieving efficient and selective oxidation of hexane to hexanol. Further studies focusing on optimizing reaction conditions and catalyst design could help in mitigating these challenges and improving the overall efficiency of the process.

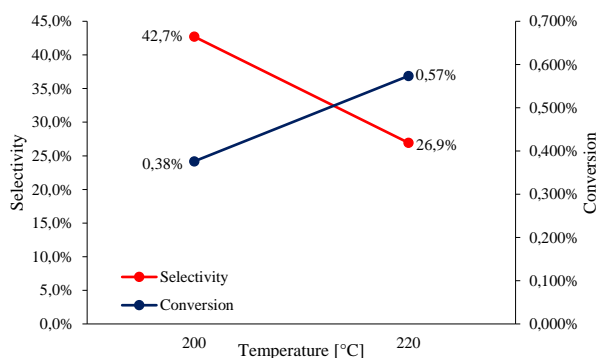
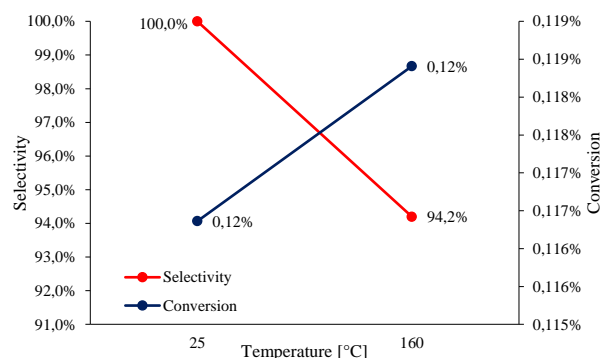
Table 6, shown below, presents two sets of data on the effect of temperature variation. Both sets indicate that increasing the temperature leads to higher conversion but lower selectivity, as previously mentioned in this section.

Table 6: Effect of temperature

Reaction conditions	Temperature [°C]	Conversion	Selectivity
<i>a</i>	200	0,38%	42,7%
<i>a</i>	220	0,57%	26,9%
<i>b</i>	25	0,12%	100,0%
<i>b</i>	160	0,12%	94,2%

Notes: ^aReaction conditions: Catalyst = MIL-100, Catalyst mass = 100 mg, Starting pressure = 1 bar, Reaction time = 2 h, *n*-hexane = 30 mL, *n*-hexane:H₂O₂ (molar) ratio = 0,77:1. ^bReaction conditions: Catalyst = HKUST-1, Catalyst mass = 100 mg, Starting pressure = 30 bar, Reaction time = 4 h, *n*-hexane = 30 mL, *n*-hexane:H₂O₂ (molar) ratio = 0,77:1.

In **Figure 45** and **Figure 46** the effect of temperature is presented graphically for reaction conditions ^a and ^b, as mentioned in the notes of **Table 6**, respectively.

**Figure 45: Effect of temperature for reaction conditions a****Figure 46: Effect of temperature for reaction conditions b**

3.2.5 Pressure

The experimental observations, as shown in **Table 7**, indicate that varying the pressure does not affect selectivity and results in only minor changes in conversion. This can be attributed to the fact that the reaction takes place in the liquid phase. In a liquid-phase reaction, the reactants are already in close contact with the catalyst and each other, meaning that the reaction dynamics are primarily governed by the concentration of reactants, temperature, and the intrinsic properties of the catalyst rather than the pressure.

Since the solubility of gases in liquids is relatively low, changes in pressure have a minimal impact on the concentration of dissolved gases. Therefore, even significant variations in pressure do not substantially alter the availability of reactants in the liquid phase. Consequently, the reaction rate and the efficiency of the catalytic process remain largely unaffected by pressure changes.

In summary, the lack of significant impact of pressure on conversion and selectivity in the liquid-phase oxidation of hexane to hexanol can be explained by the inherent characteristics of liquid-phase reactions. This finding underscores the importance of focusing on other reaction parameters, such as temperature, reactant concentration, and catalyst properties, to optimize the reaction efficiency and selectivity.

Table 7: Effect of pressure

Reaction conditions	Starting pressure [bar]	Conversion	Selectivity
^a	1	0,10%	100,0%
^a	30	0,12%	100,0%

Notes: ^aReaction conditions: Catalyst = HKUST-1, Catalyst mass = 100 mg, Temperature = 25 °C, Reaction time = 4 h, *n*-hexane = 30 mL, *n*-hexane:H₂O₂ (molar) ratio = 0,77:1.

3.2.6 *n*-Hexane:H₂O₂ ratio

The observed phenomenon (**Table 8**) where an increase in the *n*-hexane to H₂O₂ ratio leads to lower conversion but higher selectivity can be explained by considering the role of hydrogen peroxide in the oxidation process and the kinetics of the reaction.

Hydrogen peroxide (H₂O₂) acts as the oxidizing agent in the conversion of *n*-hexane to hexanol. When the ratio of *n*-hexane to H₂O₂ increases, there is relatively less hydrogen peroxide available for the oxidation process. This reduced availability of the oxidizing agent directly impacts the overall conversion rate of *n*-hexane to hexanol. With less H₂O₂, fewer oxidizing equivalents are available to convert *n*-hexane, resulting in a lower overall conversion rate.

However, the higher selectivity observed with an increased *n*-hexane to H₂O₂ ratio can be attributed to the decreased likelihood of over-oxidation and side reactions. In conditions where hydrogen peroxide is abundant, there is a greater chance that intermediate products, such as hexanol, can be further oxidized to unwanted byproducts like hexanoic acid or other higher oxidation state products. This over-oxidation reduces selectivity towards the desired product, hexanol.

By reducing the amount of hydrogen peroxide relative to *n*-hexane, the reaction environment becomes less conducive to over-oxidation. The available H₂O₂ is more likely to selectively oxidize *n*-hexane to hexanol without further reacting with the hexanol product. Thus, the reaction proceeds in a more controlled manner, favouring the formation of hexanol and enhancing selectivity.

Additionally, at higher *n*-hexane to H₂O₂ ratios, the reactant (*n*-hexane) concentration is relatively higher. This higher concentration of *n*-hexane can drive the reaction towards forming hexanol due to the increased likelihood of hexane molecules interacting with the catalyst and the limited amount of H₂O₂ focusing on initial oxidation steps rather than subsequent, less selective reactions.

In summary, increasing the *n*-hexane to H₂O₂ ratio leads to lower conversion because of the limited availability of the oxidizing agent, hydrogen peroxide. However, this condition enhances selectivity by reducing the chances of over-oxidation and side reactions, thereby favouring the formation of the desired product, hexanol. This balance between conversion and selectivity is crucial for optimizing the reaction conditions to achieve high yields of hexanol with minimal byproduct formation.

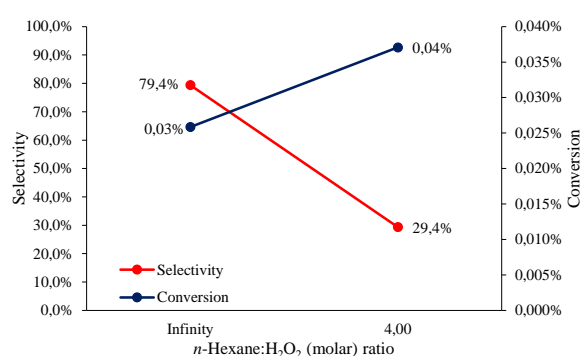
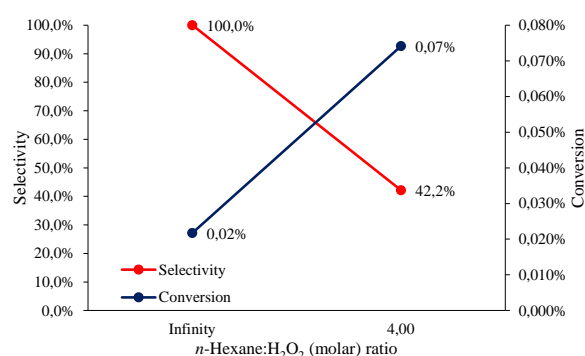
Table 8, shown below, presents two sets of data on the effect of temperature variation. Both sets indicate that increasing the temperature leads to higher conversion but lower selectivity, as previously mentioned in this section.

Table 8: Effect of *n*-hexane:H₂O₂ ratio

Reaction conditions	<i>n</i> -Hexane:H ₂ O ₂ (molar) ratio	Conversion	Selectivity
<i>a</i>	Infinity	0,03%	79,4%
<i>a</i>	4:1	0,04%	29,4%
<i>b</i>	Infinity	0,02%	100,0%
<i>b</i>	4:1	0,07%	42,2%

Notes: ^aReaction conditions: Catalyst = None, Temperature = 200 °C, Starting pressure = 1 bar, Reaction time = 2 h, *n*-hexane = 30 mL. ^bReaction conditions: Catalyst = MIL-100, Catalyst mass = 100 mg, Temperature = 200 °C, Starting pressure = 1 bar, Reaction time = 2 h, *n*-hexane = 30 mL.

In **Figure 47** and **Figure 48** the effect of *n*-hexane:H₂O₂ ratio is presented graphically for reaction conditions ^a and ^b, as mentioned in the notes of **Table 8**, respectively.

**Figure 47: Effect of *n*-hexane:H₂O₂ ratio for reaction conditions a****Figure 48: Effect of *n*-hexane:H₂O₂ ratio for reaction conditions b**

3.2.7 Reaction time

The observed increase in both conversion and selectivity with longer reaction times in the oxidation of *n*-hexane to hexanol, as shown in **Table 9** can be explained by considering the kinetics of the reaction and the nature of the oxidation process.

As the reaction time increases, there is more time for the reactants to interact with the catalyst and oxidizing agent, leading to a higher overall conversion of *n*-hexane to hexanol. The prolonged exposure allows more *n*-hexane molecules to be oxidized, thereby increasing the conversion rate. This is a typical behaviour in many chemical reactions, where extending the reaction time permits more reactants to be transformed into products until equilibrium is reached or the reactants are exhausted.

Regarding selectivity, a possible explanation for the increase in selectivity over time is the gradual deactivation of the active sites of the MOF due to the formation of hexanol. As the reaction proceeds, hexanol, the desired product, may adsorb onto the active sites of the MOF, thereby blocking these sites and reducing their availability for further catalytic activity. This selective deactivation effectively limits the formation of byproducts, as fewer active sites are available for unwanted side reactions. Consequently, the reaction pathway becomes more specific to the desired product, leading to an increase in selectivity over time. This behaviour underscores the dynamic nature of the catalytic process and highlights the role of MOF active site availability in governing the selectivity of the oxidation reaction.

In conclusion, the increase in both conversion and selectivity with longer reaction times can be attributed to the extended opportunity for the primary oxidation reaction to dominate. Additionally, the gradual deactivation of the MOF active sites by the formed hexanol reduces the availability of sites for unwanted side reactions, thereby increasing selectivity. Longer reaction times favour the production of hexanol, resulting in higher conversion rates and improved selectivity.

Table 9, shown below, presents two sets of data on the effect of reaction time. Both sets indicate that increasing the reaction time leads to higher conversion and higher selectivity, as previously mentioned in this section.

Table 9: Effect of reaction time

Reaction conditions	Time [h]	Conversion	Selectivity
<i>a</i>	2	0,03%	29,8%
<i>a</i>	4	0,12%	98,4%
<i>b</i>	0,25	0,02%	87,1%
<i>b</i>	1,5	0,03%	90,0%

Notes: ^aReaction conditions: Catalyst = MIL-100, Catalyst mass = 100 mg, Temperature = 160 °C, Starting pressure = 1 bar, *n*-hexane = 30 mL, *n*-hexane:H₂O₂ (molar) ratio = 0,77:1. ^bReaction conditions: Catalyst = MOF-808 @His-Cu, Catalyst mass = 100 mg, Temperature = 35 °C, Starting pressure = 1 bar (constant over reaction time), *n*-hexane = 3,3 mL, *n*-hexane:H₂O₂ (molar) ratio = 1:1.

In **Figure 49** and **Figure 50** the effect of reaction time is presented graphically for reaction conditions ^a and ^b, as mentioned in the notes of **Table 9**, respectively.

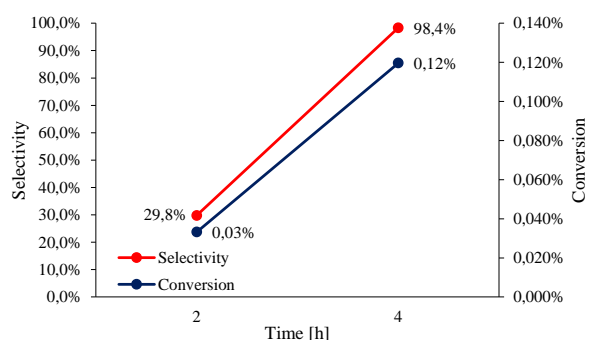


Figure 49: Effect of reaction time for reaction conditions a

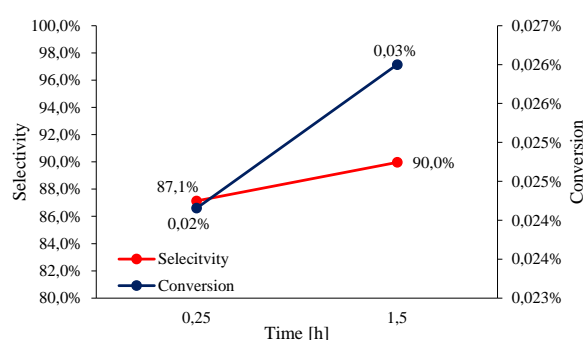


Figure 50: Effect of reaction time for reaction conditions b

4 Conclusion

The comprehensive analysis of the Metal-Organic Frameworks (MOFs) MIL-100, HKUST-1, and MOF-808 @His-Cu reveals significant differences in their pore structures, surface areas, and thermal stability, which directly influence their suitability for different applications. Nitrogen adsorption-desorption isotherms indicate that MIL-100 exhibits both micro- and mesoporous characteristics while HKUST-1 exhibits rather mesoporous characteristics both with distinct hysteresis loops, while MOF-808 @His-Cu shows a more gradual adsorption behaviour with slit-shaped mesopores. MIL-100 has a high total and external surface area due to its contributions from micropores, mesopores, and macropores, making it versatile for various applications. HKUST-1, although having fewer macropores, still offers substantial microporous and mesoporous surface areas. In contrast, MOF-808 @His-Cu's lack of microporosity and limited mesoporosity and macroporosity result in a lower total surface area.

X-ray Diffraction (XRD) analysis confirms the high purity and relatively high crystallinity of MIL-100, though it may have some structural defects or strain. HKUST-1 shows near-purity with minor impurities and good crystallinity, while MOF-808 @His-Cu indicates impurities or incomplete synthesis and moderate structural defects. The reduced intensity of peaks at lower angles in all MOFs suggests a decrease in long-range order or changes in particle size and shape.

The SEM images of MIL-100 display a porous structure with consistent polyhedral grains, indicating high crystallinity and purity. Similarly, HKUST-1 exhibits octahedral crystals with smooth surfaces, reflecting its ordered structure and purity. Contrastingly, MOF-808 @His-Cu shows octahedral crystals with precise surfaces, confirming its crystalline nature. These observations underscore the suitability of each MOF for diverse applications in materials science and catalysis.

Thermogravimetric analysis (TGA) under inert conditions demonstrates that MIL-100 has the highest resistance to decomposition, followed by HKUST-1 and MOF-808 @His-Cu, reflecting their thermal stability hierarchy. The presence of oxygen in oxidative conditions influences the decomposition behaviour, highlighting the importance of understanding the interaction between MOF structures and gaseous environments for optimizing their thermal stability. The isothermal TGA results show that the initial rapid decomposition represents the breakdown of the weakest parts of the MOFs, with subsequent stabilization indicating a more thermally stable remaining structure. Among the MOFs, MIL-100 is the most stable, while MOF-808 @His-Cu is the least stable.

Catalytic experiments for the oxidation of hexane to hexanol show that the presence of MOFs significantly increases both conversion and selectivity, underscoring their role in providing extensive surface areas and efficient catalytic sites. Increasing temperature results in higher conversion but lower selectivity, necessitating a balance to optimize both parameters. The lack of change in selectivity and minimal change in conversion with varying pressure is because the reaction occurs in the liquid phase, where pressure has little impact on the concentration of reactants and the reaction dynamics are primarily governed by temperature and catalyst properties.

Moreover, higher *n*-hexane to H₂O₂ ratios lead to lower conversion but higher selectivity, as limited oxidizing agents reduce over-oxidation and side reactions. When comparing the different MOF types, MIL-100 demonstrates lower conversion but higher selectivity in the oxidation of hexane to hexanol compared to HKUST-1. On the other hand, MOF-808 @His-Cu shows both lower conversion and selectivity than HKUST-1, making it the least efficient of the three MOFs for this reaction. Longer reaction times in the oxidation of *n*-hexane to hexanol increase conversion and selectivity due to extended primary oxidation, stabilized reaction conditions, and the deactivation of MOF active sites by hexanol, which reduces side reactions. Increasing the mass of MOFs results in higher conversion and selectivity, indicating that the catalyst's role is crucial in optimizing the oxidation process and ensuring that more hexane is converted into hexanol with minimal byproduct formation.

Bibliography

- [1] 'BioRender'. Accessed: Feb. 18, 2024. [Online]. Available: <https://app.biorender.com/illustrations/65ce8c1be85a2d63146eb6ac>
- [2] 'BioRender'. Accessed: Feb. 23, 2024. [Online]. Available: <https://app.biorender.com/illustrations/65d8643cc4df37111f646dfa>
- [3] 'Air pollution and associated human mortality: the role of air pollutant emissions, climate change and methane concentration increases from the preindustrial period to present - ProQuest'. Accessed: Feb. 08, 2024. [Online]. Available: <https://www.proquest.com/docview/1306700938?accountid=17248&sourcetype=Scholarly%20Journals>
- [4] S. C. Anenberg *et al.*, 'Global air quality and health co-benefits of mitigating near-term climate change through methane and black carbon emission controls', *Environ Health Perspect*, vol. 120, no. 6, pp. 831–839, Jun. 2012, doi: 10.1289/ehp.1104301.
- [5] S. C. Anenberg, L. W. Horowitz, D. Q. Tong, and J. J. West, 'An estimate of the global burden of anthropogenic ozone and fine particulate matter on premature human mortality using atmospheric modeling', *Environ Health Perspect*, vol. 118, no. 9, pp. 1189–1195, Sep. 2010, doi: 10.1289/ehp.0901220.
- [6] R. J. Cicerone and R. S. Oremland, 'Biogeochemical aspects of atmospheric methane', *Global Biogeochemical Cycles*, vol. 2, no. 4, pp. 299–327, 1988, doi: 10.1029/GB002i004p00299.
- [7] H. Levy, 'Photochemistry of minor constituents in the troposphere', *Planetary and Space Science*, vol. 21, pp. 575–591, Apr. 1973, doi: 10.1016/0032-0633(73)90071-8.
- [8] G. K. Heilig, 'The greenhouse gas methane (CH₄): Sources and sinks, the impact of population growth, possible interventions', *Popul Environ*, vol. 16, no. 2, pp. 109–137, Nov. 1994, doi: 10.1007/BF02208779.
- [9] E. Matthews and I. Fung, 'Methane emission from natural wetlands: Global distribution, area, and environmental characteristics of sources', *Global Biogeochemical Cycles*, vol. 1, no. 1, pp. 61–86, 1987, doi: 10.1029/GB001i001p00061.
- [10] A. Baker-Blocker, T. M. Donahue, K. H. Mancy, A. Baker-Blocker, T. M. Donahue, and K. H. Mancy, 'Methane flux from wetlands areas', *Tellus*, vol. 29, no. 3, Art. no. 3, Jan. 1977, doi: 10.1111/j.2153-3490.1977.tb00731.x.
- [11] J. Lerner, E. Matthews, and I. Fung, 'Methane emission from animals: A Global High-Resolution Data Base', *Global Biogeochemical Cycles*, vol. 2, no. 2, pp. 139–156, Jun. 1988, doi: 10.1029/GB002i002p00139.
- [12] P. J. Crutzen, I. Aselmann, and W. Seiler, 'Methane production by domestic animals, wild ruminants, other herbivorous fauna, and humans', *Tellus B*, vol. 38B, no. 3–4, pp. 271–284, Jul. 1986, doi: 10.1111/j.1600-0889.1986.tb00193.x.
- [13] 'Carbon isotopic composition of atmospheric CH₄: Fossil and biomass burning source strengths - Quay - 1991 - Global Biogeochemical Cycles - Wiley Online Library'. Accessed: Feb. 09, 2024. [Online]. Available: <https://agupubs.onlinelibrary.wiley.com/doi/epdf/10.1029/91GB00003>
- [14] R. Conrad and F. Rothfuss, 'Methane oxidation in the soil surface layer of a flooded rice field and the effect of ammonium', *Biol Fert Soils*, vol. 12, no. 1, pp. 28–32, Sep. 1991, doi: 10.1007/BF00369384.
- [15] M. A. K. Khalil, R. A. Rasmussen, M. X. Wang, and L. Ren, 'Methane emissions from rice fields in China', *Environ. Sci. Technol.*, vol. 25, no. 5, pp. 979–981, May 1991, doi: 10.1021/es00017a023.
- [16] I. Aselmann and P. J. Crutzen, 'Global distribution of natural freshwater wetlands and rice paddies, their net primary productivity, seasonality and possible methane emissions', *J Atmos Chem*, vol. 8, no. 4, pp. 307–358, May 1989, doi: 10.1007/BF00052709.
- [17] R. A. Delmas, A. Marengo, J. P. Tathy, B. Cros, and J. G. R. Baudet, 'Sources and sinks of methane in the African savanna. CH₄ emissions from biomass burning', *Journal of Geophysical Research: Atmospheres*, vol. 96, no. D4, pp. 7287–7299, 1991, doi: 10.1029/90JD02496.
- [18] M. O. Andreae, 'Biomass Burning in the Tropics: Impact on Environmental Quality and Global

- Climate', *Population and Development Review*, vol. 16, pp. 268–291, 1990, doi: 10.2307/2808077.
- [19] H. G. Bingemer and P. J. Crutzen, 'The production of methane from solid wastes', *Journal of Geophysical Research: Atmospheres*, vol. 92, no. D2, pp. 2181–2187, 1987, doi: 10.1029/JD092iD02p02181.
- [20] N. Nakićenović and Intergovernmental Panel on Climate Change, Eds., *Special report on emissions scenarios: a special report of Working Group III of the Intergovernmental Panel on Climate Change*. Cambridge; New York: Cambridge University Press, 2000.
- [21] M. Meinshausen *et al.*, 'The RCP greenhouse gas concentrations and their extensions from 1765 to 2300', *Climatic Change*, vol. 109, no. 1–2, pp. 213–241, Nov. 2011, doi: 10.1007/s10584-011-0156-z.
- [22] O. Boucher, P. Friedlingstein, B. Collins, and K. P. Shine, 'The indirect global warming potential and global temperature change potential due to methane oxidation', *Environ. Res. Lett.*, vol. 4, no. 4, p. 044007, Oct. 2009, doi: 10.1088/1748-9326/4/4/044007.
- [23] 'How satellites, algorithms and AI can help map and trace methane sources', Google. Accessed: Feb. 19, 2024. [Online]. Available: <https://blog.google/outreach-initiatives/sustainability/how-satellites-algorithms-and-ai-can-help-map-and-trace-methane-sources/>
- [24] 'Applications', Methanol Institute. Accessed: Feb. 12, 2024. [Online]. Available: <https://www.methanol.org/applications/>
- [25] T. R. Tephly, 'The toxicity of methanol', *Life Sciences*, vol. 48, no. 11, pp. 1031–1041, Jan. 1991, doi: 10.1016/0024-3205(91)90504-5.
- [26] 'Russia bath lotion kills 49 drinkers in Irkutsk', *BBC News*, Dec. 19, 2016. Accessed: Mar. 27, 2024. [Online]. Available: <https://www.bbc.com/news/world-europe-38363441>
- [27] F. Dalena, A. Senatore, A. Marino, A. Gordano, M. Basile, and A. Basile, 'Chapter 1 - Methanol Production and Applications: An Overview', in *Methanol*, A. Basile and F. Dalena, Eds., Elsevier, 2018, pp. 3–28. doi: 10.1016/B978-0-444-63903-5.00001-7.
- [28] 'Beyond Oil and Gas: The Methanol Economy, 2nd, Updated and Enlarged Edition | Wiley', Wiley.com. Accessed: Mar. 08, 2024. [Online]. Available: <https://www.wiley.com/en-us/Beyond+Oil+and+Gas%3A+The+Methanol+Economy%2C+2nd%2C+Updated+and+Enlarged+Edition-p-9783527644636>
- [29] T. A. Semelsberger, R. L. Borup, and H. L. Greene, 'Dimethyl ether (DME) as an alternative fuel', *Journal of Power Sources*, vol. 156, no. 2, pp. 497–511, Jun. 2006, doi: 10.1016/j.jpowsour.2005.05.082.
- [30] S. Hosseininejad, A. Afacan, and R. E. Hayes, 'Catalytic and kinetic study of methanol dehydration to dimethyl ether', *Chemical Engineering Research and Design*, vol. 90, no. 6, pp. 825–833, Jun. 2012, doi: 10.1016/j.cherd.2011.10.007.
- [31] 'Dimethyl Ether Market Size'. Accessed: Feb. 11, 2024. [Online]. Available: <https://www.mordorintelligence.com/industry-reports/dimethyl-ether-market>
- [32] Y. Lü, W. Yan, S. Hu, and B. Wang, 'Hydrogen production by methanol decomposition using gliding arc gas discharge', *Journal of Fuel Chemistry and Technology*, vol. 40, no. 6, pp. 698–706, Jun. 2012, doi: 10.1016/S1872-5813(12)60025-5.
- [33] H.-J. Choi and M. Kang, 'Hydrogen production from methanol/water decomposition in a liquid photosystem using the anatase structure of Cu loaded TiO₂', *International Journal of Hydrogen Energy*, vol. 32, no. 16, pp. 3841–3848, Nov. 2007, doi: 10.1016/j.ijhydene.2007.05.011.
- [34] Y. Usami, K. Kagawa, M. Kawazoe, Yasuyuki Matsumura, H. Sakurai, and M. Haruta, 'Catalytic methanol decomposition at low temperatures over palladium supported on metal oxides', *Applied Catalysis A: General*, vol. 171, no. 1, pp. 123–130, Jun. 1998, doi: 10.1016/S0926-860X(98)00082-9.
- [35] S. Sá, H. Silva, L. Brandão, J. M. Sousa, and A. Mendes, 'Catalysts for methanol steam reforming—A review', *Applied Catalysis B: Environmental*, vol. 99, no. 1, pp. 43–57, Aug. 2010, doi: 10.1016/j.apcatb.2010.06.015.
- [36] C.-Z. Yao *et al.*, 'Effect of preparation method on the hydrogen production from methanol steam reforming over binary Cu/ZrO₂ catalysts', *Applied Catalysis A: General*, vol. 297, no. 2, pp. 151–


- 158, Jan. 2006, doi: 10.1016/j.apcata.2005.09.002.
- [37] W.-H. Chen and B.-J. Lin, 'Hydrogen production and thermal behavior of methanol autothermal reforming and steam reforming triggered by microwave heating', *International Journal of Hydrogen Energy*, vol. 38, no. 24, pp. 9973–9983, Aug. 2013, doi: 10.1016/j.ijhydene.2013.05.111.
- [38] A. Iulianelli, P. Ribeirinha, A. Mendes, and A. Basile, 'Methanol steam reforming for hydrogen generation via conventional and membrane reactors: A review', *Renewable and Sustainable Energy Reviews*, vol. 29, pp. 355–368, Jan. 2014, doi: 10.1016/j.rser.2013.08.032.
- [39] W.-H. Chen and Y.-J. Syu, 'Thermal behavior and hydrogen production of methanol steam reforming and autothermal reforming with spiral preheating', *International Journal of Hydrogen Energy*, vol. 36, no. 5, pp. 3397–3408, Mar. 2011, doi: 10.1016/j.ijhydene.2010.12.055.
- [40] W.-H. Chen, C.-T. Shen, B.-J. Lin, and S.-C. Liu, 'Hydrogen production from methanol partial oxidation over Pt/Al₂O₃ catalyst with low Pt content', *Energy*, vol. 88, pp. 399–407, Aug. 2015, doi: 10.1016/j.energy.2015.05.055.
- [41] A. S. Damle, 'Hydrogen production by reforming of liquid hydrocarbons in a membrane reactor for portable power generation—Model simulations', *Journal of Power Sources*, vol. 180, no. 1, pp. 516–529, May 2008, doi: 10.1016/j.jpowsour.2008.01.063.
- [42] S. Menia, H. Tebibel, F. Lassouane, A. Khellaf, and I. Nouicer, 'Hydrogen production by methanol aqueous electrolysis using photovoltaic energy: Algerian potential', *International Journal of Hydrogen Energy*, vol. 42, no. 13, pp. 8661–8669, Mar. 2017, doi: 10.1016/j.ijhydene.2016.11.178.
- [43] X. Li and A. Faghri, 'Review and advances of direct methanol fuel cells (DMFCs) part I: Design, fabrication, and testing with high concentration methanol solutions', *Journal of Power Sources*, vol. 226, pp. 223–240, Mar. 2013, doi: 10.1016/j.jpowsour.2012.10.061.
- [44] M. J. Brown and N. D. Parkyns, 'Progress in the partial oxidation of methane to methanol and formaldehyde', *Catalysis Today*, vol. 8, no. 3, pp. 305–335, Jan. 1991, doi: 10.1016/0920-5861(91)80056-F.
- [45] T. Waters, R. A. J. O'Hair, and A. G. Wedd, 'Catalytic Gas Phase Oxidation of Methanol to Formaldehyde', *J. Am. Chem. Soc.*, vol. 125, no. 11, pp. 3384–3396, Mar. 2003, doi: 10.1021/ja028839x.
- [46] F. E. Paulik and J. F. Roth, 'Novel catalysts for the low-pressure carbonylation of methanol to acetic acid', *Chem. Commun. (London)*, no. 24, p. 1578a, 1968, doi: 10.1039/c1968001578a.
- [47] Q. Qian, J. Zhang, M. Cui, and B. Han, 'Synthesis of acetic acid via methanol hydrocarboxylation with CO₂ and H₂', *Nat Commun*, vol. 7, no. 1, p. 11481, May 2016, doi: 10.1038/ncomms11481.
- [48] D. R. Corbin, S. Schwarz, and G. C. Sonnichsen, 'Methylamines synthesis: A review', *Catalysis Today*, vol. 37, no. 2, pp. 71–102, Aug. 1997, doi: 10.1016/S0920-5861(97)00003-5.
- [49] I. Mochida, A. Yasutake, H. Fujitsu, and K. Takeshita, 'Selective synthesis of dimethylamine (DMA) from methanol and ammonia over zeolites', *Journal of Catalysis*, vol. 82, no. 2, pp. 313–321, Aug. 1983, doi: 10.1016/0021-9517(83)90197-5.
- [50] M. R. Gogate, 'Methanol-to-olefins process technology: current status and future prospects', *Petroleum Science and Technology*, vol. 37, no. 5, pp. 559–565, Mar. 2019, doi: 10.1080/10916466.2018.1555589.
- [51] P. Tian, Y. Wei, M. Ye, and Z. Liu, 'Methanol to Olefins (MTO): From Fundamentals to Commercialization', *ACS Catal.*, vol. 5, no. 3, pp. 1922–1938, Mar. 2015, doi: 10.1021/acscatal.5b00007.
- [52] C. D. Chang, J. C. W. Kuo, W. H. Lang, S. M. Jacob, J. J. Wise, and A. J. Silvestri, 'Process Studies on the Conversion of Methanol to Gasoline', ACS Publications. Accessed: Feb. 12, 2024. [Online]. Available: <https://pubs.acs.org/doi/pdf/10.1021/i260067a008>
- [53] E. Kianfar and H. Mazaheri, 'Methanol to gasoline: A Sustainable Transport Fuel', 2020.
- [54] H. A. Zaidi and K. K. Pant, 'Catalytic conversion of methanol to gasoline range hydrocarbons', *Catalysis Today*, vol. 96, no. 3, pp. 155–160, Oct. 2004, doi: 10.1016/j.cattod.2004.06.123.
- [55] M. C. Alvarez-Galvan, N. Mota, M. Ojeda, S. Rojas, R. M. Navarro, and J. L. G. Fierro, 'Direct methane conversion routes to chemicals and fuels', *Catalysis Today*, vol. 171, no. 1, pp. 15–23, Aug. 2011, doi: 10.1016/j.cattod.2011.02.028.
- [56] J. A. Barbero, M. C. Alvarez, M. A. Bañares, M. A. Peña, and J. L. G. Fierro, 'Breakthrough in

- the direct conversion of methane into *c1*-oxygenates', *Chem. Commun.*, no. 11, pp. 1184–1185, May 2002, doi: 10.1039/b202812n.
- [57] K. Tabata *et al.*, 'Activation of methane by oxygen and nitrogen oxides', *Catalysis Reviews*, vol. 44, no. 1, pp. 1–58, Aug. 2002, doi: 10.1081/CR-120001458.
- [58] K. Fujimoto, 'New Uses of Methane', in *Studies in Surface Science and Catalysis*, vol. 81, H. E. Curry-Hyde and R. F. Howe, Eds., in *Natural Gas Conversion II*, vol. 81., Elsevier, 1994, pp. 73–84. doi: 10.1016/S0167-2991(08)63849-5.
- [59] H. D. Gesser and N. R. Hunter, 'A review of C-1 conversion chemistry', *Catalysis Today*, vol. 42, no. 3, pp. 183–189, Jul. 1998, doi: 10.1016/S0920-5861(98)00090-X.
- [60] H. D. Gesser, N. R. Hunter, and C. B. Prakash, 'The direct conversion of methane to methanol by controlled oxidation', *Chem. Rev.*, vol. 85, no. 4, pp. 235–244, Aug. 1985, doi: 10.1021/cr00068a001.
- [61] K. Tabata, Y. Teng, Y. Yamaguchi, H. Sakurai, and E. Suzuki, 'Experimental Verification of Theoretically Calculated Transition Barriers of the Reactions in a Gaseous Selective Oxidation of $\text{CH}_4 - \text{O}_2 - \text{NO}_2$ ', *J. Phys. Chem. A*, vol. 104, no. 12, pp. 2648–2654, Mar. 2000, doi: 10.1021/jp9926239.
- [62] K. Aoki *et al.*, 'Direct conversion of methane into methanol over $\text{MoO}_3/\text{SiO}_2$ catalyst in an excess amount of water vapor', *Catalysis Today*, vol. 45, no. 1, pp. 29–33, Oct. 1998, doi: 10.1016/S0920-5861(98)00236-3.
- [63] M. Sohrabi, L. Vafajoo, S. Morteza, and M. Fattahi, 'Direct Conversion of Methane to Methanol Over $\text{V}_2\text{O}_5/\text{SiO}_2$ Catalyst in a Fixed-Bed Reactor Utilizing a CFD Model', vol. 73, pp. 797–802, Jan. 2011.
- [64] X. Zhang, D. He, Q. Zhang, B. Xu, and Q. Zhu, 'Catalytic conversion of methane to methanol over lanthanum-cobalt-oxide supported molybdenum based catalysts', presented at the ACS Division of Fuel Chemistry, Preprints, 2003, pp. 837–838.
- [65] Q. Zhang, D. He, and Q. Zhu, 'Direct partial oxidation of methane to methanol: Reaction zones and role of catalyst location', *Journal of Natural Gas Chemistry*, vol. 17, no. 1, pp. 24–28, Mar. 2008, doi: 10.1016/S1003-9953(08)60021-3.
- [66] R. Raja and P. Ratnasamy, 'Direct conversion of methane to methanol', *Applied Catalysis A: General*, vol. 158, no. 1, pp. L7–L15, Sep. 1997, doi: 10.1016/S0926-860X(97)00105-1.
- [67] R. Polnišar, M. Štolcová, M. Hronec, and M. Mikula, 'Structure and reactivity of copper iron pyrophosphate catalysts for selective oxidation of methane to formaldehyde and methanol', *Applied Catalysis A: General*, vol. 400, no. 1, pp. 122–130, Jun. 2011, doi: 10.1016/j.apcata.2011.04.022.
- [68] E. V. Starokon, M. V. Parfenov, S. S. Arzumanov, L. V. Pirutko, A. G. Stepanov, and G. I. Panov, 'Oxidation of methane to methanol on the surface of FeZSM-5 zeolite', *Journal of Catalysis*, vol. 300, pp. 47–54, Apr. 2013, doi: 10.1016/j.jcat.2012.12.030.
- [69] Y. K. Krisnandi, B. A. P. Putra, M. Bahtiar, Zahara, I. Abdullah, and R. F. Howe, 'Partial Oxidation of Methane to Methanol over Heterogeneous Catalyst $\text{Co}/\text{ZSM-5}$ ', *Procedia Chemistry*, vol. 14, pp. 508–515, Jan. 2015, doi: 10.1016/j.proche.2015.03.068.
- [70] J. Xu *et al.*, 'Continuous selective oxidation of methane to methanol over Cu- and Fe-modified ZSM-5 catalysts in a flow reactor', *Catalysis Today*, vol. 270, pp. 93–100, Jul. 2016, doi: 10.1016/j.cattod.2015.09.011.
- [71] J. Baek *et al.*, 'Bioinspired Metal–Organic Framework Catalysts for Selective Methane Oxidation to Methanol', *J. Am. Chem. Soc.*, vol. 140, no. 51, pp. 18208–18216, Dec. 2018, doi: 10.1021/jacs.8b11525.
- [72] M. Barona and R. Q. Snurr, 'Exploring the Tunability of Trimetallic MOF Nodes for Partial Oxidation of Methane to Methanol', *ACS Appl. Mater. Interfaces*, vol. 12, no. 25, pp. 28217–28231, Jun. 2020, doi: 10.1021/acsami.0c06241.
- [73] M. C. Simons *et al.*, 'Beyond Radical Rebound: Methane Oxidation to Methanol Catalyzed by Iron Species in Metal–Organic Framework Nodes', *J. Am. Chem. Soc.*, vol. 143, no. 31, pp. 12165–12174, Aug. 2021, doi: 10.1021/jacs.1c04766.
- [74] D. Y. Osadchii *et al.*, 'Isolated Fe Sites in Metal Organic Frameworks Catalyze the Direct Conversion of Methane to Methanol', *ACS Catal.*, vol. 8, no. 6, pp. 5542–5548, Jun. 2018, doi: 10.1021/acscatal.8b00505.

- [75] Z. Zakaria and S. K. Kamarudin, 'Direct conversion technologies of methane to methanol: An overview', *Renewable and Sustainable Energy Reviews*, vol. 65, pp. 250–261, Nov. 2016, doi: 10.1016/j.rser.2016.05.082.
- [76] A. E. Shilov and G. B. Shul'pin, 'Activation of C–H Bonds by Metal Complexes', *Chem. Rev.*, vol. 97, no. 8, pp. 2879–2932, Dec. 1997, doi: 10.1021/cr9411886.
- [77] R. A. Periana, D. J. Taube, S. Gamble, H. Taube, T. Satoh, and H. Fujii, 'Platinum catalysts for the high-yield oxidation of methane to a methanol derivative', *Science*, vol. 280, no. 5363, pp. 560–564, Apr. 1998, doi: 10.1126/science.280.5363.560.
- [78] R. A. Periana *et al.*, 'A mercury-catalyzed, high-yield system for the oxidation of methane to methanol', *Science*, vol. 259, no. 5093, pp. 340–343, Jan. 1993, doi: 10.1126/science.259.5093.340.
- [79] A. K. Md. L. Rahman, M. Kumashiro, and T. Ishihara, 'Direct synthesis of formic acid by partial oxidation of methane on H-ZSM-5 solid acid catalyst', *Catalysis Communications*, vol. 12, no. 13, pp. 1198–1200, Jul. 2011, doi: 10.1016/j.catcom.2011.04.001.
- [80] T. Li, S. J. Wang, C. S. Yu, Y. C. Ma, K. L. Li, and L. W. Lin, 'Direct conversion of methane to methanol over nano-[Au/SiO₂] in [Bmim]Cl ionic liquid', *Applied Catalysis A: General*, vol. 398, no. 1, pp. 150–154, May 2011, doi: 10.1016/j.apcata.2011.03.028.
- [81] R. K. Srivastava, P. K. Sarangi, L. Bhatia, A. K. Singh, and K. P. Shadangi, 'Conversion of methane to methanol: technologies and future challenges', *Biomass Conv. Bioref.*, vol. 12, no. 5, pp. 1851–1875, May 2022, doi: 10.1007/s13399-021-01872-5.
- [82] F. Dalena, A. Senatore, M. Basile, S. Knani, A. Basile, and A. Iulianelli, 'Advances in Methanol Production and Utilization, with Particular Emphasis toward Hydrogen Generation via Membrane Reactor Technology', *Membranes*, vol. 8, no. 4, Art. no. 4, Dec. 2018, doi: 10.3390/membranes8040098.
- [83] A. Yu. Kapran and S. M. Orlyk, 'Hydrogen Production in Methanol Reforming on Modified Copper–Zinc Catalysts: A Review', *Theor Exp Chem*, vol. 53, no. 1, pp. 1–16, Mar. 2017, doi: 10.1007/s11237-017-9495-9.
- [84] M. J. da Silva, 'Synthesis of methanol from methane: Challenges and advances on the multi-step (syngas) and one-step routes (DMTM)', *Fuel Processing Technology*, vol. 145, pp. 42–61, May 2016, doi: 10.1016/j.fuproc.2016.01.023.
- [85] N. J. Brown *et al.*, 'From Organometallic Zinc and Copper Complexes to Highly Active Colloidal Catalysts for the Conversion of CO₂ to Methanol', *ACS Catal.*, vol. 5, no. 5, pp. 2895–2902, May 2015, doi: 10.1021/cs502038y.
- [86] C. Zhang, K.-W. Jun, R. Gao, G. Kwak, and H.-G. Park, 'Carbon dioxide utilization in a gas-to-methanol process combined with CO₂/Steam-mixed reforming: Techno-economic analysis', *Fuel*, vol. 190, pp. 303–311, Feb. 2017, doi: 10.1016/j.fuel.2016.11.008.
- [87] Y. Yang, J. Liu, W. Shen, J. Li, and I.-L. Chien, 'High-efficiency utilization of CO₂ in the methanol production by a novel parallel-series system combining steam and dry methane reforming', *Energy*, vol. 158, pp. 820–829, Sep. 2018, doi: 10.1016/j.energy.2018.06.061.
- [88] L. G. A. van de Water, S. K. Wilkinson, R. A. P. Smith, and M. J. Watson, 'Understanding methanol synthesis from CO/H₂ feeds over Cu/CeO₂ catalysts', *Journal of Catalysis*, vol. 364, pp. 57–68, Aug. 2018, doi: 10.1016/j.jcat.2018.04.026.
- [89] R. Kajaste, M. Hurme, P. Oinas, R. Kajaste, M. Hurme, and P. Oinas, 'Methanol-Managing greenhouse gas emissions in the production chain by optimizing the resource base', *AIMSE*, vol. 6, no. 6, pp. 1074–1102, 2018, doi: 10.3934/energy.2018.6.1074.
- [90] P. V. L. Reddy, K.-H. Kim, and H. Song, 'Emerging green chemical technologies for the conversion of CH₄ to value added products', *Renewable and Sustainable Energy Reviews*, vol. 24, pp. 578–585, Aug. 2013, doi: 10.1016/j.rser.2013.03.035.
- [91] J. R. Roth, *Industrial plasma engineering*. Bristol ; Philadelphia: Institute of Physics Pub, 1995.
- [92] K. Okazaki, T. Kishida, K. Ogawa, and T. Nozaki, 'Direct conversion from methane to methanol for high efficiency energy system with exergy regeneration', *Energy Conversion and Management*, vol. 43, no. 9, pp. 1459–1468, Jun. 2002, doi: 10.1016/S0196-8904(02)00028-6.
- [93] D. W. Larkin, L. L. Lobban, and R. G. Mallinson, 'The direct partial oxidation of methane to organic oxygenates using a dielectric barrier discharge reactor as a catalytic reactor analog', *Catalysis Today*, vol. 71, no. 1, pp. 199–210, Nov. 2001, doi: 10.1016/S0920-5861(01)00430-8.

- [94] T. Nozaki, A. Ağiral, S. Yuzawa, J. G. E. Han Gardeniers, and K. Okazaki, 'A single step methane conversion into synthetic fuels using microplasma reactor', *Chemical Engineering Journal*, vol. 166, no. 1, pp. 288–293, Jan. 2011, doi: 10.1016/j.cej.2010.08.001.
- [95] Y.-F. Wang, C.-H. Tsai, M. Shih, L.-T. Hsieh, and W. Chang, 'Direct Conversion of Methane into Methanol and Formaldehyde in an RF Plasma Environment II: Effects of Experimental Parameters', *Aerosol Air Qual. Res.*, vol. 5, no. 2, pp. 211–224, 205AD, doi: 10.4209/aaqr.2005.12.0007.
- [96] T. Tsuchiya and S. Iizuka, 'Conversion of Methane to Methanol by a Low-Pressure Steam Plasma', 2013. Accessed: Feb. 18, 2024. [Online]. Available: <https://www.semanticscholar.org/paper/Conversion-of-Methane-to-Methanol-by-a-Low-Pressure-Tsuchiya-Iizuka/4ee805beed563ff3f719e955d5fc13f6ced3a940>
- [97] Sk. Mahammadunnisa, K. Krushnamurthy, and Ch. Subrahmanyam, 'Catalytic nonthermal plasma assisted co-processing of methane and nitrous oxide for methanol production', *Catalysis Today*, vol. 256, pp. 102–107, Nov. 2015, doi: 10.1016/j.cattod.2015.03.011.
- [98] L. Chen, X. Zhang, L. Huang, and L. Lei, 'Application of in-plasma catalysis and post-plasma catalysis for methane partial oxidation to methanol over a Fe₂O₃-CuO/ γ -Al₂O₃ catalyst', *Journal of Natural Gas Chemistry*, vol. 19, no. 6, pp. 628–637, Nov. 2010, doi: 10.1016/S1003-9953(09)60129-8.
- [99] J. H. Lunsford, 'Catalytic conversion of methane to more useful chemicals and fuels: a challenge for the 21st century', *Catalysis Today*, vol. 63, no. 2, pp. 165–174, Dec. 2000, doi: 10.1016/S0920-5861(00)00456-9.
- [100] B. Michalkiewicz, 'Partial oxidation of methane to formaldehyde and methanol using molecular oxygen over Fe-ZSM-5', *Applied Catalysis A: General*, vol. 277, no. 1, pp. 147–153, Dec. 2004, doi: 10.1016/j.apcata.2004.09.005.
- [101] S. D. Razumovsky *et al.*, 'Effect of immobilization on the main dynamic characteristics of the enzymatic oxidation of methane to methanol by bacteria *Methylosinus sporium* B-2121', *Russ Chem Bull*, vol. 57, no. 8, pp. 1633–1636, Aug. 2008, doi: 10.1007/s11172-008-0211-8.
- [102] 'MIL-100(Fe) as a new catalyst for selective catalysis reduction of NO_x with ammonia'. Accessed: Mar. 19, 2024. [Online]. Available: <https://www.tandfonline.com/doi/epdf/10.1080/10584587.2017.1352302?needAccess=true>
- [103] D. J. Xiao *et al.*, 'Oxidation of ethane to ethanol by N₂O in a metal–organic framework with coordinatively unsaturated iron(II) sites', *Nature Chem*, vol. 6, no. 7, Art. no. 7, Jul. 2014, doi: 10.1038/nchem.1956.
- [104] M. C. Simons *et al.*, 'Structure, Dynamics, and Reactivity for Light Alkane Oxidation of Fe(II) Sites Situated in the Nodes of a Metal–Organic Framework', *J. Am. Chem. Soc.*, vol. 141, no. 45, pp. 18142–18151, Nov. 2019, doi: 10.1021/jacs.9b08686.
- [105] V. N. Parmon, G. I. Panov, A. Uriarte, and A. S. Noskov, 'Nitrous oxide in oxidation chemistry and catalysis: application and production', *Catalysis Today*, vol. 100, no. 1, pp. 115–131, Feb. 2005, doi: 10.1016/j.cattod.2004.12.012.
- [106] G. B. Skinner, A. Lifshitz, K. Scheller, and A. Burcat, 'Kinetics of Methane Oxidation', *The Journal of Chemical Physics*, vol. 56, no. 8, pp. 3853–3861, Apr. 1972, doi: 10.1063/1.1677790.
- [107] 'MIL-100 (Fe) - CD Bioparticles'. Accessed: Mar. 01, 2024. [Online]. Available: <https://www.cd-bioparticles.net/p/9624/mil-100-fe>
- [108] 'HKUST-1 Metal Organic Framework', ChemTube3D. Accessed: Feb. 27, 2024. [Online]. Available: <https://www.chemtube3d.com/mof-hkust-1-2/>
- [109] crystallography365, 'The structure of empty space – HKUST 1', Crystallography365. Accessed: Mar. 22, 2024. [Online]. Available: <https://crystallography365.wordpress.com/2014/01/03/the-structure-of-empty-space-hkust-1/>
- [110] C. H. Hendon and A. Walsh, 'Chemical principles underpinning the performance of the metal–organic framework HKUST-1', *Chem. Sci.*, vol. 6, no. 7, pp. 3674–3683, 2015, doi: 10.1039/C5SC01489A.
- [111] 'MOF-808 (Zr) - CD Bioparticles'. Accessed: Feb. 27, 2024. [Online]. Available: <https://www.cd-bioparticles.net/p/9211/mof-808-zr>
- [112] H. G. T. Ly, G. Fu, A. Kondinski, B. Bueken, D. De Vos, and T. N. Parac-Vogt, 'Superactivity of MOF-808 toward Peptide Bond Hydrolysis', *J. Am. Chem. Soc.*, vol. 140, no. 20, pp. 6325–6335,

- May 2018, doi: 10.1021/jacs.8b01902.
- [113] A. Valverde *et al.*, ‘Enzyme-mimicking of copper-sites in metal–organic frameworks for oxidative degradation of phenolic compounds’, *J. Mater. Chem. A*, vol. 12, no. 8, pp. 4555–4571, 2024, doi: 10.1039/D3TA06198A.
- [114] ‘Cu-MOF-808 as a Sensing Material for Gaseous Hydrogen Sulfide - Marquardt - 2023 - ChemPlusChem - Wiley Online Library’. Accessed: Mar. 22, 2024. [Online]. Available: <https://chemistry-europe-onlinelibrary-wiley-com.kuleuven.e-bronnen.be/doi/full/10.1002/cplu.202300109>
- [115] A. S. Hakemian and A. C. Rosenzweig, ‘The Biochemistry of Methane Oxidation’, *Annu. Rev. Biochem.*, vol. 76, no. 1, pp. 223–241, Jun. 2007, doi: 10.1146/annurev.biochem.76.061505.175355.
- [116] J. C. Murrell, B. Gilbert, and I. R. McDonald, ‘Molecular biology and regulation of methane monooxygenase’, *Arch. Microbiol.*, vol. 173, no. 5, pp. 325–332, Jun. 2000, doi: 10.1007/s002030000158.
- [117] S. Sirajuddin and A. C. Rosenzweig, ‘Enzymatic Oxidation of Methane’, *Biochemistry*, vol. 54, no. 14, pp. 2283–2294, Apr. 2015, doi: 10.1021/acs.biochem.5b00198.
- [118] ‘Hexane - Definition, Properties, Structure, and Uses’, VEDANTU. Accessed: Mar. 30, 2024. [Online]. Available: <https://www.vedantu.com/chemistry/hexane>
- [119] PubChem, ‘n-HEXANE’. Accessed: Mar. 30, 2024. [Online]. Available: <https://pubchem.ncbi.nlm.nih.gov/compound/8058>
- [120] PubChem, ‘Hydrogen Peroxide’. Accessed: Mar. 30, 2024. [Online]. Available: <https://pubchem.ncbi.nlm.nih.gov/compound/784>
- [121] ‘Hydrogen Peroxide | Physico-Chemical Properties’. Accessed: Mar. 30, 2024. [Online]. Available: <https://active-oxygens.evonik.com/en/products-and-services/hydrogen-peroxide/general-information/physico-chemical-properties>
- [122] PubChem, ‘1-Hexanol’. Accessed: Mar. 30, 2024. [Online]. Available: <https://pubchem.ncbi.nlm.nih.gov/compound/8103>
- [123] ‘1-Hexanol | 111-27-3’, ChemicalBook. Accessed: Mar. 30, 2024. [Online]. Available: https://www.chemicalbook.com/ChemicalProductProperty_EN_CB8461421.htm
- [124] N. Belhadj, M. Lailliau, R. Benoit, and P. Dagaut, ‘Experimental and kinetic modeling study of *n*-hexane oxidation. Detection of complex low-temperature products using high-resolution mass spectrometry’, *Combustion and Flame*, vol. 233, p. 111581, Nov. 2021, doi: 10.1016/j.combustflame.2021.111581.
- [125] L. S. Shul’pina, M. V. Kirillova, A. J. L. Pombeiro, and G. B. Shul’pin, ‘Alkane oxidation by the H₂O₂–NaVO₃–H₂SO₄ system in acetonitrile and water’, *Tetrahedron*, vol. 65, no. 12, pp. 2424–2429, Mar. 2009, doi: 10.1016/j.tet.2009.01.088.
- [126] ‘n-Hexane 95% for analysis, ACS’. Accessed: Apr. 17, 2024. [Online]. Available: <https://www.itwreagents.com/united-states/en/product/n-hexane-95-for-analysis-acs/133242>
- [127] ‘Hydrogen peroxide, 35%, reagent grade EUD Required, Non-Account Cust’. Accessed: May 14, 2024. [Online]. Available: <https://shop.chemsupply.com.au/hydrogen-peroxide-35-reagent-grade-eud-required-non-account-cust>
- [128] ‘Trimesic acid 95 554-95-0’. Accessed: Apr. 17, 2024. [Online]. Available: <http://www.sigmaaldrich.com/>
- [129] ‘Sodium hydroxide’. Accessed: Apr. 17, 2024. [Online]. Available: <https://lab.honeywell.com/shop/sodium-hydroxide-71690>
- [130] ‘Iron(II) chloride ReagentPlus , 98 13478-10-9’. Accessed: Apr. 17, 2024. [Online]. Available: <http://www.sigmaaldrich.com/>
- [131] ‘Ethanol 96 EMSURE Reag. Ph Eur 64-17-5’. Accessed: Apr. 17, 2024. [Online]. Available: <http://www.sigmaaldrich.com/>
- [132] ‘Sodium bicarbonate puriss., meets analytical specification of Ph. Eur., BP, USP, FCC, E500, 99.0-100.5 , powder 144-55-8’. Accessed: May 02, 2024. [Online]. Available: <http://www.sigmaaldrich.com/>
- [133] ‘Nitrato de cobre(II) hemi(pentahidrato), 98 %, Thermo Scientific Chemicals’. Accessed: May 02, 2024. [Online]. Available: <https://www.thermofisher.com/order/catalog/product/es/es/A14004.30>
- [134] ‘Ácido acético glacial 99,8% AGR ACS, ISO, Ph. Eur.’, Labbox España. Accessed: Apr. 17, 2024.

- [Online]. Available: <https://esp.labbox.com/producto/acido-acetico-glacial-99-8-agr-acs-iso-ph-eur/>
- [135] ‘Zirconium(IV) chloride = 99.5 trace metals 10026-11-6’. Accessed: Apr. 17, 2024. [Online]. Available: <http://www.sigmaaldrich.com/>
- [136] ‘L-Histidine ReagentPlus , =99 TLC 71-00-1’. Accessed: Apr. 17, 2024. [Online]. Available: <http://www.sigmaaldrich.com/>
- [137] ‘Metanol AGR ACS,ISO,Ph.Eur.’, Labbox España. Accessed: Apr. 17, 2024. [Online]. Available: <https://esp.labbox.com/producto/metanol-agr-acsisoph-eur/>
- [138] ‘Copper(II) acetate ACS reagent, = 98 6046-93-1’. Accessed: Apr. 17, 2024. [Online]. Available: <http://www.sigmaaldrich.com/>
- [139] ‘Acetonitrilo GC/HPLC GGR’, Labbox España. Accessed: Apr. 17, 2024. [Online]. Available: <https://esp.labbox.com/producto/acetonitrilo-gc-hplc-ggr/>
- [140] ‘BioRender’. Accessed: Apr. 29, 2024. [Online]. Available: <https://app.biorender.com/illustrations/662e1551c5f49812e09b992d>
- [141] G. Chen *et al.*, ‘In Vitro Toxicity Study of a Porous Iron(III) Metal–Organic Framework’, *Molecules*, vol. 24, no. 7, Art. no. 7, Jan. 2019, doi: 10.3390/molecules24071211.
- [142] S. Loera-Serna, L. L. Núñez, J. Flores, R. López-Simeon, and H. I. Beltrán, ‘An alkaline one-pot metathesis reaction to give a [Cu₃(BTC)₂] MOF at r.t., with free Cu coordination sites and enhanced hydrogen uptake properties’, *RSC Adv.*, vol. 3, no. 27, p. 10962, 2013, doi: 10.1039/c3ra40726h.
- [143] ‘HKUST-1’, *Wikipedia*. Feb. 16, 2024. Accessed: Apr. 10, 2024. [Online]. Available: <https://en.wikipedia.org/w/index.php?title=HKUST-1&oldid=1208284391>
- [144] ‘Figure 3. The IUPAC classification of adsorption isotherms showing both...’, ResearchGate. Accessed: May 26, 2024. [Online]. Available: https://www.researchgate.net/figure/The-IUPAC-classification-of-adsorption-isotherms-showing-both-the-adsorption-and_fig2_258684354
- [145] M. D. Donohue and G. L. Aranovich, ‘Adsorption Hysteresis in Porous Solids’, *Journal of Colloid and Interface Science*, vol. 205, no. 1, pp. 121–130, Sep. 1998, doi: 10.1006/jcis.1998.5639.
- [146] ‘Figure 4. The relationship between the pore shape and the...’, ResearchGate. Accessed: May 26, 2024. [Online]. Available: https://www.researchgate.net/figure/The-relationship-between-the-pore-shape-and-the-adsorption-desorption-isotherm_fig3_258684354
- [147] M. A. Al-Ghouti and D. A. Da’ana, ‘Guidelines for the use and interpretation of adsorption isotherm models: A review’, *Journal of Hazardous Materials*, vol. 393, p. 122383, Jul. 2020, doi: 10.1016/j.jhazmat.2020.122383.
- [148] S. Brunauer, P. H. Emmett, and E. Teller, ‘Adsorption of Gases in Multimolecular Layers’, *J. Am. Chem. Soc.*, vol. 60, no. 2, pp. 309–319, Feb. 1938, doi: 10.1021/ja01269a023.
- [149] K. Sing, ‘The use of nitrogen adsorption for the characterisation of porous materials’, *Colloids and Surfaces A: Physicochemical and Engineering Aspects*, vol. 187–188, pp. 3–9, Aug. 2001, doi: 10.1016/S0927-7757(01)00612-4.
- [150] D. Dollimore, P. Spooner, and A. Turner, ‘The bet method of analysis of gas adsorption data and its relevance to the calculation of surface areas’, *Surface Technology*, vol. 4, no. 2, pp. 121–160, Mar. 1976, doi: 10.1016/0376-4583(76)90024-8.
- [151] E. P. Barrett, L. G. Joyner, and P. P. Halenda, ‘The Determination of Pore Volume and Area Distributions in Porous Substances. I. Computations from Nitrogen Isotherms’, *J. Am. Chem. Soc.*, vol. 73, no. 1, pp. 373–380, Jan. 1951, doi: 10.1021/ja01145a126.
- [152] R. Bardestani, G. S. Patience, and S. Kaliaguine, ‘Experimental methods in chemical engineering: specific surface area and pore size distribution measurements—BET, BJH, and DFT’, *The Canadian Journal of Chemical Engineering*, vol. 97, no. 11, pp. 2781–2791, 2019, doi: 10.1002/cjce.23632.
- [153] G. Jura and W. D. Harkins, ‘Surfaces of Solids. XI. Determination of the Decrease (π) of Free Surface Energy of a Solid by an Adsorbed Film’, *J. Am. Chem. Soc.*, vol. 66, no. 8, pp. 1356–1362, Aug. 1944, doi: 10.1021/ja01236a046.
- [154] A. Galarneau, F. Villemot, J. Rodriguez, F. Fajula, and B. Coasne, ‘Validity of the *t*-plot Method to Assess Microporosity in Hierarchical Micro/Mesoporous Materials’, *Langmuir*, vol. 30, no. 44, pp. 13266–13274, Nov. 2014, doi: 10.1021/la5026679.
- [155] M. Lee, *X-Ray Diffraction for Materials Research: From Fundamentals to Applications*. New

- York: Apple Academic Press, 2017. doi: 10.1201/b19936.
- [156] R. James, 'X-Ray Diffraction'.
- [157] 'Bragg law | Definition, Equation, Diagram, & Facts | Britannica'. Accessed: Apr. 09, 2024. [Online]. Available: <https://www.britannica.com/science/Bragg-law>
- [158] 'Field Emission Scanning Electron Microscopy (FE-SEM)'. Accessed: Apr. 19, 2024. [Online]. Available: <https://vaccoat.com/blog/field-emission-scanning-electron-microscopy-fesem/>
- [159] 'BioRender'. Accessed: Apr. 24, 2024. [Online]. Available: <https://app.biorender.com/illustrations/6628c4c76787aac6b126f1d4>
- [160] K. Akhtar, S. A. Khan, S. B. Khan, and A. M. Asiri, 'Scanning Electron Microscopy: Principle and Applications in Nanomaterials Characterization', in *Handbook of Materials Characterization*, S. K. Sharma, Ed., Cham: Springer International Publishing, 2018, pp. 113–145. doi: 10.1007/978-3-319-92955-2_4.
- [161] S. Vyazovkin, A. Burnham, J. Criado, L. Pérez-Maqueda, C. Popescu, and N. Sbirrazzuoli, 'ICTAC Kinetics Committee Recommendations for Performing Kinetic Computations on Thermal Analysis Data', *Thermochimica Acta*, vol. 520, pp. 1–19, Jun. 2011, doi: 10.1016/j.tca.2011.03.034.
- [162] 'Thermal Analysis of Polymers: Fundamentals and Applications | Wiley', Wiley.com. Accessed: Apr. 16, 2024. [Online]. Available: <https://www.wiley.com/en-us/Thermal+Analysis+of+Polymers%3A+Fundamentals+and+Applications-p-9780471769170>
- [163] N. Saadatkhan *et al.*, 'Experimental methods in chemical engineering: Thermogravimetric analysis—TGA', *The Canadian Journal of Chemical Engineering*, vol. 98, no. 1, pp. 34–43, 2020, doi: 10.1002/cjce.23673.
- [164] P. Tiwari and M. Deo, 'Detailed kinetic analysis of oil shale pyrolysis TGA data', *AIChE Journal*, vol. 58, no. 2, pp. 505–515, 2012, doi: 10.1002/aic.12589.
- [165] M. Edake, M. Dalil, M. J. Darabi Mahboub, J.-L. Dubois, and G. S. Patience, 'Catalytic glycerol hydrogenolysis to 1,3-propanediol in a gas–solid fluidized bed', *RSC Adv.*, vol. 7, no. 7, pp. 3853–3860, 2017, doi: 10.1039/C6RA27248G.
- [166] 'Gas Chromatography – How a Gas Chromatography Machine Works, How To Read a Chromatograph and GCxGC', Analysis & Separations from Technology Networks. Accessed: Mar. 25, 2024. [Online]. Available: <http://www.technologynetworks.com/analysis/articles/gas-chromatography-how-a-gas-chromatography-machine-works-how-to-read-a-chromatograph-and-gcxc-335168>
- [167] 'BioRender'. Accessed: Mar. 25, 2024. [Online]. Available: <https://app.biorender.com/illustrations/660146f76570ab4280a7cdcd>
- [168] 'Fig. 1 Schematic plot of the main components of GC–MS instruments', ResearchGate. Accessed: Mar. 25, 2024. [Online]. Available: https://www.researchgate.net/figure/Schematic-plot-of-the-main-components-of-GC-MS-instruments_fig1_273955959
- [169] N. Frank, '6890 Site Prep and Installation'.
- [170] 'Agilent 7683B Automatic Liquid Sampler Installation, Operation and Maintenance'.
- [171] '125-7032UI | Agilent'. Accessed: Apr. 11, 2024. [Online]. Available: https://www.agilent.com/store/en_US/Prod-125-7032UI/125-7032UI
- [172] 'GCMS-QP2010Ultra_SE-UsersGuideVer2.6-29919qx.pdf'. Accessed: Mar. 26, 2024. [Online]. Available: https://cpb-us-w2.wpmucdn.com/wordpress.lehigh.edu/dist/1/313/files/2017/05/GCMS-QP2010Ultra_SE-UsersGuideVer2.6-29919qx.pdf
- [173] '5989-3290EN.pdf'. Accessed: Mar. 25, 2024. [Online]. Available: <https://www.agilent.com/cs/library/specifications/Public/5989-3290EN.pdf>
- [174] 'Shimadzu AOC-20i_20s Autosampler Instruction Manual.pdf'. Accessed: Mar. 26, 2024. [Online]. Available: https://chemistry.unt.edu/system/files/Shimadzu%20AOC-20i_20s%20Autosampler%20Instruction%20Manual.pdf
- [175] 'TRB-WAX'. Accessed: Apr. 16, 2024. [Online]. Available: <https://www.teknokroma.es/en/products/gc-chromatography/gc-capillary-columns/fused-silica-capillary-column/trb-wax/TR-140233>
- [176] 'Crystallography Open Database: Search results'. Accessed: May 22, 2024. [Online]. Available: <https://www.crystallography.net/cod/result.php>

- [177] N. Bhuvanesh, J. H. Reibenspies, A. A. Yakovenko, and H.-C. Zhou, 'Generation and applications of structure envelopes for porous metal–organic frameworks', *J Appl Cryst*, vol. 46, no. 2, pp. 346–353, Apr. 2013, doi: 10.1107/S0021889812050935.
- [178] J. Jiang, F. Gándara, Y.-B. Zhang, K. Na, O. M. Yaghi, and W. G. Klemperer, 'Superacidity in Sulfated Metal–Organic Framework-808', *J. Am. Chem. Soc.*, vol. 136, no. 37, pp. 12844–12847, Sep. 2014, doi: 10.1021/ja507119n.



Universidad del País Vasco Euskal Herriko Unibertsitatea

FACULTY
OF ENGINEERING
BILBAO
UNIVERSITY
OF THE BASQUE
COUNTRY

FACULTY OF ENGINEERING BIBAO
CAMPUS OF BILBAO
Ingeniero Torres Quevedo Plaza, 1
48013 BILBAO, Biscay, Spain
tel. + 34 946 01 40 24
secretaria.eib@ehu.eus

<http://www.ehu.eus/ingeniaritza-bilbo>